

Kinetic treatment of magnetized and collisionless plasma near a wall



Alessandro Geraldini

Merton College

University of Oxford

A thesis submitted for the degree of

Doctor of Philosophy

Jul 2018

Abstract

Charged particles gyrate around magnetic field lines, a property that is exploited to confine plasma in magnetic confinement fusion devices. Typically, the gyroradius is small compared to the system size and thus the gyromotion can be averaged out. The resulting charged particle motion closely follows a magnetic field line. At the edge of fusion devices, the magnetic field usually impinges on a wall at a shallow angle. A boundary layer forms in which the plasma density changes over a characteristic distance from the wall of the order of the ion gyroradius, as ions are absorbed during their gyromotion. This boundary layer is called magnetic presheath, and is typically collisionless and quasineutral. Importantly, the electric field in this region distorts the ion gyro-orbits, making them non-circular and thus affecting the ion density profile. Solving the magnetic presheath amounts to obtaining the self-consistent electric field for which the net charge density is zero.

In this thesis, I assume a small magnetic field angle and small gradients parallel to the wall to develop an asymptotic theory for the magnetic presheath, which is used to obtain the ion density. The small, yet crucial, contribution of the part of the orbit near the wall is included. To demonstrate the theory for a case without any gradients parallel to the wall, I calculate numerically the self-consistent electrostatic potential by assuming the electron density to be a Boltzmann distribution. The model is used to study the dependence of magnetic presheath characteristics on magnetic field angle and ion temperature. The distribution function of ions that have traversed the magnetic presheath is obtained, which is important to predict the amount of sputtering and erosion at the wall of a fusion device.

Acknowledgements

I cannot thank enough my PhD supervisor, Felix Parra: in these four years, he has been able to simultaneously motivate, encourage and teach me in the best possible way. I also thank my co-supervisor at Culham Centre for Fusion Energy (CCFE), Fulvio Militello, for his contribution and support.

Several people have given me feedback about my work. I thank Greg Hammett, Paolo Ricci, Dmitri Ryutov, Paul Dellar, Chris Ham, John Omotani and Ian Abel for discussions and comments. I am especially grateful to Paolo for reading this thesis with genuine curiosity and for giving me valuable advice.

Together with Felix, Alex Schekochihin, Michael Barnes and Steve Cowley have created the perfect research environment in the Oxford Plasma Theory group; I thank them for this and for their continuous feedback. Especially Alex, who not only read this thesis but has also been like a mentor.

During my time in the group, I am lucky to have bridged two “generations” of students and postdocs: the “Lads on Tour” Justin, Michael F, Ferdinand and Marek; the “Plasmaniacs” Nick, Michael H, Adwiteey, Valerian, Plamen, Jason, Ollie, Mantas, Yohei and Adnane. I have enjoyed spending my days with them, as well as conferences (tours) and ping-pong games.

A number of people have made my time at Oxford special. I thank all of those who kept me company in these years, be it with dinner nights, pints, coffees, house-sharing, tennis or simply an occasional life talk. I especially thank Luca, Francesco, Jutta, Karl and Richard, who were always there when I needed them. And Andriana, who taught me the meaning of $\epsilon\rho\omega\tau\epsilon\upsilon\mu\acute{\epsilon}\nu\omicron\varsigma$.

I am grateful to my family for their wholehearted love and support throughout my life, and for encouraging me to do what I wanted.

This work has received funding from the RCUK Energy Programme [grant number EP/P012450/1]. I am grateful to CCFE for supporting me financially. I have also received financial support for conferences from Merton College and the Wolfgang Pauli Institute.

Contents

1	Introduction	1
1.1	Plasma-wall interaction	2
1.2	The magnetic presheath	6
2	Ion trajectories	11
2.1	Orderings	12
2.2	Periodic orbits	19
2.2.1	Orbit parameters	20
2.2.2	Types of effective potential curves	22
2.2.3	Periodicity	27
2.3	Magnetic presheath trajectories	28
2.3.1	Approximately closed orbits	29
2.3.2	Open orbits	34
3	Ion distribution function and density	43
3.1	Ion distribution function	44
3.2	Ion density	46
3.2.1	Closed orbit density	46
3.2.2	Open orbit density	50
4	Electron-repelling magnetic presheath	59
4.1	Boltzmann electrons	60
4.2	Quasineutrality equation	62
4.3	Magnetic presheath entrance	64
4.4	Debye sheath entrance	70
4.5	Numerical method	77
4.6	Numerical results	83
5	Ion temperature dependence	95
5.1	Boundary conditions	97

5.2	Finite ion temperature	99
5.3	Zero ion temperature limit	102
5.3.1	Closed orbit region ($x \gg x_c$)	109
5.3.2	Open orbit region ($x \ll x_c$)	113
5.3.3	Intermediate region ($x \sim x_c$)	115
5.4	Infinite ion temperature limit	117
5.5	Discussion	121
6	Conclusions	123
A	Typical widths of the plasma-wall boundary layers in a tokamak	129
B	Orderings in the context of a tokamak	133
B.1	Turbulence	133
B.2	Steady-state scrape-off layer width	136
C	How large can the parallel current be?	139
D	Adiabatic invariant	143
E	Ion density at the magnetic presheath entrance	145
E.1	Adiabatic invariant expansion	145
E.2	Gyrophase expansion	147
E.3	Change of variables in the ion density integral	148
E.4	Expansion of the integral over U in equation (E.23)	150
F	Proof that $k_2 > 0$ and $q_2 > 0$	153
G	Neglecting the contribution of type II closed orbits near $x = 0$	157
H	Integrals of temperature-dependent distribution functions	159
	Bibliography	165

List of Figures

11	Boundary layers of magnetized plasma	5
21	Effective potential types	22
22	Electrostatic potential example and its derivatives	24
23	Values of orbit position for which the effective potential is type I or type II .	25
24	Ion trajectories in the magnetic presheath	31
25	Phase space ion trajectories in the transition from a closed to an open orbit .	36
31	Minimum orbit position for a closed orbit	49
32	Minimum orbit position for an open orbit	52
33	Phase space ion trajectories and accuracy of the range of velocities of an open orbit	54
41	Condition for adiabatic electrons (general ion temperature)	61
42	Numerical grid of distance from the wall	78
43	Numerical grid of energy	80
44	Example of failure of the numerical method	82
45	Distribution function at magnetic presheath entrance	83
46	Distribution function at magnetic presheath entrance (in 3 dimensions) . . .	84
47	Electrostatic potential profiles	86
48	Ion density profiles	86
49	Ion fluid velocity profiles	87
410	Ion distribution function at the Debye sheath entrance (velocity component normal to wall)	89

LIST OF FIGURES

411	Ion distribution function at the Debye sheath entrance (velocity components parallel to wall)	90
412	Ion distribution function at the Debye sheath entrance (velocity components parallel to the magnetic field and perpendicular to wall)	91
413	Electrostatic potential drop	92
51	Electrostatic potential drop as a function of α and τ	100
52	Electrostatic potential profiles for $\alpha = 0.05$ at several values of τ	100
53	Flow profiles for $\alpha = 0.05$ at different values of τ	101
54	1D distribution function at the wall and at the magnetic presheath entrance .	103
55	2D distribution function at the Debye and magnetic presheath entrance . . .	104
56	Effective potential curves of small-temperature ions	109
B1	Plasma-wall boundary geometry in the context of a tokamak	134
B2	Turbulence orderings	135
B3	Length scales in magnetic presheath	137
E1	Inverting the order of integration in the ion density integral at $x \rightarrow \infty$. . .	149

CHAPTER 1

Introduction

Harnessing the energy released during nuclear fusion reactions is the objective of nuclear fusion research, with a collective effort from physicists, engineers and materials scientists. Confinement of the hot plasma required for fusion reactions can be achieved by using magnetic fields. Magnetic forces cause the charged particles in a plasma to gyrate, thus confining them within a gyroradius in the two dimensions perpendicular to the magnetic field. Existing concepts for magnetic confinement fusion include tokamaks [1], stellarators [2], magnetic mirrors [3] and reversed-field pinches [4]. Most of these concepts [1, 2, 4] rely on a magnetic field with magnetic field lines that do not reach the wall in order to achieve confinement parallel to the magnetic field. Even in such devices, particle and energy confinement is far from perfect for several reasons, including collisions, orbit drifts, plasma instabilities and turbulence. Thus, particles and energy slowly travel perpendicular to the magnetic field and eventually leave the confinement region.

The plasma and the closed field lines must be contained in a finite volume with boundaries, because the magnets generating most of the confining field must be protected from the plasma and from the neutrons generated by the fusion reactions. Hence,

at the boundary of a fusion device there are regions in which the magnetic field lines are open and terminate at a wall. These walls are subject to a constant particle and energy flux from the plasma leaving the confinement region. Therefore, it is crucial to understand and predict how the particles and energy leaving the plasma affect the device walls, and in turn how the plasma-wall interaction affects device performance and confinement.

Typically, the interaction between the confined plasma and the wall of the magnetic fusion device happens at locations specified by design, which in tokamaks are called divertor or limiter targets [5]. The magnetic field usually makes a shallow angle with these targets in order to minimize the heat flux onto the wall materials [6]. Motivated by this observation, in this thesis I study the plasma-wall boundary assuming that the magnetic field makes a small angle $\alpha \ll 1$ with the wall. With this magnetic field configuration, I focus on the boundary layer with characteristic thickness of the order of the ion gyroradius that forms near the wall, called the magnetic presheath, and assume that ions are collisionless in this thin region. This study is applicable to other systems: near spacecraft [7], plasma thrusters [8], probes [9] and magnetic filters [10].

The rest of this introductory chapter is structured as follows. In Section 1.1, I discuss the basic physics of plasma-wall interaction and introduce the boundary layers present next to the wall. In Section 1.2 I describe the magnetic presheath and explain the structure of the thesis.

1.1 Plasma-wall interaction

When a steady-state plasma is in contact with a wall, a potential difference between the bulk plasma and the wall is present which depends on the density and temperature

of the plasma and on the current flowing from the plasma to the wall. This potential drop forms due to the difference in mobility between ions and electrons. When quasineutral plasma is placed in contact with a wall, electrons usually reach the wall faster and thus charge it negatively [11], leaving a thin layer of plasma next to the wall, called the “Debye sheath”, to be positively charged. The Debye sheath has a thickness of several Debye lengths $\lambda_D = \sqrt{e^2 n_e / \epsilon_0 T_e}$, where e is the proton charge, n_e is the number density of electrons in the plasma, ϵ_0 is the permittivity of free space and T_e is the electron temperature. Most of the wall charge is shielded from the bulk plasma by the Debye sheath, allowing a steady-state in which most of the electrons are repelled from the wall while the ions are accelerated towards the wall.

Some of the electrostatic potential difference between wall and plasma occurs in a quasineutral “presheath”, of size $\lambda_{ps} \gg \lambda_D$. Usually $\lambda_{ps} \ll a$, where a is the scale of the device (for example, the minor radius of a tokamak), which implies that the presheath can be treated as a thin boundary layer with respect to the bulk plasma. The validity of two-scale theories that exploit the limit $\lambda_D / \lambda_{ps} \rightarrow 0$ has been justified by Riemann [12, 13]. In unmagnetized plasmas, or magnetized plasmas in which the magnetic field is normal to the wall, the size of the presheath is determined by the ion collisional mean free path, λ_{mfp} . When a magnetic field is present, the ion motion perpendicular to the magnetic field is confined within a gyroradius ρ_i , while ions are free to move parallel to the magnetic field. The ions are considered magnetized if $\rho_i \ll \lambda_{mfp}$, and thus travel in the direction parallel to the magnetic field for a distance of the order of a mean free path before colliding. If the magnetic field makes an oblique angle α with the wall, the ion gyro-orbit touches the wall when it is a gyroradius ρ_i away from it. The mean displacement of an ion between collisions (λ_{mfp} parallel to the magnetic field) projected in the direction normal to the wall is $\lambda_{mfp} \sin \alpha$. This length scale sets the size of the

boundary layer in which the transition from a collisional to a collisionless plasma occurs.

Thus, there are two presheath length scales: $\lambda_{\text{mfp}} \sin \alpha$ and ρ_i .

I consider the fusion-relevant case of a magnetic field impinging on the wall at a shallow angle, $\alpha \ll 1$. The size of the collisional length scale at such a small angle is $\lambda_{\text{mfp}} \sin \alpha \simeq \alpha \lambda_{\text{mfp}}$. Moreover, I consider a plasma-wall boundary that satisfies the scale separation

$$\lambda_D \ll \rho_i \ll \alpha \lambda_{\text{mfp}}. \quad (1.1)$$

As shown in Figure 11, with this scale separation, the presheath can be split into two separate layers: a “collisional presheath” of size $\alpha \lambda_{\text{mfp}}$ and a collisionless “magnetic presheath” of size ρ_i [14]. The ion motion in the two layers has a very different nature: in the collisional layer, ions are magnetized in circular gyro-orbits and stream parallel to the magnetic field; in the magnetic presheath, ion gyro-orbits are distorted by increasingly strong electric fields. In the Debye sheath, ions are accelerated towards the wall by an electric force much larger than the magnetic force. In Appendix A I justify the ordering (1.1) in the context of a typical tokamak plasma. A cartoon of the ion motion across all boundary layers is shown in Figure 11.

There is a vast literature that treats the plasma-wall boundary using fluid equations [15–20]. Although, with due care, fluid equations may capture well most of the underlying physics, it is widely accepted that a kinetic treatment should be carried out to describe the plasma-wall boundary, which is kinetic in nature from the collisional layer to the wall. For example, Siddiqui *et al* [21] argue, using experimental measurements of ion flows in three dimensions near the plasma-wall boundary, that a kinetic theory of ions and neutrals is necessary in the boundary layer in order to accurately predict the location and intensity of ion and charge exchanged neutral fluxes to the wall.

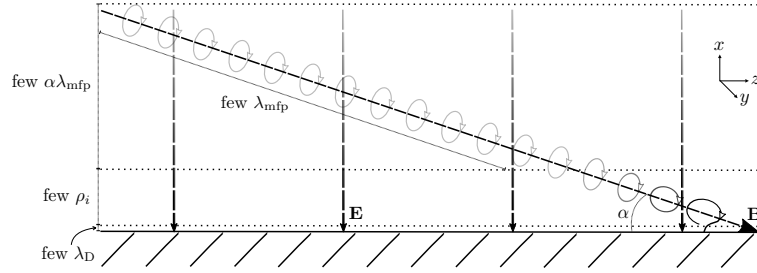


Figure 11: Cartoon of ion orbits in the neighbourhood of the divertor target of a tokamak plasma, with $\lambda_D \ll \rho_i \ll \alpha \lambda_{mfp}$. The orbits have a size ρ_i and are tied to a dashed line representing the magnetic field \mathbf{B} , which is inclined at an angle α with the wall. The electric field \mathbf{E} is shown as a dashed vertical line, and is shaded darker nearer to the wall, where it is stronger. Highly distorted orbits in the magnetic presheath are black, while circular orbits in the collisional presheath are light grey.

Most of the existing kinetic solutions to plasma-wall boundary layers are numerical and use Particle-in-Cell (PIC) codes [22–25], although some use Eulerian-Vlasov advection schemes [26–29]. Analytical kinetic treatments of the plasma-wall boundary are more rare [30–37]. They often provide more insight, although generally suffer from the limitation of making oversimplifying assumptions and/or solving the problem only partially. A combination of robust analytical work supported by numerical solutions is often the best compromise.

A kinetic treatment of the collisional presheath must describe the transition from collisional to collisionless ions and electrons, while retaining the effect of magnetic and electric forces on each individual particle. A conventional drift-kinetic or gyrokinetic ordering [38–40] is expected to hold for both ions and electrons in the collisional presheath, which can be used to substantially simplify the particle trajectories. Apart from this simplification, a kinetic theory of this layer remains complicated and dependent on the dominant collision process.

Kinetic treatments of the collisionless layers (magnetic presheath and Debye sheath)

are simplified by the absence of collisions. However, compared with the Debye sheath, an ion kinetic treatment in the magnetic presheath is complicated by the role of the oblique magnetic field, which exerts dynamically important forces on the ions. Electric forces perpendicular to the wall dominate the ion dynamics in the Debye sheath; hence, the change in electrostatic potential energy of an ion is equal to the change in kinetic energy of the component of the ion velocity normal to the wall. In the magnetic presheath, the typical size of electric and magnetic forces acting on an ion are similar; hence, the kinetic energy of each ion is continuously transferred between the three velocity components and the electrostatic potential. From this discussion, it is clear that two co-ordinates are sufficient to describe ion motion in the Debye sheath: the distance from the wall, x , and the velocity component normal to the wall, v_x . Conversely, a kinetic treatment of ions in the magnetic presheath requires two additional velocity co-ordinates to describe the ion dynamics in the plane parallel to the wall (even when the system is translationally invariant in the directions parallel to the wall). Hence, a kinetic treatment of the magnetic presheath offers a substantial analytical and numerical challenge, which is addressed by this thesis.

1.2 The magnetic presheath

The magnetic presheath was first studied by Chodura [15]. For this reason, it is often referred to as the “Chodura sheath” in the literature, although it has also been referred to as the “gyrosheath” [41]. Chodura used fluid equations for the electrons and ions, which are valid provided ions are much colder than electrons. He thus found a solution for the electrostatic potential and ion flow across the magnetic presheath. Chodura also found that, for cold ions, the ion flow parallel to the magnetic field at the presheath entrance

must at least be equal to the Bohm speed

$$v_B = \sqrt{\frac{ZT_e}{m_i}}, \quad (1.2)$$

which is known as the Chodura (or Bohm-Chodura) condition [15, 16]. In equation (1.2), Z is the ion charge as a multiple of the proton charge e , and m_i is the ion mass. Bohm [42] first obtained a similar condition at the entrance of the Debye sheath, where he concluded that the ions enter with a normal velocity component at least equal to v_B . Hence, the ion fluid velocity in the magnetic presheath is turned by the strong electric field from being parallel to the magnetic field to being normal to the wall. Chodura also predicted that the electrostatic potential drop across the magnetic presheath is approximately $(T_e/e) \ln(1/\sin \alpha)$. His predictions were supported by PIC simulations.

The problem of how an oblique magnetic field influences the plasma-wall interaction and the plasma-wall boundary conditions has been of interest and is yet to be fully resolved. After Chodura, many other studies of the magnetic presheath that also used fluid equations to model the ion species have been carried out [16, 20, 43, 44]. The main results and the physical picture provided by Chodura survived. After the work of Stangeby and Chankin [18], who incorporated the $\mathbf{E} \times \mathbf{B}$ drifts expected in the magnetic presheath (due to, for example, turbulence in the scrape-off-layer) and thus generalized Chodura's condition, Loizu [14] obtained a set of boundary conditions for fluid models of the Scrape-Off-Layer. The problem of an ion fluid model is that it cannot accurately describe fluid quantities across the magnetic presheath, since kinetic effects due to the finite ion Larmor radius and due to the width of the ion distribution function are neglected. For example, an ion that is initially at a distance ρ_i from the wall may or may not reach the wall before completing a gyration depending on its initial velocity, which in turn also affects the velocity of the ion at the wall. Moreover, ion Larmor orbits have

a characteristic radius of the order of the length scale of variation of the electric field, and are thus highly distorted [41]. A fluid description can only be used when $T_i \ll T_e$, where T_i is the ion temperature, because such ions can be treated as mono-energetic and with zero Larmor radius. Several kinetic treatments of the ions in the magnetic presheath have been carried out [32–37, 45], all of which have made significant progress in our understanding of the magnetic presheath. With this thesis, I hope to make further progress by providing a complete kinetic theory of ions in the magnetic presheath based on an asymptotic expansion and a numerical procedure that is efficient and requires very little computational power.

In this thesis, I do not consider the effect of kinetic electrons and take a Boltzmann electron distribution across the magnetic presheath, as is done in most other studies. This relies on the assumptions that the electron distribution function entering the magnetic presheath is Maxwellian, and that the potential drop across the Debye sheath repels most of the electrons away from the wall. I derive the electron-repelling magnetic presheath equations valid for general $T_i \sim T_e$ by retaining the full ion distribution function and exploiting an asymptotic expansion in the small angle α . This work is consistent with the qualitative picture of fluid models of the electron-repelling magnetic presheath, with a quantitative modification of the electrostatic potential and ion flow profiles. Additionally, the ion distribution function at the entrance of the Debye sheath is obtained from the ion distribution function entering the magnetic presheath. The distribution function at the entrance of the Debye sheath is found to be narrower when the angle α is smaller. A kinetic solution of the Debye sheath, as shown in reference [46], can be used to obtain the ion distribution function at the wall from the distribution function at the Debye sheath entrance. The distribution of ion velocities at the wall is important because the sputtering yield of each ion depends on its kinetic energy and its angle of impact with

the wall, and thus sputtering — which is a source of impurities in the plasma — can be predicted from the ion distribution function.

When the angle between the magnetic field and the wall is sufficiently small and/or there is a sufficiently large electron current to the wall, the strongly electron-repelling model of the magnetic presheath is invalid (see the discussion in section 4.1) [47]. In order to further improve the models of plasma-wall interaction at grazing angles, a kinetic description of the electrons is therefore necessary. The strongly electron-repelling assumption can only break down if $T_i \neq 0$, and thus an essential prerequisite of any improved model is to have a kinetic description of the ions. Therefore, the theory presented in this thesis is crucial for future models of the collisionless boundary layers that do not assume an electron-repelling Debye sheath. With the inclusion of a kinetic description of the electrons, and a solution of the Debye sheath [46] and magnetic presheath, one could reliably obtain the relationship between current through the plasma and electrostatic potential drop across the collisionless sheath and presheath at small angles. This relationship could provide a simple boundary condition to drift-kinetic models describing the plasma in the Scrape-Off-Layer. The equations derived herein for the ion density in the magnetic presheath can also be used to obtain the electron density in the Debye sheath when the electron finite Larmor orbit effects are important $\rho_e \gtrsim \lambda_D$. In previous studies, finite Larmor orbit effects are often neglected $\rho_e \ll \lambda_D$ [14, 33] or considered using the assumption that $\rho_e \gg \lambda_D$ [48].

The thesis is structured as follows. In chapter 2, I solve for the ion trajectories by using an asymptotic expansion for $\alpha \sim \delta \ll 1$, which is equivalent to a gyrokinetic separation of timescales. In chapter 3, I solve for the ion distribution function and density in the magnetic presheath. Up to this point, my equations also include the effect of the small turbulent electric fields parallel to the wall, ordered smaller than the electric

field normal to the wall by a factor $\delta \ll 1$ as was done in reference [14]. In chapter 4, I close the system of equations derived in the previous chapters using the quasineutrality equation, and subsequently consider a magnetic presheath with no gradients parallel to the wall ($\delta = 0$). After a detailed kinetic analysis of the Debye sheath and magnetic presheath entrance conditions, I present numerical solutions for different values of α . In chapter 5, I study the dependence of the magnetic presheath results on the ion temperature. Finally, in chapter 6 I conclude by summarizing and discussing my work¹.

¹Much of the material presented in this thesis appears in references [49, 50].

CHAPTER 2

Ion trajectories

The ion trajectories are necessary in order to solve the ion kinetic equation in the magnetic presheath and thus obtain the ion density. In this chapter I solve for the ion motion in the magnetic presheath assuming that:

- the angle between the magnetic field and the wall is small, $\alpha \ll 1$;
- variations parallel to the wall are in the cross-field direction only, with a characteristic length scale l much longer than the ion gyroradius ρ_i , such that $\delta = \rho_i/l \ll 1$.

In Section 2.1 I introduce and explain the orderings of all quantities. In Section 2.2 I solve for periodic ion trajectories in a system in which the magnetic field is exactly parallel to the wall ($\alpha = 0$) with no gradients in the direction parallel to the wall ($\delta = 0$). Finally, in Section 2.3, I use the asymptotic expansion in $\alpha \sim \delta \ll 1$ to solve for the approximate ion trajectories in a grazing angle magnetic presheath with weak turbulent gradients parallel to the wall.

2.1 Orderings

I denote the electric and magnetic fields in the magnetic presheath as \mathbf{E} and \mathbf{B} respectively, and use the coordinate axes in Figure 11. The magnetic field is

$$\mathbf{B} = B \cos \alpha \hat{\mathbf{z}} - B \sin \alpha \hat{\mathbf{x}}, \quad (2.1)$$

where $\hat{\mathbf{x}}$ is the unit vector in the x direction, normal to the wall, and $\hat{\mathbf{z}}$ is a unit vector parallel to the wall. Throughout this work I assume a negatively charged, electron repelling wall, valid if the time it takes for the electrons to reach the wall is shorter than the time it takes for the ions. The criterion required for assuming an electron-repelling wall is quantified in chapter 4.

The gyrofrequency of an ion orbit in a constant and uniform magnetic field is

$$\Omega = \frac{ZeB}{m_i}, \quad (2.2)$$

where $Z \sim 1$ is the ion atomic number and e is the proton charge. As we will see, orbit distortion in the magnetic presheath changes the exact value of the gyrofrequency, whose size nonetheless remains of order Ω . The individual ion velocity is ordered

$$|\mathbf{v}| \sim v_x \sim v_y \sim v_z \sim v_{t,i} = \sqrt{\frac{2T_i}{m_i}}, \quad (2.3)$$

where $v_{t,i}$ is the thermal velocity. The thermal gyroradius, which is the typical size of an ion orbit, is defined as

$$\rho_i = \frac{v_{t,i}}{\Omega}. \quad (2.4)$$

As we will see in chapter 5, the magnetic presheath has a characteristic thickness of the order of the ion sound Larmor radius

$$\rho_s = \sqrt{\frac{ZT_e + T_i}{m_i}}. \quad (2.5)$$

In this chapter, and in chapters 3 and 4, I will consider magnetic presheaths with $T_e \sim T_i$, and thus with $\rho_s \sim \rho_i$. Such magnetic presheaths have a characteristic thickness of the order of the thermal ion Larmor radius ρ_i .

The characteristic length perpendicular to the wall is set by the ion gyroradius $\sim \rho_i$. The characteristic lengths parallel to the wall are constrained by the size of the turbulent structures in the scrape-off-layer (SOL) [51], which are assumed much larger than ρ_i . The z direction is mostly along the magnetic field, a direction in which turbulent structures are elongated, while the y direction is mostly across the magnetic field. From this, I argue in Appendix B that gradients in the z direction must be ordered smaller than in the y direction. I thus take the orderings

$$x \sim \rho_i \ll y \sim l \ll z \sim l/\alpha \sim l/\delta \quad (2.6)$$

for the length scales associated with the different coordinate directions, where l is the characteristic cross-field size of turbulent structures in the SOL and $\delta = \rho_i/l \ll 1$ is a small parameter relating the different length scales. From reference [52], I estimate $l \sim 10$ mm in a typical tokamak, which leads to $\delta \sim 0.07$, which is indeed small. I take the maximal ordering

$$\alpha \sim \delta \quad (2.7)$$

throughout this chapter and chapter 3. From section 4.2 of chapter 4 and throughout chapter 5, I take the ordering $\delta \ll \alpha$, effectively setting $\delta = 0$ and ignoring gradients parallel to the wall.

The external magnetic field \mathbf{B} is assumed constant in space and time. This is justified in the context of a fusion device because the length scale of \mathbf{B} is set by the curvature of the device, which is typically much larger than l , and the time variations of this field are

also expected to be negligible. I make two further assumptions which are justified in the last few paragraphs of this section. Firstly, I assume that the magnetic fields produced by currents in the magnetic presheath plasma are so small compared to the external magnetic field that they can be neglected. Secondly, I assume that the plasma in the magnetic presheath is electrostatic, $\mathbf{E} = -\nabla\phi$, where ϕ is the electrostatic potential.

The electrostatic potential changes in the magnetic presheath are ordered

$$\phi \sim \frac{T_e}{e}. \quad (2.8)$$

The ordering (2.8) is expected from a magnetic presheath in which electrons are being repelled from the wall, and is consistent with the potential drop across the magnetic presheath being $\sim (T_e/e) \ln(1/\alpha)$ as predicted by fluid treatments [15]. The ion and electron temperatures are ordered to be of similar size, $T_i \sim T_e \sim T$. From the ordering of the potential (2.8) and the length scales (2.6), the size of the electric field components is

$$\frac{\partial\phi}{\partial z} \sim \frac{\delta T}{el} \sim \frac{\alpha T}{el} \ll \frac{\partial\phi}{\partial y} \sim \frac{T}{el} \ll \frac{\partial\phi}{\partial x} \sim \frac{T}{e\rho_i}. \quad (2.9)$$

The strong electric field normal to the wall leads to an $\mathbf{E} \times \mathbf{B}$ drift in the y direction comparable with the ion thermal velocity, $(1/B)\partial\phi/\partial x \sim v_{ti}$. Because potential gradients in this direction are small, the drifting particles will be exposed to significant potential changes only after a timescale much longer than the period of gyration. This means that the effect of this drift is unimportant to lowest order. The electric field component $\partial\phi/\partial y$ parallel to the wall leads to an $\mathbf{E} \times \mathbf{B}$ drift in the x direction, normal to the wall, that is first order in δ . Therefore, ions drift towards or away from the wall at a speed $\sim \delta v_{ti}$. This drift competes with the projection of the parallel flow towards the wall $\sim \alpha v_{ti}$ when we take the maximal ordering $\delta \sim \alpha$, consistent with reference [14].

Parallel streaming and the presence of an absorbing wall leads to an expected ion flow $\sim v_{t,i}$ in the z direction. From (2.3) and (2.9), potential changes due to motion in the z direction happen over a timescale so much longer than the orbital timescale that their effect is small even to first order in $\delta \sim \alpha$.

The magnetic presheath has a size ρ_i . Considering that the drift in the x direction is of order $\delta v_{t,i} \sim \alpha v_{t,i}$, the characteristic time t_{MPS} that it takes for an ion to reach the wall after having entered the magnetic presheath is expected to be $\rho_i / \delta v_{t,i} \sim \rho_i / \alpha v_{t,i}$, which becomes

$$t_{\text{MPS}} \sim \frac{1}{\Omega \delta} \sim \frac{1}{\Omega \alpha}. \quad (2.10)$$

The size of the time derivative $\partial/\partial t$ is set by the turbulence in the SOL, and is given by (see Appendix B)

$$\frac{\partial}{\partial t} \sim \delta^2 \Omega. \quad (2.11)$$

Because this partial derivative is higher order compared to $1/t_{\text{MPS}}$, it is negligible. From (2.3) and (2.6), the gradients in the z direction are also negligible because

$$v_z \frac{\partial}{\partial z} \sim \alpha^2 \Omega \sim \delta^2 \Omega. \quad (2.12)$$

Ions and electrons $\mathbf{E} \times \mathbf{B}$ drift in the same direction, so their contributions to the current partially cancel each other. However, because ions have a large Larmor orbit, they experience a strongly varying electric field over an orbit. Therefore, their $\mathbf{E} \times \mathbf{B}$ drift in the y direction can differ from the electron one substantially, which leads to a large current density $j_y^D \sim e n_i v_{t,i}$ in this direction. Here, n_i is the ion density. The “D” superscript denotes current that is produced by the particle drifts in the plasma. This estimate for j_y^D also follows from analyzing the size of diamagnetic ion and electron

flows parallel to the wall [20]. The order of magnitude of the diamagnetic current in the y direction is $(1/B^2)(\mathbf{B} \times \nabla p)_y \sim (1/B)\partial p/\partial x \sim en_i v_{ti}$, where $p \sim m_i n_i v_{ti}^2$ is the plasma pressure. From the ordering of the plasma flow in the x direction, the size of the current normal to the wall is expected to be $j_x^D \sim \delta en_i v_{ti} \sim \alpha en_i v_{ti}$. Again, this also follows by considering the component of the diamagnetic current in the x direction, $(1/B^2)(\mathbf{B} \times \nabla p)_x \sim (1/B)\partial p/\partial y \sim \delta en_i v_{ti}$.

I proceed to demonstrate that the neglect of magnetic fields produced by magnetic presheath currents and the electrostatic assumption are both justified. For the remainder of this section (and in Appendix C), I refer to the constant externally produced field as \mathbf{B}^c . From my choice of axes (see Figure 11), $B_x^c = -B^c \sin \alpha \sim \alpha B^c$, $B_y^c = 0$, $B_z^c = B^c \cos \alpha \sim B^c$. The plasma current \mathbf{j}^D in the boundary layer can produce a magnetic field \mathbf{B}^p . Using (2.6), $\nabla \cdot \mathbf{B}^p = 0$ gives

$$B_x^p \sim \delta^2 B^p \sim \delta \alpha B^p \ll B_y^p \sim \delta B^p \sim \alpha B^p \ll B_z^p \sim B^p. \quad (2.13)$$

Ampère's law is

$$\mu_0 \mathbf{j}^D = \nabla \times \mathbf{B}^p, \quad (2.14)$$

where μ_0 is the vacuum permeability. Using (2.6) and (2.13) to order the right hand side of (2.14), the orderings

$$j_x^D \sim j_z^D \sim \frac{B^p}{\mu_0 l} \ll j_y^D \sim \frac{B^p}{\mu_0 \rho_i} \quad (2.15)$$

are obtained. The earlier orderings for the current deduced from particle motion ($j_x^D \sim \delta en_i v_{ti} \sim \alpha en_i v_{ti}$ and $j_y^D \sim en_i v_{ti}$) are consistent with equation (2.15) if we take $j_z^D \sim j_x^D \sim \delta en_i v_{ti} \sim \alpha en_i v_{ti}$. This ordering is consistent with what is expected from the piece of the parallel current produced in response to the perpendicular currents resulting from

particle drifts (an analogue of the Pfirsch-Schlüter current [53]).¹ From these estimates of the currents, it follows that

$$\frac{B^p}{B^c} \sim \beta \ll 1, \quad (2.16)$$

where $\beta = 2\mu_0 p / (B^c)^2$ is the plasma beta parameter. This parameter is typically small in the core and is even smaller in the SOL ($\beta \sim 0.004$ inferred from reference [54]), so that the field produced by the plasma in the magnetic presheath is much smaller than the externally generated one.

In order to neglect the plasma produced magnetic field, I require each component of it to be negligible compared to either the respective component or the smallest retained component of the external magnetic field \mathbf{B}^c . Considering the non-zero components of \mathbf{B}^c (the z and x components), the orderings $B_z^p \sim B^p \ll B_z^c \sim B^c$ and $B_x^p \sim \delta\alpha B^p \ll B_x^c \sim \alpha B^c$ are required, which are both satisfied if the inequality (2.16) holds. In addition to this we require that $B_y^p \ll B_x^c$ (because B_x^c is the smallest retained component of the external magnetic field), which is satisfied if (2.16) holds. This discussion justifies taking $\mathbf{B} = \mathbf{B}^c = \text{constant}$ in my equations and hence neglecting all plasma produced magnetic field components.

The electrostatic approximation is valid if each component of the *non-electrostatic* piece, \mathbf{E}^p , of the electric field (which is induced by the plasma produced magnetic fields) is negligible compared to either the respective component or the smallest retained component of the *electrostatic* piece, $-\nabla\phi$, of the electric field. The smallest retained component of the electric field is $\partial\phi/\partial y \sim T_e/el$ because $\partial\phi/\partial z$ will be neglected, as discussed earlier. With this consideration and using (2.9), $E_x^p \ll T/e\rho_i \sim v_{ti}B^c$,

¹This does not imply, as discussed in the last paragraph of Section 2 and in Appendix C, that larger parallel currents cannot be present in the magnetic presheath.

$E_y^p \ll T/el \sim \delta v_{ti} B^c$ and $E_z^p \ll T/el \sim \delta v_{ti} B^c$ are required in order to justify the electrostatic approximation. The induction equation is

$$\frac{\partial \mathbf{B}^p}{\partial t} = -\nabla \times \mathbf{E}^p. \quad (2.17)$$

Using (2.11) and (2.13) to order the left hand side, and (2.6) to order the partial derivatives on the right hand side of (2.17), I obtain an ordering for the induced electric field components,

$$E_z^p \sim \delta^2 E^p \sim \delta \alpha E^p \ll E_y^p \sim \delta E^p \ll E_x^p \sim E^p \sim \delta v_{ti} B^p. \quad (2.18)$$

In order to neglect E_x^p and E_y^p compared to their electrostatic counterparts I require $\delta B^p \ll B^c$, which is automatically satisfied if (2.16) holds. It follows that E_z^p can also be neglected, because $E_z^p \ll E_y^p$ (from (2.18)) and the neglect of E_y^p has been justified. This discussion justifies the electrostatic approximation and hence the use of $\mathbf{E} = -\nabla \phi$ in the equations of this paper.

Note that my orderings do not preclude a larger parallel current \mathbf{j}^L (e.g. due to divertor target potential bias, Edge Localized Mode disruptions [55], etc.) with $j_x^L = -j^L \sin \alpha$, $j_y^L = 0$ and $j_z^L = j^L \cos \alpha$, provided that the magnetic field produced by the plasma in the magnetic presheath remains much smaller than the external one and that the electrostatic assumption remains valid. In order for our approximations to be valid, such a current would have to satisfy $\nabla \cdot \mathbf{j}^L = 0$ independently of \mathbf{j}^D . In Appendix C, I show that my equations allow for a parallel current density of size $j^L \ll (\alpha/\beta) \delta n_i v_{ti}$. This current density can be large, $j^L \gg j_z^D \sim \delta n_i e v_{ti}$, because $\alpha \sim 0.1 \gg \beta \sim 0.004$ in the magnetic presheath.

To conclude, in this section I have justified and introduced the following assumptions and orderings:

- The magnetic field \mathbf{B} is uniform and constant in time, making a small angle $\alpha \ll 1$ with the wall;
- the electric field is described by an electrostatic potential $\phi(x, y)$;
- the scale length of variation perpendicular to the wall is set by the size of the ion gyro-orbits, ρ_i ;
- turbulent variations in the plane parallel to the wall are constrained to the direction perpendicular to the magnetic field, with a typical length scale l longer than the ion gyroradius ρ_i such that $\delta = \rho_i/l \ll 1$.

2.2 Periodic orbits

When $\alpha = \delta = 0$, the uniform magnetic field is parallel to the wall and the system is translationally invariant in the plane parallel to the wall. I proceed to study ion trajectories in this system, as a lowest order solution to the ion trajectories in the magnetic presheath, where $\alpha \sim \delta \ll 1$. Section 2.2.1 is devoted to obtaining constants of the ion motion in such a system. Using these constants of the motion, the ion velocity is expressed in terms of the instantaneous position and the orbit parameters, using an “effective potential”. In Section 2.2.2 I introduce two distinct types of effective potential curves. In Section 2.2.3 I briefly discuss periodic solutions to the equations of motion with $\alpha = \delta = 0$.

2.2.1 Orbit parameters

The equations of motion for an ion moving in the collisionless magnetic presheath are [49]

$$\dot{x} = v_x, \quad (2.19)$$

$$\dot{y} = v_y, \quad (2.20)$$

$$\dot{z} = v_z, \quad (2.21)$$

$$\dot{v}_x = -\frac{\Omega}{B} \frac{\partial \phi}{\partial x} + \Omega v_y \cos \alpha, \quad (2.22)$$

$$\dot{v}_y = -\frac{\Omega}{B} \frac{\partial \phi}{\partial y} - \Omega v_x \cos \alpha - \Omega v_z \sin \alpha, \quad (2.23)$$

$$\dot{v}_z = -\frac{\Omega}{B} \frac{\partial \phi}{\partial z} + \Omega v_y \sin \alpha, \quad (2.24)$$

where a dot denotes a time derivative, d/dt . Setting $\alpha = 0$ and $\delta = 0$, equations (2.22)-(2.24) become

$$\dot{v}_x = -\frac{\Omega}{B} \frac{\partial \phi}{\partial x} + \Omega v_y, \quad (2.25)$$

$$\dot{v}_y = -\Omega v_x, \quad (2.26)$$

$$\dot{v}_z = 0. \quad (2.27)$$

Using (2.19), direct integration of (2.26) leads to

$$\bar{x} = \frac{v_y}{\Omega} + x \sim \rho_i, \quad (2.28)$$

where \bar{x} is the constant of integration which represents the position of an ion orbit. The statement that $\bar{x} \sim \rho_i$ is understood to mean “the typical changes of the value of \bar{x} (that occur as ions move in the magnetic presheath) are of the order of ρ_i ”. Multiplying (2.25) by v_x and adding it to (2.26) multiplied by v_y , we obtain $\dot{U}_\perp = 0$, where

$$U_\perp = \frac{1}{2}v_x^2 + \frac{1}{2}v_y^2 + \frac{\Omega\phi}{B} \sim v_{ti}^2 \quad (2.29)$$

is the perpendicular energy. From (2.27), the parallel velocity v_z of the ion is a constant of the motion. Adding the parallel kinetic energy $v_z^2/2$ to the perpendicular energy, we obtain the total energy,

$$U = \frac{1}{2}v_x^2 + \frac{1}{2}v_y^2 + \frac{1}{2}v_z^2 + \frac{\Omega\phi}{B} \sim v_{ti}^2. \quad (2.30)$$

The quantities \bar{x} , U_\perp and U constitute the orbit parameters of ion motion. When $\alpha = \delta = 0$ they are exactly conserved, and when $\alpha \sim \delta \ll 1$ they change slowly (except for U which remains constant).

The ion velocity components v_x , v_y and v_z can be expressed in terms of the orbit parameters and the instantaneous ion position x . Inserting (2.28) into (2.29) and rearranging gives

$$v_x = \sigma_x V_x(x, y, \bar{x}, U_\perp) \text{ with } V_x(x, y, \bar{x}, U_\perp) = \sqrt{2(U_\perp - \chi(x, y, \bar{x}))}, \quad (2.31)$$

where I introduced $\sigma_x = \pm 1$ to account for the two possible signs of v_x , and an effective potential function

$$\chi(x, y, \bar{x}) = \frac{1}{2}\Omega^2(x - \bar{x})^2 + \frac{\Omega\phi(x, y)}{B}. \quad (2.32)$$

The dependence on z is negligible even to first order in δ , and therefore it is omitted. The y -component of the velocity is obtained by rearranging equation (2.28),

$$\dot{y} = v_y = \Omega(\bar{x} - x). \quad (2.33)$$

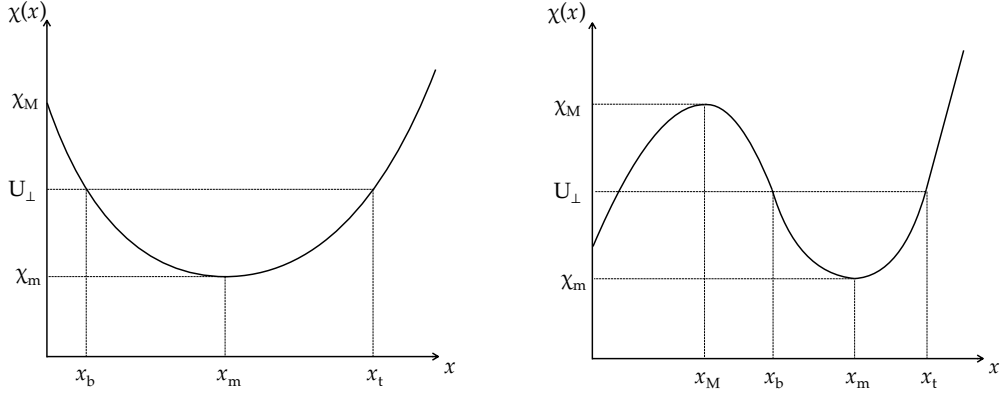


Figure 21: Type I (left) and II (right) effective potential curves, both with a stationary point corresponding to a minimum at $x = x_m$. A type II curve is characterized by a stationary point corresponding to a maximum at $x = x_M$. These curves allow closed orbits for any value of U_\perp in the range $\chi_m(y, \bar{x}) \leq U_\perp \leq \chi_M(y, \bar{x})$ with bottom and top bounce points at positions x_b and x_t .

The z -component of the velocity is obtained by subtracting equation (2.29) from (2.30), multiplying by 2 and taking a square root,

$$v_z = \sigma_\parallel V_\parallel(U_\perp, U) \text{ with } V_\parallel(U_\perp, U) = \sqrt{2(U - U_\perp)}, \quad (2.34)$$

where $\sigma_\parallel = \pm 1$ is the sign of v_z .

2.2.2 Types of effective potential curves

By imposing that v_x be real in equation (2.31), I find that the allowed ion positions must satisfy $U_\perp \geq \chi(x; y, \bar{x})$. A particle moves periodically if, for given values of U_\perp and \bar{x} , it is trapped around a minimum (with respect to x) of the effective potential $\chi(x; y, \bar{x})$. Then, the ion motion is confined between bounce points x_b (bottom) and x_t (top) defined by (see Figure 21)

$$U_\perp = \chi(x_b; y, \bar{x}) = \chi(x_t; y, \bar{x}) \text{ with } x_b \leq x_t. \quad (2.35)$$

Throughout this work, the electrostatic potential across the magnetic presheath is assumed to be such that $\phi(x, y)$, $\partial\phi(x, y)/\partial x$ and $\partial^2\phi(x, y)/\partial x^2$ are all monotonic as a function of x , as shown in Figure 22. My numerical results, presented in chapters 4 and 5 and obtained with no y -dependence ($\delta = 0$), satisfy these monotonicity conditions. Then, for values of \bar{x} and y for which the effective potential has a minimum, there are two possible types of effective potential $\chi(x; y, \bar{x})$:

- a type I effective potential has one stationary point, corresponding to a minimum at x_m , such that $\chi_m(\bar{x}, y) \equiv \chi(x_m; y, \bar{x})$, and *no* other stationary point — in this case, it is important to consider the local maximum at position $x_M = 0$ (which is *not* a stationary point) with $\chi_M(\bar{x}, y) = \chi(0, \bar{x}, y)$;
- a type II effective potential has two stationary points: one at position x_m which corresponds to a minimum $\chi_m(\bar{x}, y)$, and one at position x_M which corresponds to a maximum $\chi_M(y, \bar{x}) \equiv \chi(x_M; y, \bar{x})$.

These two types of effective potential are shown in Figure 21. I will refer to the ion trajectories arising due to each curve type as type I and type II orbits.

I proceed to obtain the range of values of \bar{x} for which the effective potential is of either type, and to give a physical explanation of the difference between the two types of curves. Differentiating equation (2.32) with respect to x , we obtain

$$\frac{\partial\chi}{\partial x}(x; y, \bar{x}) = \Omega^2(x - \bar{x}) + \frac{\Omega}{B} \frac{\partial\phi}{\partial x}(x, y). \quad (2.36)$$

Substituting $v_y = \Omega(\bar{x} - x)$ into equation (2.25), which is valid to lowest order in α and δ , one sees that $-\partial\chi(x; y, \bar{x})/\partial x$ coincides with the acceleration of an ion at that point, in the x direction. Indeed, the magnetic force in the x direction is, to lowest order in α and δ , given by $m_i\Omega v_y = m_i\Omega^2(\bar{x} - x)$ and the electric force is $-m_i\Omega\phi'(x, y)/B$.

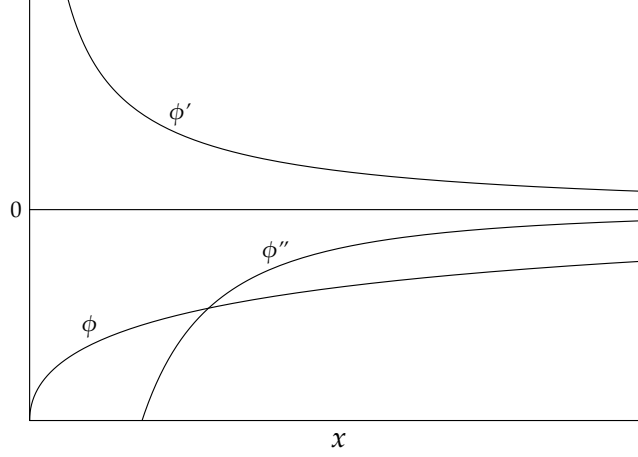


Figure 22: An example of a monotonic electrostatic potential profile $\phi(x)$ and its monotonic first and second derivatives $\phi'(x)$ and $\phi''(x)$.

Consider an ion that reaches the point $x = 0$. For type I curves the gradient of the effective potential at $x = 0$ must be negative. Hence, from equation (2.36), we obtain $-\Omega^2 \bar{x} + \Omega \phi'(0, y)/B < 0$ which leads to the requirement that $\bar{x} > \bar{x}_{m,I}(y)$ with

$$\bar{x}_{m,I}(y) = \frac{\phi'(0, y)}{\Omega B}. \quad (2.37)$$

Physically, the difference between type I and type II curves only manifests itself only when the ion reaches the region $x \leq x_M$, and therefore always manifests itself at $x = 0$. For type I curves, the magnetic force directed away from the wall at $x = 0$ is larger than the electric force towards the wall. For type II curves, the opposite is true and the electric force towards the wall is larger than the magnetic force turning the ions away from the wall at $x = 0$.

Setting equation (2.36) to zero gives an equation for the stationary points of χ , which can be rearranged to

$$\frac{\partial \phi}{\partial x}(x, y) = \Omega B (\bar{x} - x). \quad (2.38)$$

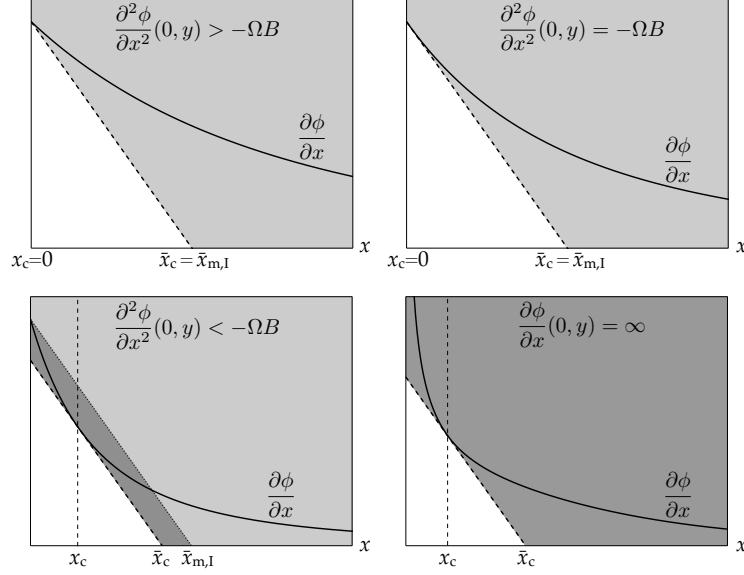


Figure 23: The stationary points of the effective potential satisfy equation (2.38), $\partial\phi/\partial x = \Omega B (\bar{x} - x)$. In each of the four diagrams the solid curves represent $\partial\phi/\partial x$, the oblique dashed lines are $\Omega B (\bar{x} - x_c)$, while the additional oblique dotted line in the bottom-left diagram is $\Omega B (\bar{x} - x_{m,I})$. For given values of y and \bar{x} , equation (2.38) can have two solutions (dark grey region, χ is type II), one solution (light grey region, χ is type I) or no solution (unshaded region, χ has no minimum). The smallest value of \bar{x} for which a stationary point exists, at position $x_c(y)$, is $\bar{x}_c(y)$. The value of \bar{x} which corresponds to a stationary point at $x = 0$ is $\bar{x}_{m,I}(y)$.

The stationary points are minima if the second derivative of χ is positive. This condition is equivalent to the gradient of $\partial\phi(x, y)/\partial x$ with respect to x being larger than the gradient of the line $\Omega B (\bar{x} - x)$. By rearranging equation (2.38) to an equation for \bar{x} as a function of x and then minimizing it with respect to x , we obtain the minimum value of the orbit position $\bar{x}_c(y)$ for which the effective potential has a stationary point,

$$\bar{x}_c(y) \equiv \min_{x \in [0, \infty]} \left(x + \frac{\phi'(x, y)}{\Omega B} \right) \equiv x_c(y) + \frac{\phi'(x_c(y), y)}{\Omega B}. \quad (2.39)$$

Note that, in equation (2.39), I also defined the position $x_c(y)$ of the stationary point of the effective potential χ when $\bar{x} = \bar{x}_c(y)$. In Figure 23, $\bar{x}_c(y)$ is the smallest value of \bar{x} for

which the straight line $\Omega B(\bar{x} - x)$ touches the curve $\partial\phi(x, y)/\partial x$, and $x_c(y)$ is the value of x at which they intersect. From Figure 23, \bar{x}_c and $\bar{x}_{m,I}$ coincide if $\partial^2\phi(0, y)/\partial x^2 \geq -\Omega B$. Then, all effective potential curves are type I for $\bar{x} > \bar{x}_c(y) = \bar{x}_{m,I}(y)$. If $\partial^2\phi(0, y)/\partial x^2 < -\Omega B$, $\bar{x} = \bar{x}_c(y)$ is the orbit parameter value corresponding to when the straight line $\Omega B(\bar{x} - x)$ touches the curve $\partial\phi(x, y)/\partial x$ tangentially. Then, for orbit parameter values in the range $\bar{x}_c(y) \leq \bar{x} \leq \bar{x}_{m,I}(y)$, there are two stationary points (a minimum in the region $x > x_c(y)$ and a maximum in the region $0 \leq x < x_c(y)$), corresponding to type II curves, while for $\bar{x} > \bar{x}_{m,I}(y)$ there is only one minimum, corresponding to type I curves. Summarizing these observations with the aid of Figure 23:

- if $\partial^2\phi(0, y)/\partial x^2 \geq -\Omega B$, χ is a type I curve for $\bar{x} > \bar{x}_c(y) = \bar{x}_{m,I}(y)$;
- if $\partial^2\phi(0, y)/\partial x^2 < -\Omega B$, χ is a type II curve for $\bar{x}_c(y) < \bar{x} < \bar{x}_{m,I}(y)$ and a type I curve for $\bar{x} > \bar{x}_{m,I}(y)$.

In chapter 4 I set $\delta = 0$ and thus solve a magnetic presheath with no y -dependence. I will show that a self-consistent solution $\phi(x)$ of such a magnetic presheath requires the electric field to diverge at $x = 0$, $\partial\phi(0)/\partial x \rightarrow \infty$, which is confirmed numerically. Hence, the effective potential curves are type II for all values of \bar{x} larger than \bar{x}_c because $\bar{x}_{m,I} = (\partial\phi(0)/\partial x)/\Omega B \rightarrow \infty$ (see Figure 23, bottom-right diagram). It is nonetheless useful to consider also type I curves because I obtain my numerical solution by iterating over possible electrostatic potential profiles starting from the initial guess of a flat potential, $\phi(x) = 0$ for all x .

2.2.3 Periodicity

The ion motion for $\alpha = 0$ and $\delta = 0$ is a periodic (closed) orbit provided that an effective potential minimum exists, $\bar{x} > \bar{x}_c(y)$, and that a pair of bounce points x_b and x_t exist, $U_\perp < \chi_M(y, \bar{x})$ (see Figure 21). For a closed orbit, the position x can be written as a function of a gyrophase angle which parameterizes the particular point of the orbit in which the particle lies. The period of the orbit, $2\pi/\bar{\Omega}$, where $\bar{\Omega}$ is the generalized gyrofrequency, is the integral of all the time elements $dt = dx/v_x$ over a whole orbit,

$$\frac{2\pi}{\bar{\Omega}} = 2 \int_{x_b}^{x_t} \frac{dx}{V_x(x, y, \bar{x}, U_\perp)}. \quad (2.40)$$

The gyrophase angle φ of the orbit is defined as $\bar{\Omega}t$, where t is defined in the interval $-\pi/\bar{\Omega} < t < \pi/\bar{\Omega}$ and is (when positive) the time elapsed since the particle last reached the top bounce point,

$$\varphi = \sigma_x \bar{\Omega} \int_{x_t}^x \frac{ds}{V_x(s, y, \bar{x}, U_\perp)}. \quad (2.41)$$

The time derivative of the gyrophase is the gyrofrequency,

$$\dot{\varphi} = \bar{\Omega}. \quad (2.42)$$

To obtain this, I have used $\partial\varphi/\partial x = \sigma_x \bar{\Omega}/V_x$ and $\sigma_x \dot{x} = V_x$ to simplify $\dot{\varphi} = \sigma_x \bar{\Omega} \dot{x} \partial\varphi/\partial x$. Note that inverting (2.41) gives $x(\varphi, y, \bar{x}, U_\perp)$. It will turn out that, for $\alpha \ll 1$, the ion distribution function is independent of φ .

It will be useful to define the gyroaveraging operation as a time average over possible values of gyrophase, or equivalently as an average over the period of a closed orbit,

$$\langle \dots \rangle_\varphi = \frac{1}{2\pi} \int_{-\pi}^{\pi} (\dots) d\varphi = \sum_{\sigma_x = \pm 1} \frac{\bar{\Omega}}{2\pi} \int_{x_b}^{x_t} \frac{(\dots) dx}{V_x(x, y, \bar{x}, U_\perp)}. \quad (2.43)$$

The second equality in (2.43) is obtained using (2.41). The closed orbit has an $\mathbf{E} \times \mathbf{B}$ drift in the y direction (parallel to the wall), with drift velocity $V_{\mathbf{E} \times \mathbf{B}}$ defined as the gyroaverage of v_y ,

$$V_{\mathbf{E} \times \mathbf{B}}(y, \bar{x}, U_{\perp}) = \frac{\bar{\Omega}}{\pi} \int_{x_b}^{x_t} \frac{\Omega(\bar{x} - x)}{V_x(x, y, \bar{x}, U_{\perp})} dx = \frac{\bar{\Omega}}{\pi} \int_{x_b}^{x_t} \frac{(1/B) \partial \phi(x, y) / \partial x}{V_x(x, y, \bar{x}, U_{\perp})} dx. \quad (2.44)$$

The second equality in (2.44) comes from using equation (2.36) and the result

$$\begin{aligned} \int_{x_b}^{x_t} \frac{\partial \chi(x; y, \bar{x}) / \partial x}{V_x(x, y, \bar{x}, U_{\perp})} dx &= - \int_{x_b}^{x_t} \frac{\partial V_x}{\partial x}(x, y, \bar{x}, U_{\perp}) dx \\ &= V_x(x_b, y, \bar{x}, U_{\perp}) - V_x(x_t, \bar{x}, U_{\perp}) = 0, \end{aligned} \quad (2.45)$$

where I used $V_x(x_b; y, \bar{x}, U_{\perp}) = V_x(x_t; y, \bar{x}, U_{\perp}) = 0$. The first equality in (2.45) comes from differentiating equation (2.31).

2.3 Magnetic presheath trajectories

The main effect of non-zero α and δ is to break the exact periodicity by making the orbit parameters vary over a characteristic time $1/\alpha\Omega \sim 1/\delta\Omega \gg 1/\Omega$. Using the results of Section 2.2, in Section 2.3.1 I explain how the ion trajectories consist of a sequence of approximately closed orbits. I quantify the variation of the orbit parameters to first order in α and δ , and obtain two quantities that are conserved to lowest order over the long timescale $1/\alpha\Omega \sim 1/\delta\Omega$: the adiabatic invariant and the z -component of the canonical momentum. A time $\sim 1/\Omega$ before the ion reaches the wall, the ion is considered to be in an “open” orbit. In Section 2.3.2, I define an open orbit and obtain the conditions that orbit parameters must satisfy for an ion to be in an open orbit.

2.3.1 Approximately closed orbits

When $\alpha = \delta = 0$ an ion moves in a closed orbit which $\mathbf{E} \times \mathbf{B}$ drifts in the y direction (equation (2.44)) and streams parallel to the magnetic field in the z direction (equation (2.34)). When $\alpha \sim \delta \ll 1$, the motion is *approximately* periodic because the orbit parameters vary over a timescale $1/\alpha\Omega$ that is much longer than the typical gyroperiod $1/\Omega$. The equations of motion (2.22)-(2.24) are approximately given by

$$\dot{v}_x = -\frac{\Omega}{B} \frac{\partial \phi}{\partial x} + \Omega v_y + O(\alpha^2 \Omega v_{t,i}), \quad (2.46)$$

$$\dot{v}_y = -\Omega v_x - \frac{\Omega}{B} \frac{\partial \phi}{\partial y} - \alpha \Omega v_z + O(\alpha^2 \Omega v_{t,i}), \quad (2.47)$$

$$\dot{v}_z = \alpha \Omega v_y + O(\alpha^2 \Omega v_{t,i}). \quad (2.48)$$

The time variation of the total energy is given by

$$\dot{U} = O(\delta^2 \Omega v_{t,i}^2) \quad (2.49)$$

because energy is exactly conserved up to explicit time dependence, which is second order in δ (equation (2.11)). Differentiating (2.28) with respect to time and using (2.47), we find

$$\dot{\bar{x}} = -\sigma_{\parallel} \alpha V_{\parallel}(U_{\perp}, U) - \frac{1}{B} \frac{\partial \phi}{\partial y}(x, y) + O(\alpha^2 v_{t,i}). \quad (2.50)$$

Physically, this drift is a combination of the small x -component of the parallel motion, and the small $\mathbf{E} \times \mathbf{B}$ drift due to the weak turbulent electric fields [14]. Differentiating (2.29) and using (2.46) and (2.47) we get

$$\dot{U}_{\perp} = -\sigma_{\parallel} \alpha \Omega^2 V_{\parallel}(U_{\perp}, U) (\bar{x} - x) + O(\alpha^2 \Omega v_{t,i}^2). \quad (2.51)$$

Both $\dot{\bar{x}}$ and \dot{U}_\perp depend on the instantaneous particle position x , and therefore on the gyrophase φ . Since the orbit parameters are varying over the long timescale t_{MPS} , they are approximately constant over a single orbit, and hence $\dot{\bar{x}}$ and \dot{U}_\perp are approximately periodic at small timescales (because x is approximately periodic). Hence, the gyroaveraged time derivatives of \bar{x} and U_\perp determine the behaviour of \bar{x} and U_\perp at long timescales. From (2.50) the gyroaveraged time derivative of \bar{x} is

$$\langle \dot{\bar{x}} \rangle_\varphi = -\sigma_\parallel \alpha V_\parallel (U_\perp, U) - \frac{1}{B} \left\langle \frac{\partial \phi}{\partial y}(x, y) \right\rangle_\varphi + O(\alpha^2 v_{\text{ti}}). \quad (2.52)$$

Exploiting (2.43) and (2.44), the gyroaverage of (2.51) is

$$\langle \dot{U}_\perp \rangle_\varphi = -\frac{\sigma_\parallel \alpha \Omega V_\parallel (U_\perp, U)}{B} \left\langle \frac{\partial \phi}{\partial x}(x, y) \right\rangle_\varphi + O(\alpha^2 \Omega v_{\text{ti}}^2). \quad (2.53)$$

Note that the overall motion in the y direction is determined by the gyroaveraged time derivative of y , which is the $\mathbf{E} \times \mathbf{B}$ drift of equation (2.44),

$$\langle \dot{y} \rangle_\varphi = \langle v_y \rangle_\varphi = \Omega \langle \bar{x} - x \rangle_\varphi = V_{\mathbf{E} \times \mathbf{B}}(y, \bar{x}, U_\perp) = \frac{1}{B} \left\langle \frac{\partial \phi}{\partial x}(x, y) \right\rangle_\varphi. \quad (2.54)$$

The variation of z is second order, $\dot{z}/z \sim \alpha^2 \Omega$. Two ion trajectories, which were obtained by varying the orbit parameters according to equations (2.49)-(2.51), are shown in Figure 24.

In a Hamiltonian system, when the parameters of periodic motion change over a timescale much longer than the period of the motion, an *adiabatic invariant* exists. Here, it is given by the definite integral

$$\mu = \frac{1}{\pi} \int_{x_b}^{x_t} V_x(x, y, \bar{x}, U_\perp) dx \sim \frac{v_{\text{ti}}^2}{\Omega}. \quad (2.55)$$

This is derived in Appendix D. Equation (2.55) is a generalization of the usual magnetic moment to the grazing angle presheath geometry which I study in this thesis. It was

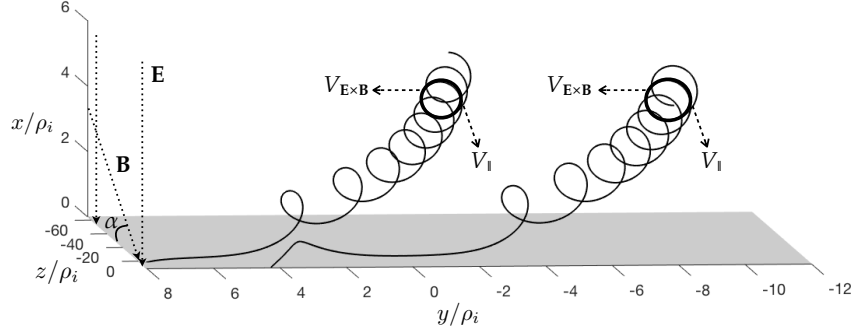


Figure 24: Two ion trajectories approaching the wall, represented as a grey surface at $x = 0$, are shown as black lines. The electric and magnetic fields are marked with dotted arrows. The angle between the magnetic field and wall is $\alpha = 0.05$ radians, although it looks large because the z direction has been squashed in order to draw the 3 dimensional ion trajectories. The electrostatic potential used to obtain the trajectories is the solution presented in chapter 4. Most of the ion motion is locally approximated by closed orbits, represented as superimposed rings. Ions stream along the magnetic field \mathbf{B} at velocity $V_{\parallel}(U_{\perp}, U)$, and the strong electric field towards the wall causes the approximately closed orbits to $\mathbf{E} \times \mathbf{B}$ drift at velocity $V_{\mathbf{E} \times \mathbf{B}}(y, \bar{x}, U_{\perp})$ in the y direction. The increasing electric field as the orbits approach $x = 0$ causes the $\mathbf{E} \times \mathbf{B}$ velocity to noticeably increase (see equation (2.44)). Since these are type II orbits, there is a point (x_M) in which the electric and magnetic forces on the ion are equal and opposite, where the trajectories spend a long time moving almost tangential to the wall. The trajectory on the left crosses x_M with near-zero v_x , while the trajectory on the right crosses x_M with the largest velocity possible. The two trajectories have, to lowest order, equal values of μ and U ; the only difference between them is the gyrophase φ .

derived by Cohen and Ryutov in reference [33]. Note that we can use μ as an orbit parameter instead of U_{\perp} . Unlike U_{\perp} , the adiabatic invariant (2.55) is conserved to lowest order over the much longer timescale t_{MPS} ,

$$\langle \dot{\mu} \rangle_{\varphi} = O(\alpha^2 v_{ti}^2) \simeq 0. \quad (2.56)$$

I proceed to prove equation (2.56). Differentiating (2.55) with respect to \bar{x} gives, using

$\partial\chi/\partial\bar{x} = \Omega^2 (\bar{x} - x)$ and equation (2.44),

$$\frac{\partial\mu}{\partial\bar{x}} = \frac{1}{\pi} \int_{x_b}^{x_t} \frac{\Omega^2 (x - \bar{x})}{\sqrt{2(U_\perp - \chi(x; y, \bar{x}))}} dx = -\frac{\Omega}{B\Omega} \left\langle \frac{\partial\phi}{\partial x}(x, y) \right\rangle_\varphi. \quad (2.57)$$

Differentiating (2.55) with respect to y , I obtain, using $\partial\chi/\partial y = (\Omega/B) \partial\phi/\partial y$,

$$\frac{\partial\mu}{\partial y} = -\frac{1}{\pi} \frac{\Omega}{B} \int_{x_b}^{x_t} \frac{\partial\phi/\partial y(x, y)}{\sqrt{2(U_\perp - \chi(x; y, \bar{x}))}} dx = -\frac{\Omega}{B\Omega} \left\langle \frac{\partial\phi}{\partial y}(x, y) \right\rangle_\varphi. \quad (2.58)$$

Finally, differentiating (2.55) with respect to U_\perp and using (2.40), I have

$$\frac{\partial\mu}{\partial U_\perp} = \frac{1}{\pi} \int_{x_b}^{x_t} \frac{1}{\sqrt{2(U_\perp - \chi(x; y, \bar{x}))}} dx = \frac{1}{\Omega}. \quad (2.59)$$

Using the chain rule to take the time derivative $\dot{\mu}$ gives, to first order in α and δ ,

$$\dot{\mu} = \frac{\partial\mu}{\partial\bar{x}} \dot{\bar{x}} + \frac{\partial\mu}{\partial y} \dot{y} + \frac{\partial\mu}{\partial U_\perp} \dot{U}_\perp. \quad (2.60)$$

Gyroaveraging equation (2.60), the first order gyroaveraged total derivative of the magnetic moment with respect to time is

$$\langle \dot{\mu} \rangle_\varphi = \frac{\partial\mu}{\partial\bar{x}} \langle \dot{\bar{x}} \rangle_\varphi + \frac{\partial\mu}{\partial y} \langle \dot{y} \rangle_\varphi + \frac{\partial\mu}{\partial U_\perp} \langle \dot{U}_\perp \rangle_\varphi. \quad (2.61)$$

Upon using (2.57)-(2.59) and (2.52)-(2.54), I obtain (2.56).

The variation of y with time is first order in my ordering, $\dot{y}/y \sim \alpha\Omega$. In what follows, I introduce another orbit parameter $y_\star \sim l$ which varies over a timescale much longer than t_{MPS} , $\dot{y}_\star/y_\star \sim \alpha^2\Omega \ll 1/t_{\text{MPS}}$. The equation of motion in the z direction is approximately (2.48). Integrating this in time and introducing the constant of integration y_\star gives

$$y_\star = y - \frac{v_z}{\alpha\Omega} \sim l. \quad (2.62)$$

This quantity is proportional to the canonical momentum in the z direction [34], if the magnetic vector potential is written so that it has no z dependence. Such a choice for

the vector potential is, for example,

$$\mathbf{A} = \begin{pmatrix} 0 \\ xB \cos \alpha \\ -yB \sin \alpha \end{pmatrix}. \quad (2.63)$$

This vector potential can be checked by calculating the magnetic field that corresponds to it,

$$\mathbf{B} = \nabla \times \mathbf{A} = \begin{pmatrix} -B \sin \alpha \\ 0 \\ B \cos \alpha \end{pmatrix}, \quad (2.64)$$

which is exactly the magnetic field present in the magnetic presheath. Using $\sin \alpha \simeq \alpha$, the canonical momentum in the z direction, p_z , is proportional to y_* , $p_z = m_i v_z + ZeA_z = m_i (v_z - \Omega y \sin \alpha) \simeq -m_i \alpha \Omega y_*$. Because the magnetic vector potential is written such that it is independent of z and the electrostatic potential depends on z only to second order (see equation (2.9)), the canonical momentum that we have just calculated is a constant of motion to first order, $\dot{p}_z/p_z \sim \alpha^2 \Omega$. Note that the orbit position \bar{x} is proportional to the canonical momentum in the y direction [56], $p_y = m_i v_y + ZeA_y = m_i (v_y + \Omega x \cos \alpha) \simeq m_i \Omega \bar{x}$. Because both the magnetic vector potential in (2.63) and the electrostatic potential have a first order dependence on y , we have $\dot{p}_y/p_y \sim \alpha \Omega$ as expected. Using (2.34) y_* is re-expressed in terms of y , U_\perp and U ,

$$y_* = y - \frac{1}{\alpha \Omega} v_\parallel (U_\perp, U, \sigma_\parallel). \quad (2.65)$$

The picture that emerges of the ion trajectory in a grazing angle magnetic presheath is that of a sequence of approximately closed orbits whose parallel streaming brings them slowly towards the wall, as shown in Figure 24. As the ion approaches the wall, its $\mathbf{E} \times \mathbf{B}$

drift increases. The adiabatic invariant μ , the z component of the canonical momentum y_* , and total energy U are conserved as the ion traverses the magnetic presheath. The final piece of the ion trajectory terminates at the wall, a characteristic that is clearly incompatible with periodicity. Hence, a time $1/\Omega$ before the ion reaches the wall, I consider the ion's trajectory to be an open orbit, as it can no longer be approximated by a closed orbit. The gyroaveraged time derivatives (equations (2.52)-(2.54)) are not an accurate description of the open orbit, and the instantaneous variation of the orbit parameters (equations (2.50)-(2.51)) must be considered in order to study open orbits.

2.3.2 Open orbits

When the ion reaches values of the orbit parameters for which its lowest order motion intersects the wall (and is therefore no longer periodic), it reaches the wall and is lost from the system over the fast timescale $1/\Omega$ (as I will show). In this short period of time, the ion is in an open orbit. The number of ions in open orbits is small (higher order in α) compared with the number of ions in closed orbits because open orbits exist for a much shorter time. However, the number of ions in closed orbits that cross a point arbitrarily close to the wall is small because it only includes those ions in type I orbits that are near the bottom bounce point of their orbit (and thus, from equation (2.41), it only includes ions with a small range of gyrophases around $\varphi = \pm\pi$). Therefore, it is essential to obtain the contribution to the density due to ions in open orbits.

It is clear that an ion is in an open orbit when $x \leq x_M$, because a closed orbit cannot access this region by definition (see Figure 21). For the ion to reach $x \leq x_M$, it must have crossed the maximum of the effective potential χ from the region $x > x_M$. The exact point $x > x_M$ at which we consider its orbit to be open is arbitrary, but this arbitrariness

does not matter because the ion density for $x > x_M$ is dominated by closed orbits. We exploit this to generalize the open orbit definition in a way that includes all ions at $x \leq x_M$ and smoothly extends the open orbit density to $x > x_M$. We consider an ion to be in an open orbit if:

$$\text{at future times, its trajectory has no bounce points;} \quad (2.66)$$

$$\text{at past times, its trajectory has several bounce points.} \quad (2.67)$$

Note that the criterion (2.67) corresponds to the past trajectory becoming an approximately closed orbit. Both criteria (2.66) and (2.67) rely on the wall being electron-repelling, because they assume that any ion reaching $x = 0$ (the Debye sheath entrance) does not bounce back. Examples of pieces of trajectories considered to be open orbits are shown in Figure 25 by solid lines. We consider open orbit the part of a trajectory between the wall and the top bounce point.

To study open orbits, it will be useful to consider the difference between the perpendicular energy and the effective potential maximum as a separate quantity D ,

$$D = U_{\perp} - \chi_M(y, \bar{x}). \quad (2.68)$$

The velocity component v_x , given by equation (2.31), is

$$v_x = \sigma_x V_x(x; y, \bar{x}, D + \chi_M(\bar{x})) = \sigma_x \sqrt{2(D + \chi_M(y, \bar{x}) - \chi(x; y, \bar{x}))}. \quad (2.69)$$

When $x = x_M$ is reached from $x > x_M$, the velocity is given by $v_x = -\sqrt{2D}$, hence only ions with $D > 0$ cross the effective potential maximum and reach $x \leq x_M$. To obtain the rate of change of D , we calculate the rate of change of $\chi_M(y, \bar{x})$,

$$\dot{\chi}_M(y, \bar{x}) = \frac{\partial \chi}{\partial \bar{x}}(x_M, y, \bar{x}) \dot{\bar{x}} + \frac{\partial \chi}{\partial x}(x_M; y, \bar{x}) \left(\frac{\partial x_M}{\partial \bar{x}} \dot{\bar{x}} + \frac{\partial x_M}{\partial y} \dot{y} \right) + \frac{\partial \chi}{\partial y}(x_M; y, \bar{x}) \dot{y}. \quad (2.70)$$

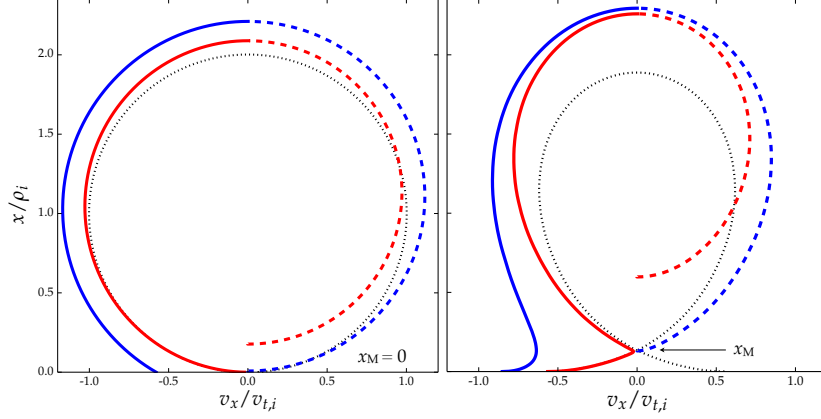


Figure 25: Two sets of phase space trajectories corresponding to type I (left diagram) and type II (right diagram) orbits. The type I trajectories are obtained using $\phi = 0$ everywhere, while the type II trajectories are evaluated using the electrostatic potential solution of chapter 4 for $\alpha = 0.02$, which has no y dependence. The dotted lines are trajectories of motion with $\alpha = 0$ when $U_{\perp} = \chi_M$, with $\bar{x} = \rho_i$ (type I) and $\bar{x} = 1.6\rho_i$ (type II). The solid and dashed lines are trajectories calculated by integrating equations (2.19), (2.31) and (2.50)-(2.51) backwards in time from $x = 0$ with $\alpha = 0.02$, starting with the same value of \bar{x} used to obtain the dotted trajectories and with $U - \chi_M = v_{t,i}^2$. The solid lines are the open orbit pieces of the trajectories, while the dashed lines are approximately closed orbits according to my definition. In each diagram, the red trajectory corresponds to the ion crossing x_M with $v_x \simeq 0$, while the blue trajectory corresponds to the ion crossing x_M with the largest possible value of $|v_x|$.

For both type I and type II orbits, the second term in (2.70) vanishes (type I curves have $\partial x_M / \partial \bar{x} = \partial x_M / \partial y = 0$, while type II curves have $\partial \chi / \partial x(x_M; y, \bar{x}) = 0$) and, using (2.33) and (2.50), we find

$$\begin{aligned} \dot{\chi}_M(\bar{x}) = & \sigma_{\parallel} \alpha \Omega^2 V_{\parallel}(U_{\perp}, U)(x_M - \bar{x}) + \frac{\Omega^2}{B}(x_M - \bar{x}) \frac{\partial \phi}{\partial y}(x, y) \\ & + \frac{\Omega^2}{B}(\bar{x} - x) \frac{\partial \phi}{\partial y}(x_M, y) + O(\alpha^2 \Omega v_{t,i}^2). \end{aligned} \quad (2.71)$$

Combining (2.71) with the result for \dot{U}_\perp in (2.51), we get

$$\begin{aligned} \dot{D}(x, y, \bar{x}, U_\perp, U) &= \sigma_\parallel \alpha \Omega^2 V_\parallel(U_\perp, U) (x - x_M) - \frac{\Omega^2}{B} (x_M - \bar{x}) \frac{\partial \phi}{\partial y}(x, y) \\ &+ \frac{\Omega^2}{B} (x - \bar{x}) \frac{\partial \phi}{\partial y}(x_M, y) + O(\alpha^2 \Omega v_{ti}^2). \end{aligned} \quad (2.72)$$

Consider an ion that reaches $U_\perp = \chi_M(y, \bar{x})$ at a position $x' > x_M$ and is travelling towards the maximum ($\sigma_x = -1$). We use the relation

$$dt = \frac{dx}{v_x} \simeq \frac{dx}{\sigma_x V_x(x; y, \bar{x}, U_\perp)} \quad (2.73)$$

to estimate the time taken for the ion to reach the effective potential maximum,

$$\delta t_M = \int dt \simeq \int_{x_M}^{x'} \frac{ds}{V_x(s; y, \bar{x}, U_\perp)}. \quad (2.74)$$

We assume that the difference between U_\perp and χ_M stays small and that the change in \bar{x} and y during the time δt_M is small (which we will show to be true), so that $U_\perp \simeq \chi_M(y, \bar{x})$. If the effective potential curve is of type I, $\delta t_M^I \sim 1/\Omega$, whereas for type II curves, δt_M^{II} diverges according to equation (2.74). We show this by expanding $V_x(x, y, \bar{x}, U_\perp)$ near $x \simeq x_M$ for a type II curve, using $U_\perp \simeq \chi_M$ and defining $\chi_M''(y, \bar{x}) \equiv \partial^2 \chi / \partial x^2(x_M, y, \bar{x})$ to obtain

$$V_x^{II}(x; y, \bar{x}, U_\perp) \simeq V_x^{II}(x, y, \bar{x}, \chi_M(y, \bar{x})) \simeq \sqrt{|\chi_M''|} |x - x_M|. \quad (2.75)$$

The time δt_M^{II} is then

$$\delta t_M^{II} \simeq \int_{x_M}^{x'} \frac{ds}{\sqrt{|\chi_M''|} (s - x_M)} \rightarrow \infty. \quad (2.76)$$

Despite this apparent divergence, the variation of D during the time δt_M can be evaluated using (2.73). Using $U_\perp \simeq \chi_M(y, \bar{x})$, equation (2.72) becomes

$$\begin{aligned} \dot{D}(x, y, \bar{x}, U_\perp, U) &= \alpha \Omega^2 V_\parallel(\chi_M(y, \bar{x}), U) (x - x_M) - \frac{\Omega^2}{B} (x_M - \bar{x}) \frac{\partial \phi}{\partial y}(x, y) \\ &+ \frac{\Omega^2}{B} (x - \bar{x}) \frac{\partial \phi}{\partial y}(x_M, y) + O(\alpha^2 \Omega v_{ti}^2). \end{aligned} \quad (2.77)$$

Note that $\dot{D} = 0$ at $x = x_M$. Thus, equations (2.75) and (2.77) imply that $\dot{D}/V_x(x, y, \bar{x}, \chi_M)$ is not divergent at $x = x_M$. Integrating equation (2.77) in time using (2.73), we have

$$D = \int \dot{D} dt \simeq \int_{x_M}^{x'} \frac{\dot{D}(s, y, \bar{x}, U_\perp, U)}{V_x(s, y, \bar{x}, \chi_M)} ds; \quad (2.78)$$

hence, we expect $D \sim \alpha v_{ti}^2 \sim \delta v_{ti}^2$ for both orbit types, justifying $U_\perp \simeq \chi_M(y, \bar{x})$ a posteriori. Using $U_\perp = \chi_M(y, \bar{x}) + D$ with $D \sim \alpha v_{ti}^2$, equation (2.74) can be used to obtain the more accurate estimate $\delta t_M^{\text{II}} \sim \ln(1/\alpha)/\Omega$. Putting together the estimates for both orbit types, I have

$$\Omega \delta t_M \sim \begin{cases} 1 & \text{for type I orbits,} \\ \ln\left(\frac{1}{\alpha}\right) & \text{for type II orbits.} \end{cases} \quad (2.79)$$

During the time δt_M , the change in \bar{x} and y is small.

I proceed to find the possible values of D which satisfy the open orbit criteria that I have defined. If $x < x_M$, the particle has already crossed the effective potential maximum and one has to integrate backwards in time to obtain the value of D at the moment x_M was crossed, denoted D_X , and further back to obtain the value of D during the last bounce from the bottom bounce point $x_b \simeq x_M$, denoted D_B . If $x > x_M$, one must integrate \dot{D} forwards in time to obtain D_X (because by definition the particle trajectory must cross x_M when it next reaches it, otherwise it would not be an open orbit), and backwards in time to obtain D_B .

I first obtain $D_X - D$ in terms of x , \bar{x} and U . If $x > x_M$, \dot{D} is integrated *forwards* in time (so $dt > 0$), and if $x < x_M$, \dot{D} is integrated *backwards* in time (so $dt < 0$). From equation (2.78), I obtain

$$D_X - D \simeq \Delta_+(x, y, \bar{x}, U) \equiv \int_{x_M}^x \frac{\dot{D}(s, y, \bar{x}, U_\perp, U)}{V_x(s, y, \bar{x}, \chi_M(\bar{x}))} ds \sim \alpha v_{ti}^2; \quad (2.80)$$

therefore, D_X is

$$D_X = D + \Delta_+(x, y, \bar{x}, U) + O(\alpha^{1+p} v_{ti}^2). \quad (2.81)$$

The power p used to quantify the error is given by

$$p = \begin{cases} 1 & \text{for type I orbits,} \\ \frac{1}{2} & \text{for type II orbits.} \end{cases} \quad (2.82)$$

The larger error from type II orbits comes from the fact that $D \sim \alpha v_{ti}^2$ is neglected when using $dt \simeq ds/V_x(s, y, \bar{x}, \chi_M(\bar{x}))$. Estimating $|v_x|$ more accurately in the region near the maximum, I have

$$V_x^{\text{II}}(x, y, \bar{x}, U_{\perp}) = V_x^{\text{II}}(x, y, \bar{x}, \chi_M(y, \bar{x}) + D) \simeq \sqrt{|\chi_M''|(x - x_M)^2 + 2D}. \quad (2.83)$$

Hence, there is a region of size $|x - x_M| \sim \alpha^{1/2} \rho_i$ where the estimate (2.75) is incorrect. The contribution from this region to the integral (2.80) is therefore incorrect, and the size of this contribution is the size of the error in equation (2.81). Indeed, multiplying the size of the region ($\int_{x_M}^x ds \sim \alpha^{1/2} \rho_i$) by the size of the integrand ($|x - x_M|/V_x^{\text{II}} \sim 1/\Omega$) and by the prefactor ($\alpha \Omega^2 v_{ti}^2$), I obtain an error of $\alpha^{3/2} v_{ti}^2$, in accordance with equation (2.81) with $p = 1/2$.

I proceed to obtain $D_B - D_X$ by integrating \dot{D} *backwards* in time (so $dt < 0$) from the point at which the maximum is crossed. The backwards integration is identical to the forwards one; hence, using equation (2.78), I obtain

$$D_X - D_B \simeq \Delta_M(y, \bar{x}, U) = 2 \int_{x_M}^{x_{tM}} \frac{\dot{D}(s, y, \bar{x}, \chi_M, U)}{V_x(x, y, \bar{x}, \chi_M(y, \bar{x}))} ds \sim 2\pi \alpha v_{ti}^2, \quad (2.84)$$

where x_{tM} is the top bounce point corresponding to $U_{\perp} = \chi_M(y, \bar{x})$. The factor of 2π in the final scaling of (2.84) is due to having integrated in time over a gyroperiod $\sim 2\pi/\Omega$.

Then, D_B is

$$D_B = D_X - \Delta_M(y, \bar{x}, U) + O(\alpha^{1+p} v_{ti}^2). \quad (2.85)$$

The criteria (2.66) and (2.67) used to determine whether an ion is in an open orbit can be used to obtain the possible values of D_B and D_X for an ion in an open orbit. We only consider $\sigma_x = -1$, as previously argued. Then, for an ion at position $x < x_M$, condition (2.66) is automatically satisfied as the ion's fate is to fall down the effective potential towards $x = 0$. However, condition (2.67) is satisfied provided the ion's past trajectory crosses the maximum x_M , so that $D_X > 0$, and then bounces back from the bottom bounce point (which, to lowest order, coincides with x_M) so that $D_B < 0$. For an ion at position $x > x_M$, condition (2.66) implies that $D_X > 0$ while condition (2.67) implies that $D_B < 0$. In both cases, imposing both conditions implies that both $D_X > 0$ and $D_B < 0$ must be satisfied. Note that the argument can be applied in the reverse direction as well, and hence conditions (2.66) and (2.67) are satisfied if and only if the following inequalities are satisfied:

$$D_X > O(\alpha^{1+p} v_{ti}^2); \quad (2.86)$$

$$D_B < O(\alpha^{1+p} v_{ti}^2). \quad (2.87)$$

The limited accuracy in the evaluation of D_X and D_B leads to the $O(\alpha^{1+p} v_{ti}^2)$ error in the inequality. Using conditions (2.86) and (2.87), and equations (2.81) and (2.85), the inequality

$$-\Delta_+(x, y, \bar{x}, U) + O(\alpha^{1+p} v_{ti}^2) < D < \Delta_M(y, \bar{x}, U) - \Delta_+(x, y, \bar{x}, U) + O(\alpha^{1+p} v_{ti}^2) \quad (2.88)$$

gives the values of D that an open orbit can have. From (2.88), for an open orbit to exist at some value of \bar{x} , U and y , the integral Δ_M must be positive. From equations (2.69) and

(2.88), there is a range of possible particle velocities v_x for open orbits, with maximum given by $-V_{x+}(x, \bar{x}, U)$, where

$$V_{x+}(x, \bar{x}, U) = \sqrt{2(-\Delta_+(x, y, \bar{x}, U) + \chi_M(y, \bar{x}) - \chi(x, y, \bar{x})) + O(\alpha^{1+p}v_{ti}^2)}, \quad (2.89)$$

and with range of values given by

$$\begin{aligned} \Delta v_x = & \sqrt{2(\Delta_M(y, \bar{x}, U) - \Delta_+(x, y, \bar{x}, U) + \chi_M(y, \bar{x}) - \chi(x, y, \bar{x})) + O(\alpha^{1+p}v_{ti}^2)} \\ & - \sqrt{2(-\Delta_+(x, y, \bar{x}, U) + \chi_M(y, \bar{x}) - \chi(x, y, \bar{x})) + O(\alpha^{1+p}v_{ti}^2)}, \end{aligned} \quad (2.90)$$

such that

$$-V_{x+}(x, y, \bar{x}, U) - \Delta v_x < v_x < -V_{x+}(x, y, \bar{x}, U). \quad (2.91)$$

Note that equations (2.89)-(2.91) are defined, for a given \bar{x} and U , in the region $0 \leq x \leq x_{t,M+}$, where $|x_{t,M} - x_{t,M+}| \sim \alpha\rho_i$ and $x_{t,M+}$ is obtained by setting $V_{x+}(x_{t,M+}, \bar{x}, U)$ to zero, $\chi_M(\bar{x}) - \chi(x_{t,M+}, \bar{x}) - \Delta_+(x_{t,M+}, \bar{x}, U) = 0$. In section 3.2.2 of chapter 3, I will obtain a useful approximation to equations (2.89)-(2.91) which eliminates the dependence on Δ_+ and is defined in the region $0 \leq x \leq x_{t,M}$ (instead of $0 \leq x \leq x_{t,M+}$).

CHAPTER 3

Ion distribution function and density

The magnetic presheath solution requires a treatment of the behaviour of a collection of ions in this system, which is the subject of this chapter. The ion distribution function $f(t, x, y, z, v_x, v_y, v_z)$ describes the probability of an ion having a certain position (x, y, z) and a certain velocity (v_x, v_y, v_z) at a time t , such that integrating the distribution function in velocity space at fixed time and position gives the number density n_i at that position and time,

$$n_i(t, x, y, z) = \int f(t, x, y, z, v_x, v_y, v_z) d^3v. \quad (3.1)$$

This chapter is devoted to obtaining f and n_i in the magnetic presheath, with the assumptions and approximations presented in chapter 2.

The structure of this chapter is as follows. First, in section 3.1, I obtain the ion distribution function by simplifying the kinetic equation using the asymptotic expansion $\alpha \sim \delta \ll 1$. Then, in section 3.2, I obtain the ion density by treating the contribution due to approximately closed orbits (described in subsection 2.3.1) and due to open orbits (described in subsection 2.3.2) separately.

3.1 Ion distribution function

The Vlasov equation, with an ion distribution function $f(t, x, y, z, v_x, v_y, v_z)$ is

$$\frac{\partial f}{\partial t} + \dot{x} \frac{\partial f}{\partial x} + \dot{y} \frac{\partial f}{\partial y} + \dot{z} \frac{\partial f}{\partial z} + \dot{v}_x \frac{\partial f}{\partial v_x} + \dot{v}_y \frac{\partial f}{\partial v_y} + \dot{v}_z \frac{\partial f}{\partial v_z} = 0. \quad (3.2)$$

In this paragraph, it will be useful to introduce vectors to represent the two possible sets of variables in which the kinetic equation can be written. By denoting $\mathbf{H} = (x, y, z, v_x, v_y, v_z)$, the kinetic equation is

$$\frac{\partial f}{\partial t} + \dot{\mathbf{H}} \cdot \frac{\partial f}{\partial \mathbf{H}} = 0. \quad (3.3)$$

Applying the change of variables $(x, y, z, v_x, v_y, v_z) \rightarrow (\varphi, y_\star, z, \bar{x}, \mu, U, \sigma_\parallel)$, the distribution function has the form $F(t, \varphi, y_\star, z, \bar{x}, \mu, U, \sigma_\parallel)$. By denoting $\mathbf{G} = (\varphi, y_\star, z, \bar{x}, \mu, U)$ and applying the chain rule on 3.3, the kinetic equation is re-expressed to

$$\frac{\partial F}{\partial t} + \left[\frac{\partial \mathbf{G}}{\partial t} + \dot{\mathbf{H}} \cdot \frac{\partial \mathbf{G}}{\partial \mathbf{H}} \right] \cdot \frac{\partial F}{\partial \mathbf{G}} = 0. \quad (3.4)$$

The expression in the square bracket is a vector, and can be identified as the time derivative of the set of variables \mathbf{G}

$$\dot{\mathbf{G}} = \frac{\partial \mathbf{G}}{\partial t} + \dot{\mathbf{H}} \cdot \frac{\partial \mathbf{G}}{\partial \mathbf{H}}. \quad (3.5)$$

Hence, the kinetic equation (3.2) is, when expressed in the set of variables \mathbf{G} ,

$$\frac{\partial F}{\partial t} + \dot{\varphi} \frac{\partial F}{\partial \varphi} + \dot{y}_\star \frac{\partial F}{\partial y_\star} + \dot{z} \frac{\partial F}{\partial z} + \dot{\bar{x}} \frac{\partial F}{\partial \bar{x}} + \dot{\mu} \frac{\partial F}{\partial \mu} + \dot{U} \frac{\partial F}{\partial U} = 0. \quad (3.6)$$

I expand the distribution function for $\alpha \sim \delta \ll 1$,

$$F = F_0 + F_1 + \dots, \quad (3.7)$$

where $F_0 \sim F$, $F_1 \sim \alpha F \sim \delta F$. Taking $O(\Omega F)$ terms only in (3.6) and using $\dot{\varphi} \simeq \bar{\Omega}$ (from equation (2.42)) leads to the lowest order equation

$$\bar{\Omega} \frac{\partial F_0}{\partial \varphi} = 0. \quad (3.8)$$

To obtain this, I used $\bar{\Omega} \sim \Omega$, $\dot{x}/\bar{x} \sim \dot{\mu}/\mu \sim \alpha\Omega$ and $\partial/\partial t \sim \dot{y}_*/y_* \sim \dot{z}/z \sim \dot{U}/U \sim \alpha^2\Omega$. From (3.8), the lowest order distribution function is gyrophase independent, $F_0 = F_0(t, y_*, z, \bar{x}, \mu, U)$.

The first order of (3.6) is

$$\dot{x} \frac{\partial F_0}{\partial \bar{x}} + \dot{\mu} \frac{\partial F_0}{\partial \mu} + \bar{\Omega} \frac{\partial F_1}{\partial \varphi} = 0. \quad (3.9)$$

where we used $\partial/\partial t \sim \dot{y}_*/y_* \sim \dot{z}/z \sim \dot{U}/U \sim \alpha^2\Omega$. Taking the gyroaverage of (3.9) and, using $\langle \dot{\mu} \rangle_\varphi / \mu \sim \alpha^2\Omega \sim \delta^2\Omega$ and $\langle \partial F_1 / \partial \varphi \rangle_\varphi = 0$, we obtain the gyrokinetic equation

$$\frac{\partial F_0}{\partial \bar{x}} = 0. \quad (3.10)$$

Therefore, the lowest order distribution function is independent of \bar{x} , $F_0 = F_0(t, y_*, z, \mu, U, \sigma_\parallel)$. Moreover, the dependence of the distribution function on z and t is unimportant, as argued in chapter 2. Hence, I do not consider z and t dependence in the ion distribution function, $F_0 = F_0(y_*, \mu, U, \sigma_\parallel)$.

Using that $F_0 = 0$ for $U_\perp \rightarrow \infty$ and $v_y = \Omega(\bar{x} - x) \sim \sqrt{U_\perp}$, the limit $\bar{x} \rightarrow \infty$ is equivalent to the limit $x \rightarrow \infty$. Hence, the distribution function at the magnetic presheath entrance is

$$\lim_{\bar{x} \rightarrow \infty} F_0 = \lim_{x \rightarrow \infty} F_0 = F_{\text{cl}}(y_*, \mu, U, \sigma_\parallel) \text{ for } \langle \dot{x} \rangle_\varphi < 0, \quad (3.11)$$

where the subscript “cl” stands for closed orbits. Note that the boundary condition only gives the particles that are drifting into the presheath, $\langle \dot{x} \rangle_\varphi < 0$. The assumption of an

electron repelling wall implies that no ion comes back from the wall. Thus, the only boundary condition to impose at $x = 0$ is that there be no forward moving ions. The distribution function of ions in the magnetic presheath is therefore

$$F \simeq F_0 = F_{\text{cl}}(y_*, \mu, U, \sigma_{\parallel}). \quad (3.12)$$

This result is similar to the one obtained in reference [33], but generalized using y_* in order to account for gradients parallel to the wall.

The ordering (1.1) implies that the collisional layer only determines the boundary conditions at $x \rightarrow \infty$. A solution of the collisional layer is thus required to obtain the correct form of F_{cl} . Alternatively, a drift-kinetic code of the scrape-off layer could be used to obtain such a distribution function.

3.2 Ion density

The total ion density is the sum of the closed orbit contribution, $n_{\text{i,cl}}(x, y)$, and the open orbit contribution, $n_{\text{i,op}}(x, y)$,

$$n_{\text{i}}(x, y) = n_{\text{i,cl}}(x, y) + n_{\text{i,op}}(x, y). \quad (3.13)$$

In subsection 3.2.1 an expression for $n_{\text{i,cl}}(x, y)$ is obtained, and in subsection 3.2.2 an expression for $n_{\text{i,op}}(x, y)$ is obtained.

3.2.1 Closed orbit density

In order to obtain the ion density of ions in approximately closed orbits, I first proceed to obtain the domain of phase space that allows for periodic solutions to lowest order in $\alpha \sim \delta \ll 1$. In references [33, 34, 56, 57], analytical expressions for the domain

of allowed closed orbits are found with various assumptions. My approach is similar to the one presented in reference [56], but includes the velocity dimension parallel to the magnetic field, weak gradients parallel to the wall, and allows for type II orbits. Type II orbits were not studied in reference [56] because the authors were studying the different problem of a plasma with a magnetic field exactly parallel to a wall, which is thus ion-repelling.

In this section, I sometimes denote the effective potential χ as a function of the variable s in order to distinguish the position x at which the ion density is evaluated from the positions s that a particle occupies in its lowest order orbit. Obviously x is just one of the many possible values that s can take. Electric fields outside the magnetic presheath are weak in our ordering, so that $\partial\phi/\partial s (s \rightarrow \infty, y) \simeq 0$. The effective potential χ must therefore be unbounded at infinity for finite \bar{x} ,

$$\frac{\partial\chi}{\partial s} (s \rightarrow \infty, \bar{x}, y) \simeq \Omega^2 (s - \bar{x}) > 0, \quad (3.14)$$

leading always to a bounce point for sufficiently large s . Therefore, in order to have a closed orbit crossing the position x at which we are calculating the integral, the effective potential must be larger than its value at x for some value of s between the particle position $s = x$ and the wall at $s = 0$,

$$\chi(s; y, \bar{x}) > \chi(x; y, \bar{x}) \text{ for some or all } s \in [0, x]. \quad (3.15)$$

Explicitly, this is (after dividing through by Ω^2)

$$\frac{1}{2} (s - \bar{x})^2 + \frac{\phi(s, y)}{\Omega B} > \frac{1}{2} (x - \bar{x})^2 + \frac{\phi(x, y)}{\Omega B}, \quad (3.16)$$

which reduces to

$$\bar{x} (x - s) > \frac{1}{2} (x^2 - s^2) + \frac{\phi(x, y) - \phi(s, y)}{\Omega B}. \quad (3.17)$$

This leads to the closed orbit condition

$$\bar{x} > g(s; x, y) \equiv \frac{1}{2}(x + s) + \frac{\phi(x, y) - \phi(s, y)}{\Omega B(x - s)} \text{ for some or all } s \in [0, x]. \quad (3.18)$$

The minimum value of \bar{x} , $\bar{x}_m(x, y)$, that satisfies this condition is obtained by minimizing the function $g(s; x, y)$ over the interval $[0, x]$,

$$\bar{x}_m(x, y) = \min_{s \in [0, x]} g(s, x, y). \quad (3.19)$$

Note that, from (3.18), $g(s; x, y) > x/2$ because $s < x$ and the electrostatic potential ϕ is increasing with the distance to the (negatively charged) wall. This implies that $\bar{x}_m(x, y) > x/2$. Figure 31 shows examples of type I and II effective potential curves with values of \bar{x} smaller than, equal to and larger than \bar{x}_m .

Closed orbits exist for $\bar{x} > \bar{x}_m(x, y)$. However, any orbit which has perpendicular energy $U_\perp > \chi_M(y, \bar{x})$ does not have a periodic solution to lowest order (with its trajectory intersecting the wall). Hence, the distribution function of approximately closed orbits is expected to be non-zero only for $\bar{x} > \bar{x}_m(x, y)$ and $U_\perp < \chi_M(y, \bar{x})$, and is therefore given by

$$f_{cl}(x, y, v_x, v_y, v_z) \simeq F_{cl}(y_\star, \mu, U, \sigma_\parallel) \Theta(\bar{x} - \bar{x}_m(x, y)) \Theta(\chi_M(y, \bar{x}) - U_\perp), \quad (3.20)$$

where Θ is the Heaviside step function,

$$\Theta(y) = \begin{cases} 1 & \text{for } y \geq 0, \\ 0 & \text{for } y < 0. \end{cases} \quad (3.21)$$

The density of ions crossing position (x, y) in approximately closed orbits is an integral in velocity space of the distribution function (3.20),

$$n_{i,cl}(x, y) = \int f_{cl}(x, y, \mathbf{v}) d^3v. \quad (3.22)$$

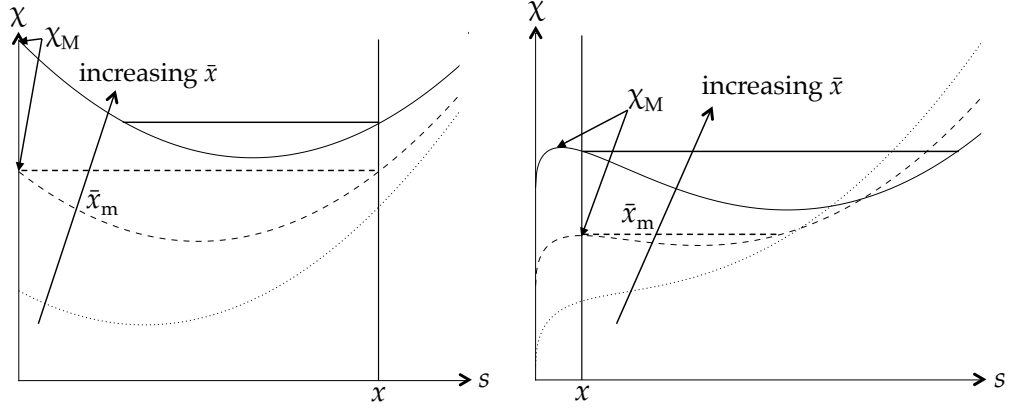


Figure 31: Two sets of effective potential curves, each set with three different curves $\chi(s, \bar{x}, y)$ plotted as a function of s that correspond to a different value of the orbit position \bar{x} . On the left, type I effective potential curves with a local maximum near the wall, which arises if the electric field is sufficiently strong there, are shown. On the right, type II effective potential curves without a maximum are shown. The solid curves are associated to orbits with position $\bar{x} > \bar{x}_m(x, y)$. Dashed curves correspond to orbit position $\bar{x}_m(x, y)$ which is associated with the presence of only one closed orbit that passes through x , while dotted ones correspond to orbits at position $\bar{x} < \bar{x}_m(x, y)$, which are all open if they are to cross point x . The horizontal lines are associated with the minimum perpendicular energy required for a closed orbit to lie at position \bar{x} and cross the point x , equal to $\chi(x, \bar{x}, y)$. The effective potential maximum $\chi_M(\bar{x}, y)$, marked for the closed (and semi-closed) orbit curves.

I proceed to change variables in the ion density integral (3.22) from (v_x, v_y, v_z) to (\bar{x}, U_\perp, U) while holding the ion position co-ordinates x and y fixed. Using (2.31), (2.33) and (2.34), the Jacobian is $|\partial(v_x, v_y, v_z)/\partial(\bar{x}, U_\perp, U)| = \Omega/|v_x v_z|$, which can be expressed as

$$\left| \frac{\partial(v_x, v_y, v_z)}{\partial(\bar{x}, U_\perp, U)} \right| = \frac{\Omega}{\sqrt{2(U_\perp - \chi(x; y, \bar{x}))} \sqrt{2(U - U_\perp)}}. \quad (3.23)$$

Therefore, the ion density integral becomes

$$n_{i,cl} = \sum_{\sigma_\parallel = \pm 1} \int_{\bar{x}_m(x, y)}^{\infty} d\bar{x} \int_{\chi(x; y, \bar{x})}^{\chi_M(y, \bar{x})} \frac{2\Omega dU_\perp}{\sqrt{2(U_\perp - \chi(x; y, \bar{x}))}} \int_{U_\perp}^{\infty} \frac{F_{cl}(y_\star, \mu, U, \sigma_\parallel)}{\sqrt{2(U - U_\perp)}} dU, \quad (3.24)$$

where the summation over the two possible values $\sigma_x = \pm 1$ has simplified to a factor of 2 because F_{cl} is independent of φ . If the distribution function were gyrophase dependent, the summation over σ_x would be necessary and (2.41) would be used in order to obtain $\varphi(x, y, \bar{x}, U_{\perp}, \sigma_x)$ at each integration point. The limits ensure that we integrate over the phase space domain in which closed orbits are allowed.

It is worth noting that $n_{\text{i,cl}}(0, y) = 0$, because for type I orbits $\chi_{\text{M}}(y, \bar{x}) = \chi(0, y, \bar{x})$ while for type II orbits $x = 0 < x_{\text{M}}$. The fact that $n_{\text{i,cl}}(0, y) = 0$ means that we cannot naively impose quasineutrality with only the approximately closed orbit contribution to the ion density. An attempt to impose $Zn_{\text{i,cl}}(0, y) = n_{\text{e}}(0, y)$ leads to $n_{\text{e}}(0, y) = n_{\text{e}\infty} \exp(e\phi(0, y)/T_{\text{e}}) = 0$ and therefore $\phi(0, y) = -\infty$. This is an unphysical result which stems from the fact that we have not kept the dominant contribution to the ion density at (and near) the wall, which comes from ions in open orbits. This contribution is calculated in the next section.

3.2.2 Open orbit density

Consider an ion at position (x, y) in an open orbit, when $U_{\perp} = \chi_{\text{M}}(y, \bar{x}) + D$ and D lies in the range (2.88). For such an ion to exist, the integral Δ_{M} defined in equation (2.84) *must* be positive. The ion transitioned from being in a closed orbit to being in an open orbit a time $\sim \delta t_{\text{M}}$ before the instant in time considered. At this time, the orbit position differed from \bar{x} by $O(\alpha\Omega\delta t_{\text{M}}\rho_{\text{i}})$, which is small. To lowest order, the ion conserved its adiabatic invariant up to the point where $U_{\perp} = \chi_{\text{M}}(y, \bar{x})$. Using $U_{\perp} \simeq \chi_{\text{M}}(y, \bar{x})$, the adiabatic invariant of the ion was $\mu(y, \bar{x}, \chi_{\text{M}}) + O(\alpha\Omega\delta t_{\text{M}}v_{\text{ti}}\rho_{\text{i}})$. Hence, the distribution function is $F_{\text{cl}}(y_{\star}(y, \chi_{\text{M}}, U, \sigma_{\parallel}), \mu(y, \bar{x}, \chi_{\text{M}}), U, \sigma_{\parallel})$ to lowest order, which is independent of the value of D [58, 59]. I proceed to obtain the values of \bar{x} (related

to v_y) and U (related to v_z) for which the distribution function is non-zero at fixed x and y . I also obtain the small range of values of v_x for which the open orbit distribution function is non-zero, at fixed values of x, y, \bar{x} and U .

For an ion in an open orbit to be at position x , the range of possible values of \bar{x} (to lowest order) is determined by two constraints. A time $\sim \delta t_M$ before being in an open orbit, the ion must have been in an approximately closed orbit whose existence depends on the presence of an effective potential minimum. Hence, a stationary point must exist, which implies that $\bar{x} > \bar{x}_c$ is necessary. Moreover, we require that $x < x_{t,M}$. For $x < x_c$, it is impossible for an ion to be in the region $x > x_{t,M}$ because $x_c \leq x_m \leq x_{t,M}$, therefore $\bar{x} > \bar{x}_c(y)$ is the necessary and sufficient condition for an open orbit crossing position x in this case. For $x > x_c$, we use the fact that $x_M < x_c$ to conclude that the ion must be in the region $x_M < x < x_{t,M}$; the criterion for an open orbit crossing position x is therefore identical to that of a closed orbit crossing position x , $\bar{x} > \bar{x}_m(x, y)$. Therefore, the condition for an ion in an open orbit to be present at position x is $\bar{x} > \bar{x}_{m,o}(x, y)$, where

$$\bar{x}_{m,o}(x, y) = \begin{cases} \bar{x}_c(y) & \text{for } x < x_c(y) \\ \bar{x}_m(x, y) & \text{for } x \geq x_c(y). \end{cases} \quad (3.25)$$

Two examples of how the constraint $\bar{x} > \bar{x}_{m,o}(x, y)$ arises are shown in Figure 32. This constraint is valid to lowest order in $\alpha\Omega\delta t_M$.

The ion's total energy has to be larger than the effective potential maximum, $U > \chi_M(y, \bar{x})$, and the z component of the velocity is approximated by $V_{\parallel}(\chi_M(\bar{x}), U)$. In order to relate values of v_y and v_z to lowest order values of \bar{x} and U for ions in open orbits, in what follows I refer extensively to equations (2.28) and

$$U = \chi_M(y, \bar{x}) + \frac{1}{2}v_z^2 + O(\alpha v_{t,i}^2), \quad (3.26)$$

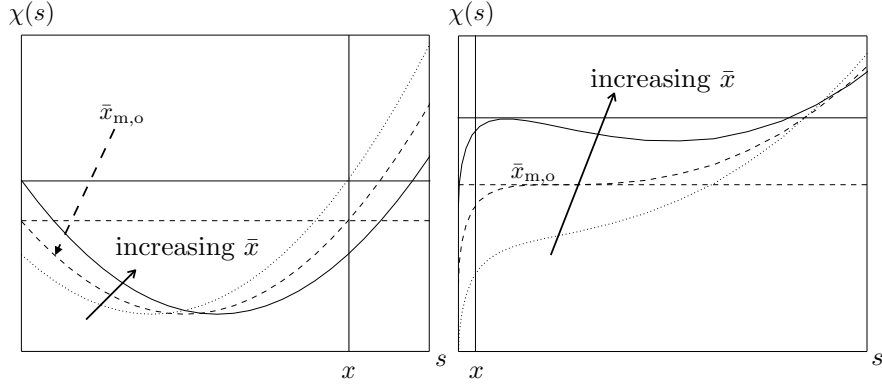


Figure 32: Type I and II effective potential curves are shown on the left and right respectively, for some fixed value of y (not shown). The dashed curves correspond to an orbit position $\bar{x} = \bar{x}_{m,o}(x, y)$, which is the minimum value of \bar{x} above which open orbits crossing the position x (vertical line) exist. The solid effective potential curves are the ones corresponding to $\bar{x} > \bar{x}_{m,o}(x)$. The horizontal lines correspond to $U_{\perp} = \chi_M$, which is the lowest order perpendicular energy of an ion in an open orbit. The dotted curves correspond to $\bar{x} < \bar{x}_{m,o}(x)$: no open orbits crossing position x exist for such values of \bar{x} because there are no closed orbits at $s \geq x$.

where the latter equation is obtained by rearranging the equation $v_z \simeq V_{\parallel}(\chi_M(y, \bar{x}), U)$.

The velocity component v_x lies in the range (2.91), which is obtained from the range of allowed values of D for given values of x, y, \bar{x} , and U . For the evaluation of the distribution function and density of ions in open orbits, the value of Δv_x is crucial because at a given x, \bar{x} and U it gives the *small* range of values of v_x in which the distribution function is non-zero. The *exact* value of the maximum and minimum v_x only needs to be known to lowest order. Hence, we can shift $V_{x+}(x, y, \bar{x}, U)$ by a small amount provided we preserve the same value of Δv_x . With this in mind, we proceed to obtain simpler expressions for $V_{x+}(x, y, \bar{x}, U)$ and Δv_x . Two regions must be distinguished: $|x - x_M| \sim \rho_i$ where $\chi_M - \chi \sim v_{ti}^2$, and $|x - x_M| \sim \alpha^p \rho_i$ where $\chi_M - \chi \sim \alpha v_{ti}^2$ (with p defined in equation (2.82)).

In the region $|x - x_M| \sim \rho_i$, we have

$$\alpha^{1+p} v_{ti}^2 \ll \Delta_M \sim \Delta_+ \sim \alpha v_{ti}^2 \ll \chi_M - \chi \sim v_{ti}^2. \quad (3.27)$$

By using equations (2.89) and (2.90), the ordering (3.27) leads to

$$\Delta v_x \sim \alpha v_{ti} \ll V_{x+} \sim v_{ti}. \quad (3.28)$$

Neglecting the term $\Delta_+ \sim \alpha v_{ti}^2$ in the square root of equation (2.89) for V_{x+} , we obtain

$$\begin{aligned} V_{x+}(x; \bar{x}, U) &= \sqrt{2(\chi_M(\bar{x}) - \chi(x, \bar{x})) + O(\alpha v_{ti}^2)} \\ &= V_x(x; \bar{x}, \chi_M(\bar{x})) + O(\alpha v_{ti}). \end{aligned} \quad (3.29)$$

I expand the terms Δ_M and Δ_+ out of the square root in equation (2.90) for Δv_x using the ordering (3.27), and thus obtain

$$\begin{aligned} \Delta v_x &= \left[\sqrt{2(\Delta_M(y, \bar{x}, U) - \Delta_+(x; y, \bar{x}, U) + \chi_M(y, \bar{x}) - \chi(x; y, \bar{x}) + O(\alpha^{1+p} v_{ti}^2))} \right. \\ &\quad \left. - \sqrt{2(-\Delta_+(x; y, \bar{x}, U) + \chi_M(y, \bar{x}) - \chi(x; y, \bar{x}) + O(\alpha^{1+p} v_{ti}^2))} \right] \\ &= \frac{\Delta_M(y, \bar{x}, U)}{\sqrt{2(\chi_M(y, \bar{x}) - \chi(x, y, \bar{x}))}} (1 + O(\alpha^p)). \end{aligned} \quad (3.30)$$

Note that the terms proportional to Δ_+ have cancelled to first order, and the error in the last line of (3.30) comes from the $O(\alpha^{1+p} v_{ti}^2)$ error in the evaluation of D (see equation (2.88)). For convenience, I re-express (3.30) in the form

$$\begin{aligned} \Delta v_x &= \left[\sqrt{2(\Delta_M(y, \bar{x}, U) + \chi_M(y, \bar{x}) - \chi(x, y, \bar{x}))} \right. \\ &\quad \left. - \sqrt{2(\chi_M(y, \bar{x}) - \chi(x, y, \bar{x}))} \right] (1 + O(\alpha^p)). \end{aligned} \quad (3.31)$$

I proceed to show that equations (3.29) and (3.31) are also valid in the region $|x - x_M| \sim \alpha^p \rho_i$. In this region, the scalings

$$\Delta_+ \lesssim \alpha^{1+p} v_{ti}^2 \ll \Delta_M \sim \chi_M - \chi \sim \alpha v_{ti}^2 \quad (3.32)$$

hold. From equations (2.89), (2.90) and (3.32) we have

$$\Delta v_x \sim V_{x+} \sim \alpha^{1/2} v_{ti}. \quad (3.33)$$

The term Δ_+ in the ordering (3.32) is small because the range of integration in equation (2.80) is small. Importantly, the $O(\alpha^{1+p} v_{ti}^2)$ error in the evaluation of D is larger than (or comparable to) Δ_+ . Hence, the term Δ_+ is negligible in equations (2.89) and (2.90), and equations (3.29) and (3.31) are valid in the region $|x - x_M| \sim \alpha^p \rho_i$.

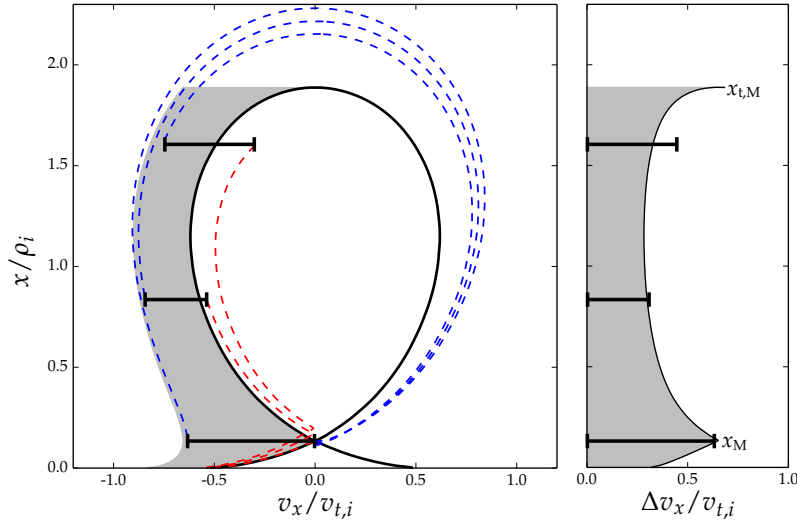


Figure 33: The left diagram shows ion trajectories (dashed lines) for $\alpha = 0.02$, obtained using equations (2.19), (2.31) and (2.50)-(2.51) with the numerical electrostatic potential solution presented in chapter 4 (with no y -dependence). At a given time, the trajectories have $\bar{x} = 1.6\rho_i$ and $U - \chi_M = v_{ti}^2$ at three different positions (marked with thick black lines). Blue lines are past ion trajectories chosen to have the largest value of U_\perp for which a bottom bounce point exists. Red lines are future ion trajectories chosen to have the smallest value of U_\perp for which the ion crosses the effective potential maximum x_M and reaches the wall. The thick black lines connect the red and blue trajectories at the three positions. Thus, they measure the difference between the maximum and minimum v_x of the open orbits. The shaded region on the left is $-V_x(x; \bar{x}, \chi_M) - \Delta v_x < v_x < -V_x(x, \bar{x}, \chi_M)$. On the right diagram, the difference between the maximum and minimum velocities of the open orbits at the three values of x is compared to the width of the shaded region, given by Δv_x .

In the above discussion I neglected the factor of 2π in the scaling $\Delta_M \sim 2\pi\alpha v_{ti}^2$ of equation (2.84). When this factor is included, equation (3.31) gives the scaling

$$2\pi\alpha v_{ti} \lesssim \Delta v_x \lesssim \sqrt{2\pi\alpha} v_{ti}, \quad (3.34)$$

where $\Delta v_x \sim \sqrt{2\pi\alpha} v_{ti}$ holds in the neighbourhood of the effective potential maximum x_M , while $\Delta v_x \sim 2\pi\alpha v_{ti}$ holds almost everywhere else. The behaviour of Δv_x as a function of x is shown in Figure 33. Note that there is a small region near the top bounce point that satisfies $|x - x_{tM}| \sim \alpha\rho_i$ in which $\Delta v_x \sim \sqrt{2\pi\alpha} v_{ti}$. In this region, equations (3.29) and (3.31) are not valid because $\Delta_+ \sim \Delta_M \sim \chi_M - \chi \sim \alpha v_{ti}^2$ and thus Δ_+ cannot be neglected. However, after equation (3.40) I will argue that the contribution to the ion density due to this region is small. Recall that Δv_x , calculated from equation (3.31), should be equal to the difference between the maximum and minimum velocity that an open orbit with a given y , \bar{x} and U can have. Indeed, from Figure 33 (which does not include y -dependence) we see that Δv_x is a good approximation to the range of allowed velocities at two out of three positions shown, and is a bad approximation only at the position close to x_{tM} .

The range of velocities in (2.91) reduces, using equations (3.29) and (3.31), to

$$-V_x(x, y, \bar{x}, \chi_M) - \Delta v_x < v_x < -V_x(x, y, \bar{x}, \chi_M). \quad (3.35)$$

Note the major simplification: equations (3.29) and (3.31), and therefore the range (3.35), are independent of Δ_+ . Equation (3.35) gives the range of values of v_x for which the distribution function of open orbits is non-zero. Using this range in v_x and $\bar{x} > \bar{x}_{m,o}(x, y)$, we have

$$\begin{aligned} f_{\text{op}}(x, y, v_x, v_y, v_z) &\simeq F_{\text{cl}}(y_*(y, V_{\parallel}), \mu(y, \bar{x}, \chi_M), U, \sigma_{\parallel}) \Theta(\bar{x} - \bar{x}_{m,o}(x, y)) \\ &\times \hat{\Pi}(v_x, -V_x(x, y, \bar{x}, \chi_M) - \Delta v_x, -V_x(x, y, \bar{x}, \chi_M)), \end{aligned} \quad (3.36)$$

where we defined the top-hat function $\hat{\Pi}(r, l_1, l_2)$ as

$$\hat{\Pi}(r, l_1, l_2) = \begin{cases} 1 & \text{if } l_1 \leq r < l_2, \\ 0 & \text{else.} \end{cases} \quad (3.37)$$

In equation (3.36) we can use (2.28) and (3.26) to re-express \bar{x} and U in terms of x , v_y and v_z . The subscript “op” stands for “open”.

The density of ions in open orbits is an integral of the distribution function in velocity space at fixed x , hence

$$n_{i,\text{op}}(x) = \int f_{\text{op}}(x, y, \mathbf{v}) d^3v. \quad (3.38)$$

Changing variables in the integral using equations (2.28) and (3.26) we get

$$n_{i,\text{op}}(x, y) = \int_{\bar{x}_{\text{m,o}}(x,y)}^{\infty} \Omega d\bar{x} \int_{\chi_{\text{M}}(y,\bar{x})}^{\infty} \frac{F_{\text{cl}}(y_*(y, v_z), \mu(y, \bar{x}, \chi_{\text{M}}), U, \sigma_{\parallel})}{\sqrt{2(U - \chi_{\text{M}})}} \Delta v_x dU. \quad (3.39)$$

The relative error in equation (3.39) is $O(\alpha^p)$.

From equations (3.34) and (3.39), the characteristic size of the open orbit density is

$$\alpha n_{e\infty} \lesssim n_{i,\text{op}} \lesssim \alpha^{1/2} n_{e\infty}. \quad (3.40)$$

The ordering $n_{i,\text{op}} \sim \alpha^{1/2} n_{e\infty}$ is valid for $x \lesssim \alpha \rho_i$ only if there is a sufficiently large number of type I orbits, that is, $\bar{x}_{\text{m,I}} \sim \rho_i$ (see Figure 23). Type I effective potential curves have $x_{\text{M}} = 0$ by definition, so all type I ion orbits must cross the effective potential maximum at the same position $x = 0$, with a range of values of v_x given by $\Delta v_x \sim \alpha^{1/2} v_{\text{ti}}$. For type II orbits, the open orbit density is always $n_{i,\text{op}} \sim \alpha n_{e\infty}$ because ions with different values of \bar{x} cross the effective potential maximum at different locations x_{M} . At some position x , there is a small range of values of x_{M} (and therefore of \bar{x}), given by $|x - x_{\text{M}}| \sim \alpha^{1/2} \rho_i$, in which $\Delta v_x \sim \alpha^{1/2} v_{\text{ti}}$. Multiplying the factor $\alpha^{1/2}$ from the

range of values of x_M by the factor $\alpha^{1/2}$ from the size of Δv_x gives a contribution of order $\alpha n_{e\infty}$ to the ion density from ions in the region $|x - x_M| \sim \alpha^{1/2} \rho_i$. Physically, the ions approach the wall more slowly near the effective potential maximum (where v_x is smaller), leading to a larger number of ions in this region due to flux conservation. However, ions in type II orbits slow down at different locations depending on their orbit position \bar{x} . Thus, there is not a *single* location where the ions in type II orbits accumulate. Therefore, their contribution to the density has the same characteristic size at all values of x . Conversely, ions in type I orbits are all slowly crossing the effective potential maximum at the same position $x = 0$, and therefore their contribution to the density at $x = 0$ is larger. Despite the fact that $\Delta v_x \sim \alpha^{1/2} v_{t,i}$ near $x_{t,M}$, the contribution to the density from ions in this region is of order $\alpha^{3/2} n_{e\infty}$ because the ions must be very close to $x_{t,M}$ for Δv_x to be large, that is, $|x - x_{t,M}| \sim \alpha \rho_i$. Consequently, the fact that Δv_x is a bad approximation to the range of values of v_x near $x_{t,M}$ (Figure 33) is unimportant.

CHAPTER 4

Electron-repelling magnetic presheath

The previous chapter provides the equations from which the ion distribution function and density can be obtained across the magnetic presheath if the electrostatic potential $\phi(x, y)$ is known. However, the electrostatic potential is not known a priori, but has to be determined from the quasineutrality equation. This chapter is devoted to solving the quasineutrality equation.

I assume a strongly electron-repelling wall and thus an adiabatic electron model. The conditions under which this assumption is justified are explained in section 4.1. Setting the ion and electron density equal to each other gives the quasineutrality equation, as shown in section 4.2. At the end of section 4.2, I take the limit $\delta \ll \alpha$ in the magnetic presheath, effectively setting $\delta = 0$ and thus ignoring turbulent gradients parallel to the wall for the remainder of this thesis. In section 4.3, I derive a condition that must be satisfied for the quasineutrality equation to have a steady-state solution. This condition is the kinetic generalization of the well-known Chodura condition (to lowest order in α). In section 4.4, I prove that the solution of my kinetic model satisfies the kinetic Bohm condition with the equality sign, and obtain the expected behaviour of the electrostatic

potential near $x = 0$. In section 4.5 I explain the numerical method and iteration procedure used to obtain the solution to the magnetic presheath quasineutrality equation. I conclude this chapter by presenting numerical results in section 4.6, discussing how the angle α affects the electrostatic potential and ion flow profiles, as well as the ion distribution function entering the Debye sheath.

4.1 Boltzmann electrons

Consider a magnetized plasma in contact with a wall without a potential difference between them and with a magnetic field making a small angle α with the wall. Ions and electrons are expected to travel at characteristic velocities equal to their thermal speeds. The ion thermal speed is defined in (2.3) and the electron thermal speed is

$$v_{t,e} = \sqrt{\frac{2T_e}{m_e}}. \quad (4.1)$$

A distance ρ_i from the wall, many ions reach the wall during their Larmor orbit. On the other hand, the typically much faster electrons ($v_{t,i} \ll v_{t,e}$) have to travel along the magnetic field because they are tied much more closely to the magnetic field lines than the ions ($\rho_e \ll \rho_i$), as shown in Figure 41. Hence, electrons travel a distance longer by a factor of $1/\alpha$ compared to ions, and they reach the wall in a time equal to $v_{t,i}/(\alpha v_{t,e})$ multiplied by the time taken by ions. The time taken by an electron to reach the wall is much smaller than the time taken by an ion if $v_{t,i}/(\alpha v_{t,e}) \ll 1$, which implies

$$\alpha \gg \sqrt{\frac{m_e T_i}{m_i T_e}}. \quad (4.2)$$

For $T_i \sim T_e$, we have $\alpha \gg \sqrt{m_e/m_i} \sim 0.02$ ($\simeq 1^\circ$) for Deuterium ions.

If the ordering (4.2) is satisfied, the plasma will lose a much larger number of electrons than ions and a potential difference that repels most of the electrons will be set

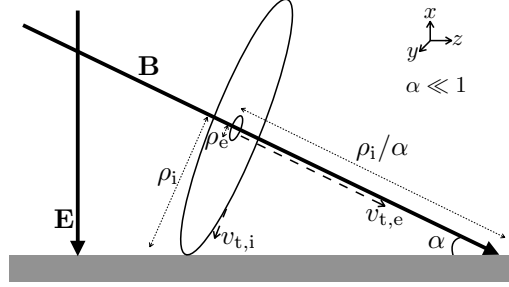


Figure 41: An ion (large) and electron (small) gyro-orbit are shown schematically an ion gyroradius ρ_i away from the wall (grey horizontal surface). The ion reaches the wall during a gyro-orbit, taking a time $\rho_i/v_{t,i}$, where $v_{t,i}$ is the ion thermal velocity. The electron gyroradius is much smaller, $\rho_e \ll \rho_i$. The electron reaches the wall by travelling a distance ρ_i/α parallel to the magnetic field at its thermal velocity $v_{t,e}$, taking a time $\rho_i/(\alpha v_{t,e}) = (v_{t,i}/(\alpha v_{t,e})) \times (\rho_i/v_{t,i})$. The x , y and z directions are shown relative to the magnetic and electric fields \mathbf{B} and \mathbf{E} , respectively.

up between the plasma and the wall. In current tokamaks, the angle α usually lies in the range $3^\circ - 11^\circ$ ($\alpha \sim 0.05 - 0.2$ in radians) and the ordering (4.2) is approximately satisfied. If (4.2) is not well satisfied, a kinetic electron model is necessary to solve for the magnetic presheath and Debye sheath. In ITER, it is expected that α will be around 2° (0.03 radians) [60]. Note that the presence of an electron current to the wall reduces the need for the wall to repel electrons, and thus large electron currents can increase the right hand side of 4.2. The electron-repelling assumption can therefore be violated at larger values of α than estimated above. Large electron currents are measured close to divertor or limiter targets in the near Scrape-Off-Layer [61]. This discussion highlights the need for a kinetic electron model in future studies of the sheath and presheath.

If (4.2) is satisfied (and there are no large electron currents to the wall), the electron density in the magnetic presheath is expected to be well-approximated by a Boltzmann distribution,

$$n_e(x, y) = n_{e\infty}(y) \exp\left(\frac{e(\phi(x, y) - \phi_\infty(y))}{T_e}\right). \quad (4.3)$$

In (4.3), $n_{e\infty}(y)$ and $\phi_\infty(y)$ are the electron density and the electrostatic potential at the magnetic presheath entrance ($x \rightarrow \infty$). The ordering (4.2) implies that the truncation of the Maxwellian electron distribution function, due to the high energy electrons reaching the wall instead of being reflected, can be ignored. Such truncation applies to the high-energy tail of the electron distribution function and leads to a negligible correction, of order $n_{e,\infty} \sqrt{m_e T_i / m_i T_e}$, to the Boltzmann distribution (4.3) [62].

4.2 Quasineutrality equation

The quasineutrality equation is

$$n_{e\infty}(y) \exp\left(\frac{e(\phi(x,y) - \phi_\infty(y))}{T_e}\right) = n_i(x,y). \quad (4.4)$$

The solution of this equation is the electrostatic potential $\phi(x,y)$ across a magnetic presheath with turbulent gradients. Solving the magnetic presheath numerically amounts to finding a potential for which (4.4) is satisfied. As previously proposed (without y dependence) by Cohen and Ryutov [33], one can solve the quasineutrality equation (4.4) by means of an iterative procedure. In order to solve for the self-consistent electrostatic potential in the magnetic presheath, the electrostatic potential profile at $x \rightarrow \infty$, $\phi_\infty(y)$, must be known as a boundary condition. This is $\phi_\infty(y) = \phi(x \rightarrow \infty, y)$. For some guessed potential $\phi(x,y)$, the integral on the right hand side of (4.4) can be computed numerically. If the initial guess can be corrected to a new guess such that the difference between the right hand side and the left hand side of (4.4) is reduced, this procedure can be iterated until convergence.

I implemented such an iteration procedure to solve the simpler problem with no gradients in the y direction ($\delta = 0$), as will be discussed in section 4.5. *I henceforth set*

$\delta = 0$ and thus neglect the y_* and y dependences from (4.4). The electron density is

$$n_e(x) = n_{e\infty} \exp\left(\frac{e\phi(x)}{T_e}\right), \quad (4.5)$$

where $n_{e\infty}$ is a constant and I set $\phi_\infty = 0$. The total ion density is

$$n_i(x) = n_{i,cl}(x) + n_{i,op}(x). \quad (4.6)$$

The ion distribution function simplifies to $F(\mu, U)$ and thus the closed orbit density is

$$n_{i,cl}(x) = \int_{\bar{x}_m(x)}^{\infty} d\bar{x} \int_{\chi(x;\bar{x})}^{\chi_M(\bar{x})} \frac{2\Omega dU_\perp}{\sqrt{2(U_\perp - \chi(x;\bar{x}))}} \int_{U_\perp}^{\infty} \frac{F_\infty(\mu, U)}{\sqrt{2(U - U_\perp)}} dU. \quad (4.7)$$

I have removed the summation over σ_\parallel because $\sigma_\parallel = +1$ is the only allowed value at $\bar{x} \rightarrow \infty$ when the turbulent $\mathbf{E} \times \mathbf{B}$ drift is not present (because $\dot{\bar{x}} = -\sigma_\parallel \alpha V_\parallel(U_\perp, U)$ must be negative at $x \rightarrow \infty$). The open orbit density is

$$n_{i,op}(x) = \int_{\bar{x}_{m,o}(x)}^{\infty} \Omega d\bar{x} \int_{\chi_M(\bar{x})}^{\infty} \frac{F_\infty(\mu(\bar{x}, \chi_M), U)}{\sqrt{2(U - \chi_M)}} \Delta v_x dU [1 + O(\alpha^p)]. \quad (4.8)$$

The quasineutrality equation thus becomes

$$n_{e\infty} \exp\left(\frac{e\phi(x)}{T_e}\right) = Z n_i(x). \quad (4.9)$$

Note that removing y dependence in equation (2.84) leads to

$$\Delta_M(\bar{x}, U) = \alpha V_\parallel(\chi_M(\bar{x}), U) I(\bar{x}), \quad (4.10)$$

where I defined the “open orbit integral”

$$I(\bar{x}, U) = 2\Omega^2 \int_{x_M}^{x_{t,M}} \frac{x - x_M}{V_x(x, \bar{x}, \chi_M(\bar{x}))} ds = 2\pi \frac{d}{d\bar{x}} (\mu(\bar{x}, \chi_M(\bar{x}))). \quad (4.11)$$

The last equality of (4.11) is proved as follows. Taking the total derivative of μ with respect to \bar{x} while fixing $U_\perp = \chi_M(\bar{x})$ gives

$$\frac{d}{d\bar{x}} (\mu(\bar{x}, \chi_M(\bar{x}))) = \frac{\partial \mu}{\partial U_\perp}(\bar{x}, \chi_M) \frac{d\chi_M}{d\bar{x}} + \frac{\partial \mu}{\partial \bar{x}}(\bar{x}, \chi_M). \quad (4.12)$$

Using equations (2.57) and (2.59) without y dependence, and using $\partial\chi_M/\partial\bar{x} = \Omega^2 (\bar{x} - x_M)$, one obtains

$$\frac{d}{d\bar{x}} (\mu(\bar{x}, \chi_M(\bar{x}))) = \frac{\Omega^2}{\pi} \int_{x_M}^{x_{t,M}} \frac{x - x_M}{V_x(x, \bar{x}, \chi_M)} dx. \quad (4.13)$$

Hence, the last equality of (4.11) follows.

Throughout this work I assume a single ion species. However, the quasineutrality equation can be generalized to include more than one ion species by adding the density integral of the additional species to equation (4.4) or its simplified version (4.9). Generalizing to a system with more than one ion species is needed to account for the presence of Deuterium and Tritium isotopes in roughly equal amounts near the divertor targets of future fusion devices.

4.3 Magnetic presheath entrance

Expanding the quasineutrality equation (4.9) near the magnetic presheath entrance $x \rightarrow \infty$ leads to:

- a solvability condition for the distribution function at the magnetic presheath entrance, with which I choose a realistic boundary condition for the ion distribution function at $x \rightarrow \infty$;
- the form of the electrostatic potential near $x \rightarrow \infty$, which is needed to determine the potential above a certain value of x in my numerical scheme.

At sufficiently large values of x , the electrostatic potential must be small, such that

$$\hat{\phi} = \frac{e |\phi(x)|}{T_e} \ll 1. \quad (4.14)$$

Here I also assume that the length scale of changes in the electrostatic potential is very large at sufficiently large x , such that

$$\epsilon = \frac{\rho_i \phi'(x)}{\phi(x)} \ll 1. \quad (4.15)$$

Assumption (4.15) is not the most general one, as ϵ can be of order unity, but it is useful because it is correct for the boundary condition at $x \rightarrow \infty$ chosen in Section 4.6. In general, $\hat{\phi} \lesssim \epsilon^2 \lesssim 1$, but here I take the more constrained limit

$$\hat{\phi} \lesssim \epsilon^2 \ll 1. \quad (4.16)$$

For $x \rightarrow \infty$, the open orbit density is higher order in α than the closed orbit density. Moreover, if the distribution function is exponentially decaying with energy, like the one I use in section 4.6, the open orbit density near $x \rightarrow \infty$ is exponentially small because only very large orbits with very large energies can extend all the way from the wall $x = 0$ to points with large x . Using that $n_{i,\text{open}}(x) \simeq 0$ for large x , the closed orbit density is obtained by expanding the near-circular ion orbits about circular orbits, as shown in Appendix E, to obtain

$$\begin{aligned} n_{i,\text{closed}}(x) = & \left(1 + \frac{\phi''(x)}{\Omega B}\right) \int_{-\pi}^{\pi} d\varphi \int_0^{\infty} \Omega d\mu \left\{ \int_{\Omega\mu}^{\infty} \frac{F_{\text{cl}}(\mu, U')}{\sqrt{2(U - \Omega\mu)}} dU \right. \\ & - \sqrt{2\delta U_{\perp}} F_{\text{cl}}(\mu, \Omega\mu) - \delta U_{\perp} \int_{\Omega\mu}^{\infty} \frac{\partial F_{\text{cl}}(\mu, U)/\partial U}{\sqrt{2(U - \Omega\mu)}} dU \\ & \left. + \frac{1}{3} (2\delta U_{\perp})^{3/2} \frac{\partial F_{\text{cl}}}{\partial U}(\mu, \Omega\mu) + \frac{1}{2} \delta U_{\perp}^2 \int_{\Omega\mu}^{\infty} \frac{\partial^2 F_{\text{cl}}(\mu, U)/\partial U^2}{\sqrt{2(U - \Omega\mu)}} dU \right\} \\ & + O\left(\hat{\phi}\epsilon^3 n_{e\infty}, \hat{\phi}^2 \epsilon^2 n_{e\infty}, \hat{\phi}^{5/2} n_{e\infty}\right), \end{aligned} \quad (4.17)$$

where

$$\begin{aligned} \delta U_{\perp} = & -\frac{\Omega\phi(x)}{B} + \frac{\Omega\phi'(x)}{B} \sqrt{\frac{2\mu}{\Omega}} \cos\varphi - \frac{\mu\phi''(x)}{2B} (1 + 2\cos^2\varphi) \\ & + O\left(\hat{\phi}\epsilon^3 v_{t,i}^2, \hat{\phi}^2 \epsilon^2 v_{t,i}^2\right). \end{aligned} \quad (4.18)$$

Note that equations (4.17) and (4.18) are derived to lowest order in $\alpha \ll 1$. The quantity δU_\perp is defined so that $U_\perp = \Omega\mu - \delta U_\perp$, and therefore captures the difference between U_\perp and $\Omega\mu$ as the ion travels into the magnetic presheath. Outside of the magnetic presheath, at $x \rightarrow \infty$, ion orbits are circular and $U_\perp = \Omega\mu$ (using $\phi(\infty) = \phi'(\infty) = \phi''(\infty) = 0$).

The electron density in (4.5) is expanded in $\hat{\phi} \ll 1$ for $x \rightarrow \infty$,

$$n_e(x) = n_{e\infty} + n_{e\infty} \frac{e\phi(x)}{T_e} + \frac{1}{2} n_{e\infty} \left(\frac{e\phi(x)}{T_e} \right)^2 + O(\hat{\phi}^3 n_{e\infty}). \quad (4.19)$$

Substituting (4.17) and (4.19) in (4.9), and using that $n_{i,op}(x) = 0$, I obtain the quasineutrality equation expanded in $\hat{\phi}$ and ϵ ,

$$\begin{aligned} n_{e\infty} + n_{e\infty} \frac{e\phi(x)}{T_e} + \frac{1}{2} n_{e\infty} \left(\frac{e\phi(x)}{T_e} \right)^2 &= Z \left(1 + \frac{\phi''(x)}{\Omega B} \right) \int_{-\pi}^{\pi} d\varphi \int_0^\infty \Omega d\mu \\ &\times \left\{ \int_{\Omega\mu}^\infty \frac{F_{cl}(\mu, U)}{\sqrt{2(U - \mu\Omega)}} dU - \sqrt{2\delta U_\perp} F_{cl}(\mu, \mu\Omega) - \delta U_\perp \int_{\Omega\mu}^\infty \frac{\partial F_{cl}(\mu, U)/\partial U}{\sqrt{2(U - \mu\Omega)}} dU \right. \\ &+ \frac{1}{3} (2\delta U_\perp)^{3/2} \frac{\partial F_{cl}}{\partial U}(\mu, \mu\Omega) + \frac{1}{2} \delta U_\perp^2 \int_{\Omega\mu}^\infty \frac{\partial^2 F_{cl}(\mu, U)/\partial U^2}{\sqrt{2(U - \mu\Omega)}} dU \left. \right\} \\ &+ O(\hat{\phi}\epsilon^3 n_{e\infty}, \hat{\phi}^2 \epsilon^2 n_{e\infty}, \hat{\phi}^{5/2} n_{e\infty}). \end{aligned} \quad (4.20)$$

To zeroth order in $\hat{\phi}$, equation (4.20) gives

$$Z \int_{-\pi}^{\pi} d\varphi \int_0^\infty \Omega d\mu \int_{\Omega\mu}^\infty \frac{F_{cl}(\mu, U)}{\sqrt{2(U - \Omega\mu)}} dU = n_{e\infty}. \quad (4.21)$$

This is the quasineutrality equation evaluated exactly at $x \rightarrow \infty$. The next order correction to (4.21) is a term of order $\hat{\phi}^{1/2}$, giving

$$-Z \int_{-\pi}^{\pi} d\varphi \int_0^\infty \Omega d\mu \sqrt{2\delta U_\perp} F_{cl}(\mu, \Omega\mu) = 0. \quad (4.22)$$

The distribution function $F_{cl}(\mu, U)$ is non-negative, and hence the integral in (4.22) is zero only if $F_{cl}(\mu, \Omega\mu) = 0$ for all possible values of μ . One expects this for an

electron-repelling sheath where no ions come back from the magnetic presheath, so $f_\infty(v_x, v_y, v_z) = 0$ at $v_z < 0$ and therefore $F_{cl}(\mu, \Omega\mu) = f_\infty(v_x, v_y, 0) = 0$.

To next order, $O(\hat{\phi})$, I collect all terms in (4.20) which are proportional to $\phi(x)$ or its derivatives. Integrating by parts¹ and using $F_{cl}(\mu, \Omega\mu) = 0$, I find the result

$$\int_{\mu\Omega}^{\infty} \frac{\partial F_{cl}(\mu, U)/\partial U}{\sqrt{2(U - \mu\Omega)}} dU = \int_{\mu\Omega}^{\infty} \frac{F_{cl}(\mu, U)}{(2(U - \mu\Omega))^{3/2}} dU. \quad (4.23)$$

With this result, the order $\hat{\phi}$ piece of (4.20) is, keeping terms up to $O(\hat{\phi}\epsilon^2)$,

$$\phi''(x) = k_1 \phi(x) + O(\hat{\phi}\epsilon^3), \quad (4.24)$$

where I define k_1 , a quantity with dimensions of $(1/\text{length})^2$, as

$$k_1 = \frac{\Omega^2 n_{e\infty} - 2\pi Z v_B^2 \int_0^\infty \Omega d\mu \int_{\mu\Omega}^\infty \frac{F_{cl}(\mu, U) dU}{(2(U - \mu\Omega))^{3/2}}}{v_B^2 n_{e\infty} + 2\pi Z \int_0^\infty \Omega^2 \mu d\mu \int_{\mu\Omega}^\infty \frac{F_{cl}(\mu, U) dU}{(2(U - \mu\Omega))^{3/2}}}. \quad (4.25)$$

From equation (4.24) and using the boundary condition $\phi = 0$ at $x \rightarrow \infty$, I find $\phi \propto \exp(-\sqrt{k_1}x)$. Consequently, $\sqrt{|k_1|}\rho_i \sim \epsilon$, and assumption (4.15) is true only if k_1 , defined in equation (4.25), is sufficiently small. If this is not the case, I expect $\phi \propto \exp(-\lambda x)$, but the value of λ would have to be determined by carrying out a more general expansion of the quasineutrality equation in $\hat{\phi} \ll 1$ with $\epsilon \sim 1$.

In order to impose that $\phi(\infty) = 0$, I require a non-oscillating potential profile at $x \rightarrow \infty$, which gives $k_1 \geq 0$ as a solvability condition. The numerator of k_1 determines the sign of k_1 because the denominator is always positive. Hence, I obtain the condition

$$2\pi Z v_B^2 \int_0^\infty \Omega d\mu \int_{\mu\Omega}^\infty \frac{F_{cl}(\mu, U) dU}{(2(U - \mu\Omega))^{3/2}} \leq n_{e\infty}, \quad (4.26)$$

¹Re-expressing integrals of the form on the left hand side of (4.23) to the form on the right hand side using integration by parts is common in the community. However, the form on the left hand side is more

where the Bohm velocity v_B is defined in equation (1.2). The equation

$$2\pi \int_0^\infty \Omega d\mu \int_{\mu\Omega}^\infty \frac{F_{cl}(\mu, U) h(\mu, U)}{\sqrt{2(U - \mu\Omega)}} dU = \int f_\infty(\mathbf{v}) h\left(\frac{v_x^2 + v_y^2}{2\Omega}, \frac{v_x^2 + v_y^2 + v_z^2}{2}\right) d^3v, \quad (4.27)$$

is valid for any function h and is obtained using the fact that $\mu = (v_x^2 + v_y^2)/2\Omega$ and $U = (v_x^2 + v_y^2 + v_z^2)/2$ at $x \rightarrow \infty$ (shown in Appendix E.1). I can use equation (4.27) to re-express the solvability condition as

$$Z v_B^2 \int \frac{f_\infty(\mathbf{v})}{v_z^2} d^3v \leq n_{e\infty}. \quad (4.28)$$

The solvability condition (4.28) generalizes Chodura's condition for the magnetic presheath entrance [15] to include the effect of kinetic ions at small α .² In chapter 5, I show that the cold ion limit of the generalized condition recovers the cold ion limit of Chodura's original condition to lowest order in α .

It is believed that solvability conditions such as (4.26) are usually satisfied marginally [31]. This means that equation (4.26) is expected to hold in the equality form, which justifies considering $k_1 = 0$ and hence justifies my initial assumption that $\epsilon \ll 1$. When $k_1 = 0$, terms of size $\hat{\phi}^{3/2}$ in the expansion of quasineutrality become important. From considering terms of this order in (4.20), I obtain

$$\phi''(x) = -k_{3/2} [-\phi(x)]^{3/2}, \quad (4.29)$$

where $k_{3/2}$ is given by

$$k_{3/2} = \sqrt{\frac{e}{T_e}} \left(\frac{\Omega}{v_B}\right)^2 \frac{\frac{2\sqrt{2}}{3} 2\pi \int_0^\infty \Omega v_B^3 \frac{\partial F_{cl}}{\partial U}(\mu, \Omega\mu) d\mu}{n_{e\infty} + 2\pi Z \int_0^\infty \Omega^2 \mu d\mu \int_{\Omega\mu}^\infty \frac{F_{cl}(\mu, U)}{(2(U - \Omega\mu))^{3/2}} dU} \geq 0. \quad (4.30)$$

general, as has been pointed out by Riemann in the context of the Debye sheath [31].

²It has been speculated that a kinetic generalization of Chodura's condition should be satisfied at

The numerator of (4.30) is positive because $F_{\text{cl}}(\mu, U) = 0$ for $U \leq \Omega\mu$ and hence $\partial F_{\text{cl}}(\mu, \Omega\mu)/\partial U \geq 0$ for all values of μ . Moreover, both terms in the denominator of (4.30) are explicitly positive, so the inequality in (4.30) follows. The case $k_{3/2} = 0$ only arises if $\partial F_{\text{cl}}(\mu, \Omega\mu)/\partial U = 0$ for all μ . Note that this condition implies $(1/v_z)\partial f_{\infty}(v_x, v_y, 0)/\partial v_z = 0$ for all values of v_x and v_y , which corresponds to a very flat ion distribution function near $v_z = 0$. One example of such a flat ion distribution function is the one used in section 5.3 of chapter 5.

Equation (4.29) is solved by multiplying by $\phi'(x)$ and then integrating once using the boundary condition $\phi'(x) = 0$ when $\phi(x) = 0$ to get

$$\phi'(x)^2 = \frac{4k_{3/2}}{5} [-\phi(x)]^{5/2}. \quad (4.31)$$

Taking the square root and integrating again, the potential profile is

$$\phi(x) = -\frac{400}{k_{3/2}^2} \frac{1}{(x + C_{3/2})^4}, \quad (4.32)$$

where $C_{3/2}$ is an integration constant. Equation (4.32) implies that $\epsilon \sim \hat{\phi}^{1/4} \gg \hat{\phi}$. The boundary condition that I use to obtain the numerical results (in Section 4.6) has $k_{3/2} \neq 0$, so equation (4.32) is the form of the electrostatic potential to which I must match my numerical solution at large x .

If $\partial F(\mu, \Omega\mu)/\partial U = 0$, then $k_{3/2} = 0$ and I must go to higher order in $\hat{\phi}$ to solve for the electrostatic potential at large x . For $\partial F_{\text{cl}}(\mu, \Omega\mu)/\partial U = 0$, one can integrate by parts twice the term with $\partial^2 F(\mu, \Omega\mu)/\partial U^2$ to get

$$\int_{\Omega\mu}^{\infty} \frac{\partial^2 F_{\text{cl}}(\mu, U)/\partial U^2}{\sqrt{2(U - \Omega\mu)}} dU = 3 \int_{\Omega\mu}^{\infty} \frac{F_{\text{cl}}(\mu, U)}{(2(U - \Omega\mu))^{5/2}} dU. \quad (4.33)$$

the magnetic presheath entrance [32]; however, the existing derivations [36, 63] make some simplifying assumptions.

Balancing the term of order $\hat{\phi}\epsilon^2$ with terms of order $\hat{\phi}^2$ in (4.20), I get

$$\phi''(x) = -k_2 [\phi(x)]^2, \quad (4.34)$$

where k_2 is given by

$$k_2 = \frac{\Omega^2 e}{2v_B^2 T_e} \frac{6\pi Z v_B^4 \int_0^\infty \Omega d\mu \int_{\Omega\mu}^\infty \frac{F_{cl}(\mu, U)}{(2(U - \Omega\mu))^{5/2}} dU - n_{e\infty}}{n_{e\infty} + 2\pi Z \int_0^\infty \Omega^2 \mu d\mu \int_{\Omega\mu}^\infty \frac{F_{cl}(\mu, U)}{(2(U - \Omega\mu))^{3/2}} dU} > 0. \quad (4.35)$$

Both terms in the denominator of (4.35) are positive, therefore the inequality on the right hand side of (4.35) is the result of the numerator being positive, which is demonstrated in Appendix F using the fact that (4.28) is satisfied with the equality sign. Equation (4.34) is solved in the same way as equation (4.29), and the result is

$$\phi(x) = -\frac{6}{k_2} \frac{1}{(x + C_2)^2}, \quad (4.36)$$

where C_2 is an integration constant. The fact that k_2 is positive and $k_2 \rho_i^2 T_e / e \sim 1$ implies that I do not need to carry out the expansion of (4.20) any further, because the order $\hat{\phi}^2$ term is guaranteed to be non-zero if the solvability condition (4.28) is marginally satisfied. Hence, $\epsilon \gtrsim \hat{\phi}^{1/2}$ as stated in equation (4.16).

4.4 Debye sheath entrance

By expanding the quasineutrality equation near the Debye sheath entrance, $x = 0$, I conclude that

- that the self-consistent solution of the system gives an ion distribution function at $x = 0$ that marginally satisfies the kinetic Bohm condition, with which I can check the numerically calculated distribution function;

- the self-consistent form of the potential near $x = 0$, with which I choose a suitable numerical discretization for the system.

I define the normalized electrostatic potential relative to $x = 0$,

$$\delta\hat{\phi} = \frac{e\delta\phi}{T_e} = \frac{e}{T_e} (\phi(x) - \phi(0)) \ll 1. \quad (4.37)$$

Each term of the quasineutrality equation (4.9) is expanded in $\delta\hat{\phi} \ll 1$ separately, order by order. Denoting the electron density at $x = 0$ as n_{e0} , such that

$$n_{e0} = n_{e\infty} \exp\left(\frac{e\phi(0)}{T_e}\right), \quad (4.38)$$

the electron density near $x = 0$ is

$$n_e(x) = n_{e0} \exp\left(\frac{e\delta\phi}{T_e}\right). \quad (4.39)$$

Using the result $n_{i,cl}(0) = 0$ and equation (4.9) gives

$$n_{e0} = Z n_{i,op}(0) = \int_{\bar{x}_{m,0}(0)}^{\infty} \Omega d\bar{x} \int_{\chi_M(\bar{x})}^{\infty} \frac{F_{cl}(\mu(\bar{x}, \chi_M), U)}{\sqrt{2(U - \chi_M(\bar{x}))}} \Delta v_{x0} dU, \quad (4.40)$$

where

$$\Delta v_{x0} = \Delta v_x|_{x=0} = \sqrt{2(\Delta_M(\bar{x}, U) + \chi_M(\bar{x}) - \chi(0, \bar{x}))} - \sqrt{2(\chi_M(\bar{x}) - \chi(0, \bar{x}))}. \quad (4.41)$$

Subtracting equation (4.40) from equation (4.9), I obtain the perturbed quasineutrality equation near $x = 0$,

$$n_e(x) - n_{e0} = Z (n_{i,cl}(x) + n_{i,op}(x) - n_{i,op}(0)). \quad (4.42)$$

The value of \bar{x} , $\bar{x}_{m,I}$, above which the orbits become type I becomes infinitely large in the magnetic presheath. Therefore, type I orbits are absent. To prove this result, I first

assume the more general scenario in which both type I and type II orbits are present, with $\phi'(0)$ being finite, and calculate the dominant contribution to equation (4.42).

I proceed to obtain the term $n_{i,cl}(x)$ in equation (4.42) to leading order. Firstly, I observe that a *closed* orbit near $x = 0$ must lie at a position x such that $0 \leq x_M \leq x$, with $\chi(x, \bar{x}) \simeq \chi_M(\bar{x})$. Remembering that for a closed orbit the perpendicular energy lies in the range $\chi(x, \bar{x}) \leq U_\perp \leq \chi_M(\bar{x})$, I can take the integral over U_\perp in (4.7) by approximating

$$F_{cl}(\mu(\bar{x}, U_\perp), U) \simeq F_{cl}(\mu(\bar{x}, \chi_M(\bar{x})), U) \quad (4.43)$$

and $\sqrt{2(U - U_\perp)} \simeq \sqrt{2(U - \chi_M(\bar{x}))}$. With these approximations, the integral (4.7) becomes

$$\begin{aligned} n_{i,cl}(x) &\simeq 2 \int_{\bar{x}_m(x)}^{\infty} \Omega \sqrt{2(\chi_M(\bar{x}) - \chi(x, \bar{x}))} d\bar{x} \\ &\quad \times \int_{\chi_M(\bar{x})}^{\infty} \frac{F_{cl}(\mu(\bar{x}, \chi_M(\bar{x})), U)}{\sqrt{2(U - \chi_M(\bar{x}))}} dU. \end{aligned} \quad (4.44)$$

The contributions to $n_{i,cl}(x)$ of type I and type II closed orbits have different sizes. Introducing the small quantity

$$\delta\chi = \chi(0, \bar{x}) - \chi(x, \bar{x}) \simeq -\frac{\Omega\delta\phi}{B} + \Omega^2\bar{x}x, \quad (4.45)$$

where I neglected the term proportional to x^2 , the closed orbit density (4.44) is dominated by type I closed orbits (which have $\chi_M(\bar{x}) = \chi(0, \bar{x})$), whose leading order density is given by

$$n_{i,cl}(x) \simeq 2 \int_{\bar{x}_{m,I}}^{\infty} \Omega \sqrt{2\delta\chi} d\bar{x} \int_{\chi_M}^{\infty} \frac{F_{cl}(\mu(\bar{x}, \chi_M(\bar{x})), U)}{\sqrt{2(U - \chi_M(\bar{x}))}} dU. \quad (4.46)$$

The reason for neglecting the contribution to the density of type II closed orbits is that the contribution from ions with $x_M > 0$ is smaller, as shown explicitly in Appendix G.

I now obtain $n_{i,\text{op}}(x) - n_{i,\text{op}}(0)$ to leading order. Using equations (4.8) and (3.25), the perturbed open orbit density is

$$\begin{aligned} n_{i,\text{op}}(x) - n_{i,\text{op}}(0) &\simeq \int_{\bar{x}_c}^{\infty} \Omega d\bar{x} \int_{\chi_M(\bar{x})}^{\infty} \frac{F_{\text{cl}}(\mu, U)}{\sqrt{2(U - \chi_M(\bar{x}))}} [\Delta v_x - \Delta v_{x0}] dU \\ &\quad - \int_{\bar{x}_c}^{\bar{x}_{\text{m.o}}(x)} \Omega d\bar{x} \int_{\chi_M(\bar{x})}^{\infty} \frac{F_{\text{cl}}(\mu, U)}{\sqrt{2(U - \chi_M(\bar{x}))}} \Delta v_{x0} dU \end{aligned} \quad (4.47)$$

where

$$\begin{aligned} \Delta v_x - \Delta v_{x0} &= \sqrt{2(\Delta_M(\bar{x}, U) + \chi_M(\bar{x}) - \chi(0, \bar{x}) + \delta\chi)} \\ &\quad - \sqrt{2(\chi_M(\bar{x}) - \chi(0, \bar{x}) + \delta\chi)} - \sqrt{2(\Delta_M(\bar{x}, U) + \chi_M(\bar{x}) - \chi(0, \bar{x}))} \\ &\quad + \sqrt{2(\chi_M(\bar{x}) - \chi(0, \bar{x}))}. \end{aligned} \quad (4.48)$$

The second term in (4.47) is zero if type II orbits are present ($x_c > 0$) because, from equation (3.25), $\bar{x}_{\text{m.o}}(x) = \bar{x}_c$ for $x < x_c \neq 0$. If no type II orbits are present ($x_c = 0$), equation (3.25) gives $\bar{x}_{\text{m.o}}(x) = \bar{x}_{\text{m}}(x)$ and, from equation (3.19), we expect the variation in $\bar{x}_{\text{m}}(x)$ to be linear in x and $\delta\phi$. For type I orbits, $\chi_M(\bar{x}) = \chi(0, \bar{x})$. Then, the second term in equation (4.48) is of order $\sqrt{\delta\hat{\phi}}$, the fourth term is zero, and the first and third terms together cancel to lowest order leaving a piece of order $\delta\hat{\phi}$. For $\chi_M(\bar{x}) > \chi(0, \bar{x})$, no term as large as $\sqrt{\delta\hat{\phi}}$ appears. Therefore, the dominant contribution to $\Delta v_x - \Delta v_{x0}$ is of order $\sqrt{\delta\hat{\phi}}$. Type II open orbits have $\chi_M(\bar{x}) \neq \chi(0, \bar{x})$, and hence they contribute at most an order $\delta\hat{\phi}$ piece to $\Delta v_x - \Delta v_{x0}$ ³. The minimum value of \bar{x} for which type I open orbits are present near $x = 0$ is approximately $\bar{x}_{\text{m,I}}$, giving

$$n_{i,\text{op}}(x) - n_{i,\text{op}}(0) \simeq - \int_{\bar{x}_{\text{m,I}}}^{\infty} \sqrt{2\delta\chi} \Omega d\bar{x} \int_{\chi_M(\bar{x})}^{\infty} \frac{F_{\text{cl}}(\mu(\bar{x}, \chi_M(\bar{x})), U)}{\sqrt{2(U - \chi_M(\bar{x}))}} dU. \quad (4.49)$$

³Some type II open orbits have $\chi_M(\bar{x}) - \chi(0, \bar{x}) \sim \delta\chi$, such that the second term in equation (4.48) is $\sqrt{\chi_M'' x_M^2 + 2\delta\chi} \sim \sqrt{\delta\hat{\phi} v_{\text{ti}}}$. The range of values of x_M for type II orbits which satisfy $\Delta v_x \sim \sqrt{\delta\hat{\phi} v_{\text{ti}}}$ is

From equation (4.39), one sees that there is no term in the expansion of the electron density that has a size $\sqrt{\delta\hat{\phi}}$. Hence, the dominant terms in the perturbed quasineutrality equation (4.42) for small x are obtained by adding equations (4.46) and (4.49) and setting the sum to zero,

$$0 = Z \int_{\bar{x}_{m,I}}^{\infty} \sqrt{2\delta\chi} \Omega d\bar{x} \int_{\chi_M(\bar{x})}^{\infty} \frac{F_{cl}(\mu(\bar{x}, \chi_M(\bar{x})), U)}{\sqrt{2(U - \chi_M(\bar{x}))}} dU. \quad (4.50)$$

The right hand side of equation (4.50) vanishes only if $\bar{x}_{m,I} \rightarrow \infty$, which from equation (2.37) implies a divergent electric field at $x = 0$, $\phi'(0) \rightarrow \infty$. The fact that $\bar{x}_{m,I} \rightarrow \infty$ means that only type II orbits are present in the magnetic presheath and $n_{i,cl}(x)$ is exponentially small, as argued in Appendix G. Therefore, I consider $n_{i,cl}(x) \simeq 0$ in equation (4.42) and focus on the perturbed open orbit density $n_{i,op}(x) - n_{i,op}(0)$.

With type I orbits absent, the effective potential maximum lies at $x_M \neq 0$, giving $\chi_M(\bar{x}) \neq \chi(0, \bar{x})$. Taking $\bar{x} \rightarrow \infty$ corresponds to $x_M \rightarrow 0$, leading to

$$\lim_{\bar{x} \rightarrow \infty} \chi_M(\bar{x}) = \chi(0, \bar{x}) \simeq \frac{1}{2} \Omega^2 \bar{x}^2. \quad (4.51)$$

If the distribution function F_{cl} decays exponentially at large energies, it is exponentially small in the region of the integral where $\chi_M(\bar{x}) - \chi(0, \bar{x}) \sim \delta\chi$ (which corresponds to \bar{x} being large). This is because, according to equation (4.51), $U_{\perp} \simeq \chi_M(\bar{x})$ is very large in that region. As a consequence, $\delta\chi \ll \chi_M(\bar{x}) - \chi(0, \bar{x})$ for values of \bar{x} where the distribution function is not exponentially small. When $\delta\chi \ll \chi_M(\bar{x}) - \chi(0, \bar{x})$, both terms in equation (4.48) can be Taylor expanded to obtain

$$\Delta v_x - \Delta v_{x0} = -\Delta \left[\frac{1}{v_{x0}} \right] \delta\chi + \frac{1}{2} \Delta \left[\frac{1}{v_{x0}^3} \right] \delta\chi^2, \quad (4.52)$$

small, $x_M \sim \sqrt{\delta\hat{\phi}\rho_i}$. Hence, integrating over such type II orbits results in a contribution to the density of the order of $\delta\hat{\phi}n_{e\infty}$.

where I introduced the positive quantities

$$\Delta \left[\frac{1}{v_{x0}} \right] = \frac{1}{\sqrt{2} (\chi_M(\bar{x}) - \chi(0, \bar{x}))} - \frac{1}{\sqrt{2} (\Delta_M(\bar{x}, U) + \chi_M(\bar{x}) - \chi(0, \bar{x}))}, \quad (4.53)$$

and

$$\Delta \left[\frac{1}{v_{x0}^3} \right] = \frac{1}{[2 (\chi_M(\bar{x}) - \chi(0, \bar{x}))]^{3/2}} - \frac{1}{[2 (\Delta_M(\bar{x}, U) + \chi_M(\bar{x}) - \chi(0, \bar{x}))]^{3/2}}. \quad (4.54)$$

I expand the open orbit density (4.8) using equation (4.52) for the expansion of Δv_x , obtaining

$$\begin{aligned} n_{i,op}(x) - n_{i,op}(0) \simeq & - \int_{\bar{x}_c}^{\infty} \delta\chi \Omega d\bar{x} \int_{\chi_M(\bar{x})}^{\infty} \frac{F_{cl}(\mu(\bar{x}, \chi_M), U)}{\sqrt{2} (U - \chi_M(\bar{x}))} \Delta \left[\frac{1}{v_{x0}} \right] dU \\ & + \frac{1}{2} \int_{\bar{x}_c}^{\infty} \delta\chi^2 \Omega d\bar{x} \int_{\chi_M(\bar{x})}^{\infty} \frac{F_{cl}(\mu(\bar{x}, \chi_M), U)}{\sqrt{2} (U - \chi_M(\bar{x}))} \Delta \left[\frac{1}{v_{x0}^3} \right] dU. \end{aligned} \quad (4.55)$$

Expanding the electron density (4.39), I get

$$n_e(x) - n_{e0} \simeq \frac{e\delta\phi}{T_e} + \frac{1}{2} \left(\frac{e\delta\phi}{T_e} \right)^2. \quad (4.56)$$

The perturbed quasineutrality equation (4.42), to order $\delta\hat{\phi}$, then implies that

$$\begin{aligned} n_{e0} \frac{e\delta\phi}{T_e} = & \frac{\Omega\delta\phi}{B} Z \int_{\bar{x}_c}^{\infty} \Omega d\bar{x} \int_{\chi_M(\bar{x})}^{\infty} \frac{F_{cl}(\mu(\bar{x}, \chi_M(\bar{x})), U)}{\sqrt{2} (U - \chi_M(\bar{x}))} \Delta \left[\frac{1}{v_x} \right] dU \\ & - x\Omega Z \int_{\bar{x}_c}^{\infty} \Omega^2 \bar{x} d\bar{x} \int_{\chi_M(\bar{x})}^{\infty} \frac{F_{cl}(\mu(\bar{x}, \chi_M(\bar{x})), U)}{\sqrt{2} (U - \chi_M(\bar{x}))} \Delta \left[\frac{1}{v_x} \right] dU. \end{aligned} \quad (4.57)$$

This can be rearranged to obtain

$$\delta\phi = \phi(x) - \phi(0) = \frac{x}{q_1}, \quad (4.58)$$

where q_1 is given by

$$q_1 = \frac{e}{\Omega T_e} \frac{Z v_B^2 \int_{\bar{x}_c}^{\infty} \Omega d\bar{x} \int_{\chi_M(\bar{x})}^{\infty} \frac{F_{cl}(\mu(\bar{x}, \chi_M(\bar{x})), U)}{\sqrt{2} (U - \chi_M(\bar{x}))} \Delta \left[\frac{1}{v_x} \right] dU - n_{e0}}{Z \int_{\bar{x}_c}^{\infty} \Omega^2 \bar{x} d\bar{x} \int_{\chi_M(\bar{x})}^{\infty} \frac{F_{cl}(\mu(\bar{x}, \chi_M(\bar{x})), U)}{\sqrt{2} (U - \chi_M(\bar{x}))} \Delta \left[\frac{1}{v_x} \right] dU}. \quad (4.59)$$

Equation (4.58) implies that $\phi'(0) = q_1^{-1}$. The magnetic presheath is *driven* towards $q_1 = 0$ because $\phi'(0) \rightarrow \infty$ is required from equation (4.50) and the discussion following it. Hence, the numerator of q_1 must be zero,

$$Z v_B^2 \int_{\bar{x}_c}^{\infty} \Omega d\bar{x} \int_{\chi_M(\bar{x})}^{\infty} \frac{F_{cl}(\mu(\bar{x}, \chi_M), U)}{\sqrt{2(U - \chi_M)}} \Delta \left[\frac{1}{v_{x0}} \right] dU = n_{e0}. \quad (4.60)$$

I proceed to show that equation (4.60) is equivalent to the marginal form of the kinetic Bohm condition [30, 31, 64],

$$Z v_B^2 \int \frac{f_0(\mathbf{v})}{v_x^2} d^3v = n_{e0}. \quad (4.61)$$

From (3.36), the distribution function at $x = 0$ is

$$\begin{aligned} f_0(\mathbf{v}) &= f_{\text{open}}(0, \mathbf{v}) \\ &\simeq F_{cl}(\mu(\bar{x}, \chi_M(\bar{x})), U) \hat{\Pi}(v_x, -V_x(0, \bar{x}, \chi_M) - \Delta v_{x0}, -V_x(0, \bar{x}, \chi_M)). \end{aligned} \quad (4.62)$$

Using the definition (4.62) and the change of variables $(\bar{x}, U) \rightarrow (v_y, v_z)$ (equations (2.28) and (3.26)) at $x = 0$, I can re-express the integral in (4.60) to obtain

$$\begin{aligned} &\int_{\bar{x}_c}^{\infty} \Omega d\bar{x} \int_{\chi_M(\bar{x})}^{\infty} \frac{F_{cl}(\mu(\bar{x}, \chi_M(\bar{x})), U)}{\sqrt{2(U - \chi_M(\bar{x}))}} \Delta \left[\frac{1}{v_{x0}} \right] dU \\ &= \int_{\bar{x}_c}^{\infty} \Omega d\bar{x} \int_{\chi_M(\bar{x})}^{\infty} \frac{F_{cl}(\mu(\bar{x}, \chi_M(\bar{x})), U)}{\sqrt{2(U - \chi_M(\bar{x}))}} dU \\ &\quad \times \int_{-\infty}^0 \frac{1}{v_x^2} \hat{\Pi}(v_x, -V_x(0, \bar{x}, \chi_M) - \Delta v_{x0}, -V_x(0, \bar{x}, \chi_M)) dv_x \\ &= \int \frac{f_0(\mathbf{v})}{v_x^2} d^3v. \end{aligned} \quad (4.63)$$

This shows that equations (4.60) and (4.61) are equivalent. Hence, the system is driven to marginally satisfying the kinetic Bohm condition (4.61).

Because $q_1 = 0$, I must consider terms of size $\sim \delta \hat{\phi}^2$ in equation (4.42). Using equa-

tions (4.55) and (4.56), I obtain

$$\frac{1}{2}n_{e0} \left(\frac{e\delta\phi}{T_e} \right)^2 = -Zx \int_{\bar{x}_c}^{\infty} \Omega^3 \bar{x} d\bar{x} \int_{\chi_M(\bar{x})}^{\infty} \frac{F_{cl}(\mu(\bar{x}, \chi_M(\bar{x})), U)}{\sqrt{2(U - \chi_M(\bar{x}))}} \Delta \left[\frac{1}{v_x} \right] dU \quad (4.64)$$

$$+ \frac{Z\Omega^2 \delta\phi^2}{2B^2} \int_{\bar{x}_c}^{\infty} \Omega d\bar{x} \int_{\chi_M(\bar{x})}^{\infty} \frac{F_{cl}(\mu(\bar{x}, \chi_M(\bar{x})), U)}{\sqrt{2(U - \chi_M(\bar{x}))}} \Delta \left[\frac{1}{v_x^3} \right] dU. \quad (4.65)$$

This leads to

$$\delta\phi = \phi(x) - \phi(0) = q_2^{-1/2} x^{1/2}, \quad (4.66)$$

where

$$q_2 = \frac{1}{2} \left(\frac{e}{T_e} \right)^2 \frac{Zv_B^4 \int_{\bar{x}_c}^{\infty} \Omega d\bar{x} \int_{\chi_M(\bar{x})}^{\infty} \frac{F_{cl}(\mu(\bar{x}, \chi_M(\bar{x})), U)}{\sqrt{2(U - \chi_M(\bar{x}))}} dU \Delta \left[\frac{1}{v_x^3} \right] - n_{e0}}{Z \int_{\bar{x}_c}^{\infty} \Omega^3 \bar{x} d\bar{x} \int_{\chi_M(\bar{x})}^{\infty} \frac{F_{cl}(\mu(\bar{x}, \chi_M(\bar{x})), U)}{\sqrt{2(U - \chi_M(\bar{x}))}} \Delta \left[\frac{1}{v_x} \right] dU} > 0. \quad (4.67)$$

In Appendix F, I show that q_2 is always positive and never small because equation (4.61) is satisfied. Therefore, equation (4.66) is the scaling of the electrostatic potential I expect to observe in my numerical results.

4.5 Numerical method

I discretize the potential on a grid x_η (labelled by the index η)

$$\frac{x_\eta}{\rho_i} = \begin{cases} (0.05\eta)^2 & \text{for } 0 \leq \eta < 10, \\ 0.25 + 0.1(\eta - 10) & \text{for } 10 \leq \eta < \eta_2 = 129. \end{cases} \quad (4.68)$$

I numerically calculate the ion density profile $n_i(x_\eta)$ in the region $0 \leq x_\eta \leq x_{\eta_1} = 6.15\rho_i$ ($\eta_1 = 69$). The domain in x is larger than $[0, x_{\eta_1}]$ because the potential profile in the region $x_{\eta_1} < x \leq x_{\eta_2} = 12.15\rho_i$ is necessary to correctly evaluate the ion density at x_{η_1} and in its neighbourhood. The electron density profile $n_e(x_\eta)$ is evaluated

by inserting $\phi(x_\eta)$ into equation (4.5). I iterate over electrostatic potential functions $\phi_\nu(x_\eta)$, where ν is an index labelling the iteration number. The problem of solving (4.9) is equivalent to finding, after N iterations, a $\phi_N(x_\eta)$ for which $n_{e,N}(x_\eta) \simeq n_{i,N}(x_\eta)$ in the region $0 \leq x \leq x_{\eta_1}$.

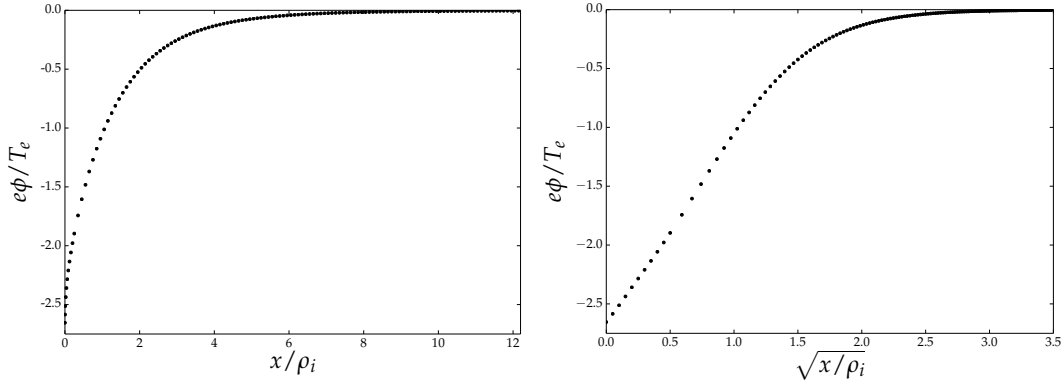


Figure 42: An example solution for the electrostatic potential profile (for $\alpha = 0.05$) is plotted on the grid of equation (4.68). Initially ϕ increases linearly with \sqrt{x} , which justifies my grid choice.

Near $x = 0$, the grid (4.68) that I use to discretize all functions of x has evenly spaced values of $\sqrt{x/\rho_i}$ ranging from 0 to 0.5 in intervals of 0.05. The reason for this is that the self-consistent solution of the electrostatic potential is expected to be proportional to \sqrt{x} near $x = 0$, as in equation (4.66). This behaviour of the electrostatic potential is captured by my grid as shown in Figure 42. For $\sqrt{x/\rho_i} > 0.5$, corresponding to $x/\rho_i > 0.25$, my grid has evenly spaced values of x/ρ_i , ranging from 0.25 to 12.15 in intervals of 0.1.

The density integrals in equations (4.7) and (4.8) are evaluated numerically at every point x_η by employing the trapezoidal rule. In order to evaluate those integrals, I first evaluate the integrands. I introduce a grid of positions \bar{x}_γ (labelled with the index γ),

$$\frac{\bar{x}_\gamma}{\rho_i} = 0.01\gamma \text{ for } 0 \leq \gamma < 1200. \quad (4.69)$$

Then, I evaluate the function $\chi(x_\eta, \bar{x}_\gamma)$ at all possible values of x_η and \bar{x}_γ . I find the location of the effective potential maximum x_M corresponding to the index $\eta_M(\gamma)$ that satisfies either

$$\chi(x_{\eta_M(\gamma)}, \bar{x}_\gamma) > \chi(x_{\eta_M(\gamma)+1}, \bar{x}_\gamma) \text{ for } \eta_M(\gamma) = 0 \text{ (type I)} \quad (4.70)$$

or

$$\begin{aligned} &\chi(x_{\eta_M(\gamma)}, \bar{x}_\gamma) > \chi(x_{\eta_M(\gamma)-1}, \bar{x}_\gamma) \\ &\text{and } \chi(x_{\eta_M(\gamma)}, \bar{x}_\gamma) > \chi(x_{\eta_M(\gamma)+1}, \bar{x}_\gamma) \text{ for } \eta_M(\gamma) \geq 1 \text{ (type II).} \end{aligned} \quad (4.71)$$

I also find the location of the effective potential minimum x_m corresponding to the index $\eta_m(\gamma)$ that satisfies

$$\begin{aligned} &\chi(x_{\eta_m(\gamma)}, \bar{x}_\gamma) < \chi(x_{\eta_m(\gamma)-1}, \bar{x}_\gamma) \\ &\text{and } \chi(x_{\eta_m(\gamma)}, \bar{x}_\gamma) < \chi(x_{\eta_m(\gamma)+1}, \bar{x}_\gamma) \text{ for } \eta_m(\gamma) \geq 1. \end{aligned} \quad (4.72)$$

At every value of the orbit parameter \bar{x}_γ , I obtain a grid of possible values of perpendicular energy $U_{\perp, \gamma \kappa}$, indexed with γ and κ ,

$$U_{\perp, \gamma \kappa} = \chi(x_{\kappa + \eta_M(\gamma)}, \bar{x}_\gamma) \text{ for } 0 \leq \kappa \leq \eta_m(\gamma) - \eta_M(\gamma). \quad (4.73)$$

This grid is shown in Figure 43. For all possible \bar{x}_γ and $U_{\perp, \gamma \kappa}$, I evaluate the adiabatic invariant $\mu(\bar{x}_\gamma, U_{\perp, \gamma \kappa})$ by performing the integral (2.55) using the trapezoidal rule. Similarly, for all possible values of \bar{x}_γ , I evaluate the integral $I(\bar{x}_\gamma)$ in (4.11) using the trapezoidal rule⁴. For all values of γ and κ , the total energy is labelled by the index ι ,

$$\frac{2U_{\gamma \kappa \iota}}{v_{t,i}^2} = \frac{2U_{\perp, \gamma \kappa}}{v_{t,i}^2} + (0.2\iota)^2 \text{ for } 0 \leq \iota < \iota_{\max}, \quad (4.74)$$

⁴Taking the derivative of $\mu(\bar{x}_\gamma, \chi_M(\bar{x}_\gamma))$, as in the last equality of (4.11), is faster and gives the same

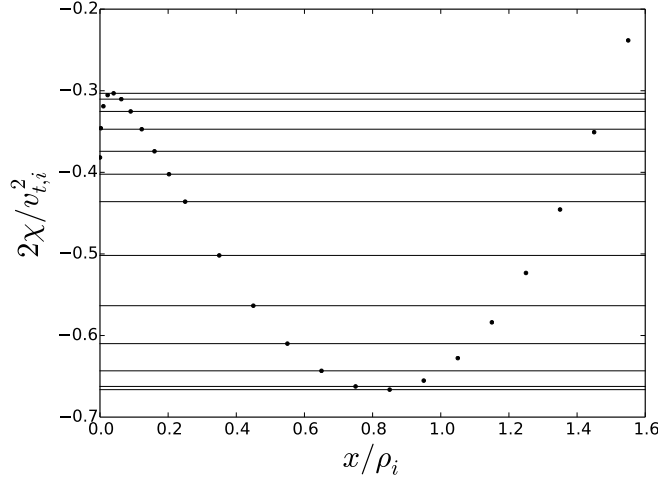


Figure 43: The values of $U_{\perp, \gamma \kappa}$ corresponding to different values of κ are shown with horizontal lines on top of the effective potential curve $\chi(x_\eta, \bar{x}_\gamma)$, for a particular value of γ . Here, κ ranges from $\kappa = 0$ (top line) to $\kappa = 12$ (bottom line).

where ι_{\max} is such that $2U/v_{ti}^2 < 15.0$ and $7.5v_{ti}^2$ is a cutoff energy above which the distribution function is essentially zero. The distribution function $F_{cl}(\mu, U)$ must be defined on a grid of values of $2\Omega\mu/v_{ti}^2$ and $2U/v_{ti}^2$. This is then bilinearly interpolated at every integration point. The integrals over U and over U_{\perp} in equations (4.7) and (4.8) are, for numerical convenience, evaluated over $v_z = \sqrt{2(U_{\gamma\kappa\iota} - U_{\perp, \gamma\kappa})}$ and $|v_x| = \sqrt{2(U_{\perp, \gamma\kappa} - \chi(x_\eta, \bar{x}_\gamma))}$, respectively (for this reason $U_{\gamma\kappa\iota}$ is defined such that linear increments in ι correspond to linear increments in v_z). Where necessary, the values of the integrands and of the integration limits of equations (2.55), (4.7), (4.8) and (4.11) are found by linear interpolation.

The iteration scheme to find $\phi(x)$ hinges on imposing

$$n_{e, \nu+1}(x_\eta) = w Z n_{i, \nu}(x_\eta) + (1 - w) n_{e, \nu}(x_\eta) \quad (4.75)$$

at every $(\nu+1)th$ iteration. Here, w is a weight whose value lies in the range $0 < w \leq 1$.
 result as the integral (to within a small numerical error).

From (4.75), $\phi_{\nu+1}(x_\eta)$ is obtained by inverting the Boltzmann relation for $n_{e,\nu+1}(x_\eta)$, and the new guess for the potential profile is thus obtained for $0 \leq \eta \leq \eta_1$. For values of η in the interval $\eta_1 + 1 \leq \eta \leq \eta_2$, the electrostatic potential $\phi_{\nu+1}(x_\eta)$ is completed by matching to the appropriate functional form for $\phi(x)$ at $x \rightarrow \infty$. With my choice of distribution function in section 4.6 marginally satisfying the Chodura condition (4.26), $\phi(x)$ satisfies equation (4.32) for large x . The value of $k_{3/2}$ is calculated numerically. The value of $C_{3/2}$ is obtained by imposing $\phi_{\nu+1}(x_{\eta_1}) = -400k_{3/2}^{-2}(x_{\eta_1} + C_{3/2})^{-4}$ to get

$$C_{3/2} = \sqrt{\frac{20}{k_{3/2}}} [-\phi_{\nu+1}(x_{\eta_1})]^{-1/4} - x_{\eta_1}. \quad (4.76)$$

The new guess for the electrostatic potential is then

$$\phi_{\nu+1}(x_\eta) = \begin{cases} \frac{T_e}{e} \ln \left(w \frac{Z n_{i\nu}(x_\eta)}{n_{e\infty}} + (1-w) \frac{n_{e\nu}(x_\eta)}{n_{e\infty}} \right) & \text{for } 0 \leq \eta \leq \eta_1, \\ -\frac{400}{k_{3/2}^2 (x_\eta + C_{3/2})^4} & \text{for } \eta_1 + 1 \leq \eta \leq \eta_2. \end{cases} \quad (4.77)$$

This can be used to evaluate $n_{i,\nu+1}(x_\eta)$ in the region $0 \leq \eta \leq \eta_1$ and continue the iteration. The first potential guess I use is a flat potential profile ($\phi_0(x_\eta) = 0$ for all η). After N iterations, a numerical solution $\phi_N(x_\eta)$ which satisfies $n_{e,N}(x_\eta) \simeq n_{i,N}(x_\eta)$ for all η is found. The deviation of $\phi_\nu(x_\eta)$ from the exact solution (which satisfies $n_i(x_\eta) = n_e(x_\eta)$) is measured by calculating the quantity

$$\tilde{n}_\nu(x_\eta) = 1 - \frac{n_{i,\nu}(x_\eta)}{n_{e,\nu}(x_\eta)}. \quad (4.78)$$

Convergence to an acceptable solution is given by the criterion that the root mean square value of $\tilde{n}_\nu(x_\eta)$ be less than some error, denoted \mathcal{E}_n ,

$$\left[\sum_{\eta=0}^{\eta_1} \frac{1}{\eta_1 + 1} \tilde{n}_\nu^2(x_\eta) \right]^{1/2} < \mathcal{E}_n. \quad (4.79)$$

For the numerical study of section 4.6, \mathcal{E}_n was set to 0.007.

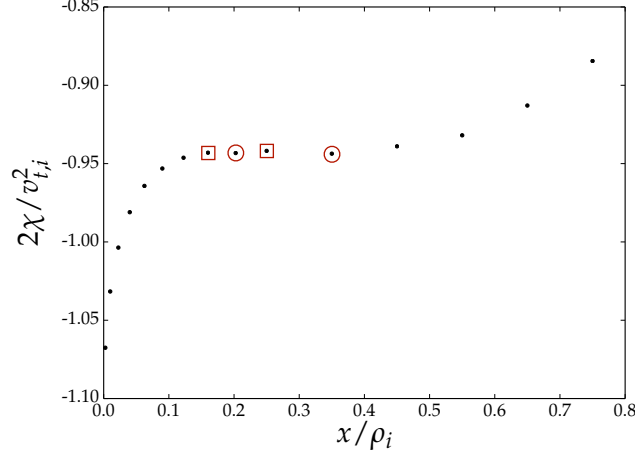


Figure 44: An example of an effective potential $\chi(x_\eta, \bar{x}_\gamma)$ in which my algorithm for generating the grid $U_{\perp, \gamma\kappa}$ fails, because it does not take into account the possibility of finding multiple effective potential minima (marked with circles) and maxima (marked with squares) for a given γ .

The method that I use can give a non-smooth numerical second derivative of the potential $\phi_\nu(x_\eta)$. The numerical noise in the second derivative is problematic because the algorithm fails to take into account the possibility of more than one maximum or minimum of the effective potential existing for some value of \bar{x} . If at some point during the iteration the function $\phi_\nu(x_\eta)$ is such that, for some value of γ , the function $\chi(x_\eta, \bar{x}_\gamma)$ has more than one index $\eta_M(\gamma)$ that satisfies either (4.70) or (4.71) (and more than one index $\eta_m(\gamma)$ that satisfies (4.72)), a more sophisticated analysis than the one I presented is necessary to obtain the grid of values of U_\perp . The appearance of multiple maxima and minima, shown in Figure 44, is due to the numerical second derivative of $\phi(x_\eta)$ having pronounced oscillations, even when $\phi(x_\eta)$ looks smooth to the naked eye. To avoid the appearance of multiple maxima and minima, in this work I perform a smoothing operation on the second derivative of $\phi_\nu(x)$ (with respect to \sqrt{x}) before iteration number $\nu + 1$, for a certain number of iterations until the densities obtained using $\phi_\nu(x)$ are

close to satisfying criterion (4.79). After that, I carry out the last few iterations without smoothing. In my iterations, $w = 0.6$ when the smoothing operation is performed, while $w = 0.2$ when it is not.

The computing time necessary to obtain the solutions that I present in the next section is small. The number of iterations required for convergence is typically less than 20, and each iteration runs in approximately 3 seconds on a laptop. Consequently, the total run time of the code on a laptop is typically less than one minute. The computing time can be further reduced by using a better initial guess, improving the integration schemes and reducing the number of integration points.

From here on, I omit all indices associated with quantities and functions evaluated numerically.

4.6 Numerical results

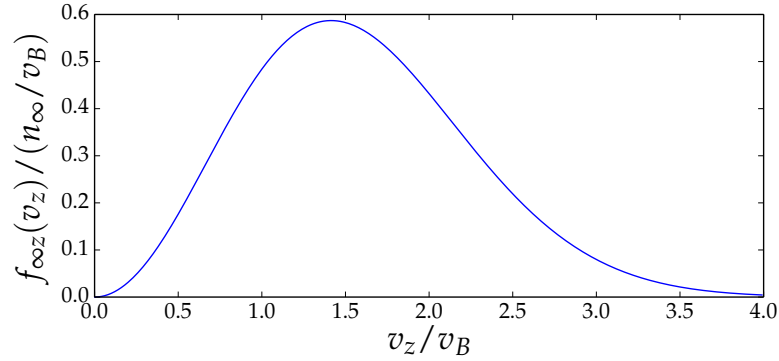


Figure 45: The distribution function in (4.80) is shown as a function of the parallel velocity v_z only, $f_{\infty z}(v_z) = \int \int f_{\infty}(\mathbf{v}) dv_x dv_y$. This distribution function marginally satisfies (4.26), $\int dv_z f_{\infty z}(v_z)/v_z^2 = n_{e\infty}/v_B^2$. Its first moment is $u_{z\infty} = (1/n_{e\infty}) \int dv_z v_z f_{\infty z}(v_z) \simeq 1.60v_B$.

In the following, I take $Z = 1$, thus considering singly charged ions. Quasineutrality

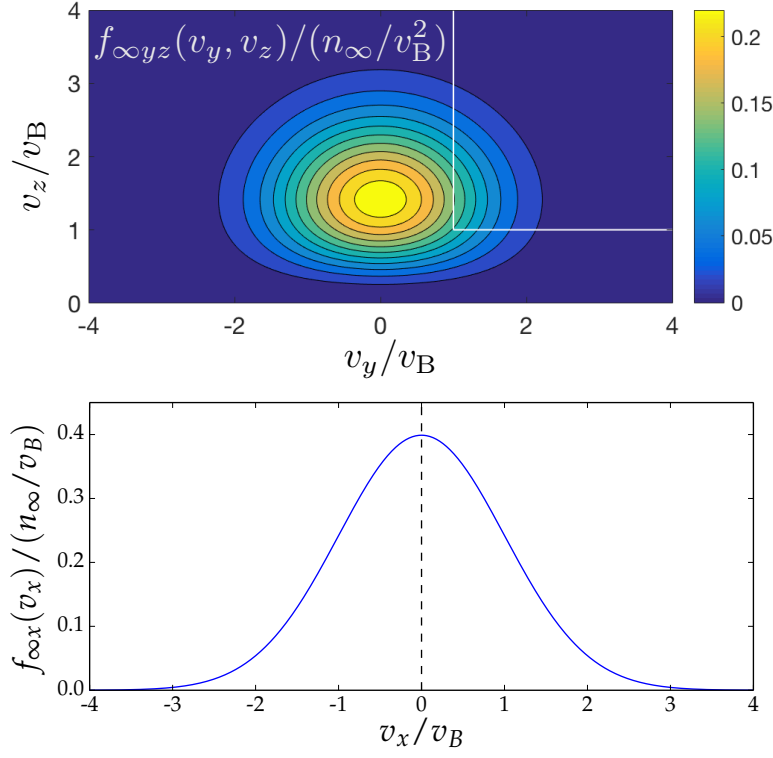


Figure 46: The distribution function (4.80) entering the magnetic presheath is shown as a function of the co-ordinates (v_x, v_y, v_z) . I define $f_{\infty x}(v_x) = \int_{-\infty}^{\infty} dv_y \int_0^{\infty} f_{\infty}(\mathbf{v}) dv_z$ and $f_{\infty yz}(v_y, v_z) = \int_{-\infty}^{\infty} f_{\infty}(\mathbf{v}) dv_x$. To compare with the distribution function $f_0(\mathbf{v})$ leaving the magnetic presheath, the box delimited by the white lines and the top right corner in the top diagram has the same size as Figure 411, and the region to the left of the dashed line in the bottom diagram is the domain of Figure 410.

(4.9) implies that the ion and electron number densities are equal, and their value at $x \rightarrow \infty$ is denoted n_{∞} . I assume the following form for the lowest order ion distribution function at the magnetic presheath entrance,

$$f_{\infty}(\mathbf{v}) = \frac{4}{\pi^{3/2}} n_{e\infty} \left(\frac{m_i}{2T_e} \right)^{5/2} v_z^2 \exp \left(-\frac{m_i |\mathbf{v}|^2}{2T_e} \right). \quad (4.80)$$

Equation (4.80) satisfies the marginal form of the kinetic Chodura condition (4.28)

$$Z v_B^2 \int \frac{f_{\infty}(\mathbf{v})}{v_z^2} d^3 v = n_{e\infty}. \quad (4.81)$$

Changing to variables μ and U , the distribution function (4.80) is

$$F_{\text{cl}}(\mu, U) = \frac{8}{\pi^{3/2}} n_{\text{e}\infty} \left(\frac{m_i}{2T_e} \right)^{5/2} (U - \Omega\mu) \exp\left(-\frac{m_i U}{T_e}\right) \Theta(v_z), \quad (4.82)$$

which is constant throughout the magnetic presheath to lowest order in α . This form was used in other studies, for example [29], and it is plotted in Figures 45 and 46. Equation (4.82) is used to obtain a discretized version of the distribution function $F_{\text{cl}}(\mu, U)$, defined on a square grid of values of $2\Omega\mu/v_{\text{ti}}^2$ and $2U/v_{\text{ti}}^2$ which lie between 0 and 15.0 in intervals of 0.05. For the distribution function (4.82), I define the ion thermal velocity $v_{\text{ti}} = \sqrt{2T_e/m_i}$ and the ion gyroradius $\rho_i = v_{\text{ti}}/\Omega$. The Bohm speed is $v_B = \sqrt{T_e/m_i} = v_{\text{ti}}/\sqrt{2}$. The distribution function (4.80) marginally satisfies the solvability condition (4.28), and the coefficient $k_{3/2}$ can be computed from (4.30), obtaining

$$\sqrt{\frac{T_e}{e}} \left(\frac{v_B}{\Omega} \right)^2 k_{3/2} = \frac{8}{3\sqrt{\pi}} \simeq 1.50. \quad (4.83)$$

The numerically calculated value of $k_{3/2}$ coincides (to within a numerical error of 2%) with equation (4.83). The average ion velocity in the z direction at the magnetic presheath entrance is

$$u_{z\infty} = \frac{1}{n_{\text{e}\infty}} \int f_{\infty}(\mathbf{v}) v_z d^3v = 2\sqrt{\frac{2}{\pi}} v_B \simeq 1.60 v_B. \quad (4.84)$$

The normalized electrostatic potential $e\phi(x)/T_e$ is shown in Figure 47 for a range of angles α . A general property of the potential curves is that they rise very steeply near $x = 0$, with the scaling $\phi(x) - \phi(0) \propto \sqrt{x}/q_2$ in that region (as can be seen explicitly in Figure 42). I have shown that this behaviour of $\phi(x)$ is expected, and it is connected with the marginal kinetic Bohm condition (4.61) being satisfied. The value of q_2 that I calculate numerically from the distribution function at $x = 0$, using equation (4.67), is consistent with the behaviour of the electrostatic potential near $x = 0$.

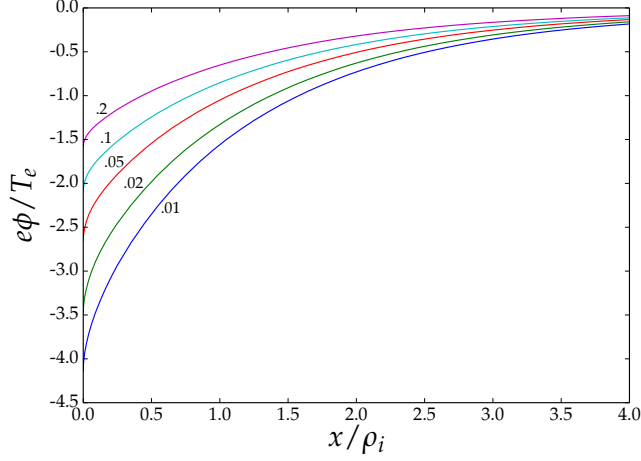


Figure 47: The electrostatic potential profile is plotted for a range of angles α , which are indicated next to the corresponding curve. Near $x = 0$, $\phi(x) - \phi(0) \propto \sqrt{x}$.

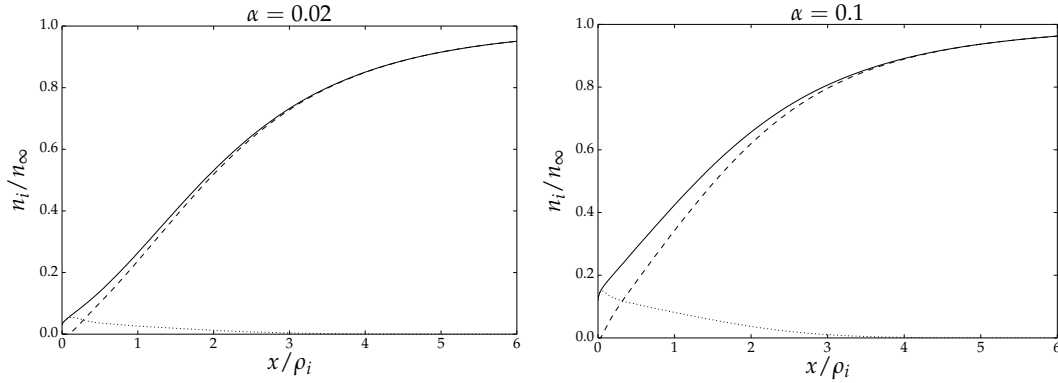


Figure 48: The ion density (solid line) for $\alpha = 0.02$ and $\alpha = 0.1$ is shown with the contributions from the closed ion orbits (dashed line) and the open orbits (dotted line) clearly marked. The open orbits clearly dominate in a very small region near $x = 0$, there is an overlap region in which the open orbit contribution and the closed orbit contribution have a similar size, while at larger values of x the closed orbit density dominates.

The ion density profiles for $\alpha = 0.02$ and $\alpha = 0.1$ are shown in Figure 48. The open orbit density can be seen to increase initially and then quickly decrease with distance from the wall. This behaviour is consistent with the behaviour of Δv_x for type II orbits

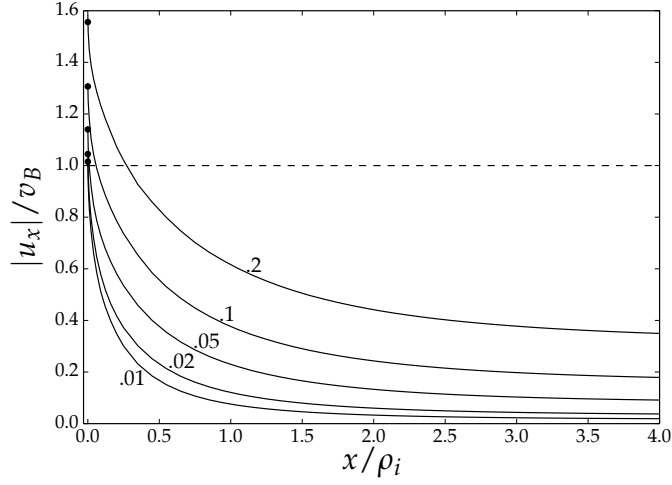


Figure 49: The average ion velocity in the direction normal to the wall is shown at various angles α (labelled next to the corresponding curve). The flow velocity obtained via the integral (4.89) is shown with a black circle at $x = 0$, which coincides with the value I calculate from continuity. The usual cold ion Bohm limit is indicated by the dashed line $|u_x|/v_B = 1$. The ion flow lies above the cold ion Bohm limit at $x = 0$ because the ions are “warm” ($T_i \neq 0$). However, at small angles $\alpha \lesssim 0.05$, the ion flow at $x = 0$ approaches the cold ion Bohm limit.

(see Figure 33 and the discussion following equation (3.40)). The open orbit density is clearly the dominant contribution to the density in the neighbourhood of $x = 0$, while for large x closed orbits give the largest contribution.

The flow velocity of ions across the magnetic presheath is commonly calculated in fluid models. Therefore, it is useful to calculate it to compare with previous results. Here I calculate the flow by using the ion continuity equation. The ion flux towards the wall across the magnetic presheath must be constant (no ion sources) due to particle conservation,

$$\frac{\partial}{\partial x} (n_i(x) u_x(x)) = 0, \quad (4.85)$$

where $u_x(x)$ is the average velocity of ions in the x direction. At the magnetic presheath entrance $x \rightarrow \infty$, the flow towards the wall is obtained from the average over the

distribution function of the gyroaveraged motion of ions towards the wall, given by $\dot{\bar{x}}$ (note that, due to distortion of the orbits, this does not remain true across the magnetic presheath). Using equations (2.34) and (2.50), the flow in the z direction, $u_{z\infty}$, is related to the flow in the x direction, $u_{x\infty}$, via $u_{x\infty} = -\alpha u_{z\infty}$. This is equivalent to the boundary condition of flow being parallel to the magnetic field at $x \rightarrow \infty$ [16]. The flow $u_{z\infty}$ is obtained as a moment of the incoming distribution function (see equation (4.84))

$$u_{z\infty} = \frac{1}{n_{e\infty}} \int f_{\infty}(\mathbf{v}) v_z d^3v. \quad (4.86)$$

The flux of ions towards the wall is conserved and therefore given by $n_i(x) u_x(x) = n_{i\infty} u_{x\infty} = -\alpha n_{i\infty} u_{z\infty}$. The average lowest order ion flow velocity towards the wall at a general position x is therefore

$$u_x(x) \simeq -\frac{\alpha n_{e\infty} u_{z\infty}}{n_i(x)}. \quad (4.87)$$

Using the quasineutrality equation, $n_i(x) = n_e(x) = n_{e\infty} \exp(e\phi(x)/T_e)$,

$$u_x(x) \simeq -\alpha u_{z\infty} \exp\left(-\frac{e\phi(x)}{T_e}\right). \quad (4.88)$$

The function (4.88) evaluated at $x = 0$ can be checked, for consistency, against the appropriate integral of the distribution function (4.62),

$$u_{x0} = \frac{1}{n_i(0)} \int f_0(\mathbf{v}) v_x d^3v. \quad (4.89)$$

In Figure 49, I plot the average ion velocity profile $u_x(x)$, obtained using equation (4.88), for a range of angles α . The magnetic presheath acceleration turns the ion flow from being (super)sonic in the direction parallel to the magnetic field to being (super)sonic in the x direction normal to the wall. At $x = 0$, the flow velocity is calculated in an alternative way, by taking the integral of the distribution function as in equation (4.89).

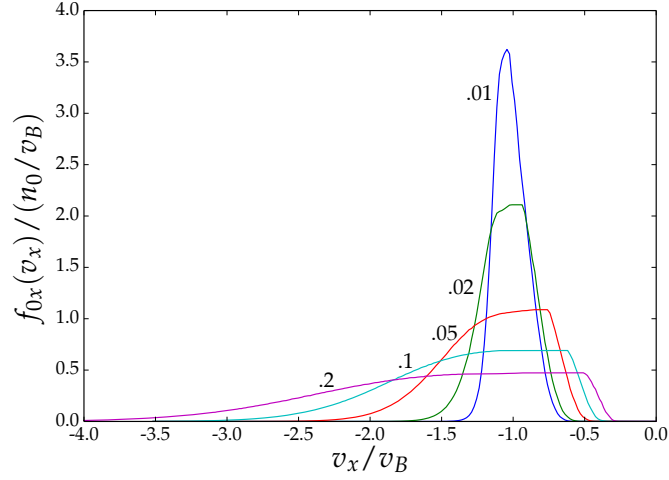


Figure 410: The distribution function $f_{0x}(v_x) = \int_{-\infty}^{\infty} dv_y \int_{-\infty}^{\infty} f_0(v_x, v_y, v_z) dv_z$ for a range of angles α , marked next to the corresponding curve.

The value thus obtained is marked on the curves for each value of α , and it is consistent with the value obtained by using equation (4.88).

By asymptotic matching, the distribution function in (4.62) is the distribution function entering the Debye sheath. In the Debye sheath, electrostatic forces normal to the wall dominate over magnetic forces, hence v_x is the only velocity component that changes significantly [31]. Therefore, only knowledge of the function

$$\begin{aligned}
 f_{0x}(v_x) &= \int_{-\infty}^{\infty} dv_y \int_{-\infty}^{\infty} f_0(v_x, v_y, v_z) dv_z \\
 &\simeq \int_{\bar{x}_{m,0}}^{\infty} \Omega d\bar{x} \int_{\chi_M(\bar{x})}^{\infty} \frac{F_{cl}(\mu(\bar{x}, \chi_M(\bar{x})), U)}{V_{||}(\chi_M(\bar{x}), U)} \\
 &\quad \times \hat{\Pi}(v_x, -V_x(0, \bar{x}, \chi_M) - \Delta v_x, -V_x(0, \bar{x}, \chi_M)) dU
 \end{aligned} \tag{4.90}$$

is needed to solve for the electrostatic potential in the Debye sheath. The distribution $f_{0x}(v_x)$ is shown in Figure 410 for a range of angles α . A general feature of this function is that it is very close to zero near $v_x = 0$. This is expected from the discussion in Section 4.4, where I concluded that there is an exponentially small number of ions with

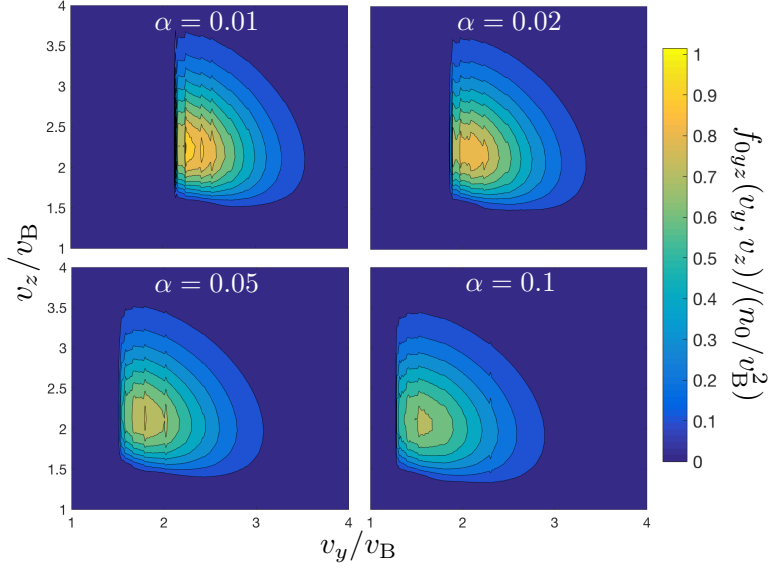


Figure 411: The distribution function $f_{0yz}(v_y, v_z) = \int_{-\infty}^0 f_0(v_x, v_y, v_z) dv_x$ for a range of angles α , marked on each panel.

small values of v_x if the distribution function F_d decays exponentially at large energy U . Another pronounced feature of Figure 410 is that the distribution function becomes narrower with decreasing α . For the cases $\alpha = 0.01$ and $\alpha = 0.02$, the distribution function is thin, approximately symmetric and centred at the Bohm speed v_B . For all angles α , the marginal form of the kinetic Bohm condition (4.61) is found to be satisfied, as I predicted in Section 4.4, with an error of $\lesssim 2\%$. A thin distribution function implies that the distribution function must be centred at the sonic speed. If the ions entering the Debye sheath have a narrow velocity distribution, this can be approximated by a Dirac delta function, $f_{0x}(v_x) \simeq \delta_{\text{Dirac}}(v_x - u_{x0})$. Substituting this approximation into (4.61), one obtains the “fluid” marginal Bohm condition $u_{x0} = v_B$.

The broadening of the distribution function $f_{0x}(v_x)$ at larger values of α is due to typical values of Δv_x , given in equation (3.31), becoming larger. The scaling $\Delta v_x \sim \sqrt{2\pi\alpha}v_{t,i}$ gives $\Delta v_x \sim v_{t,i}$ for $\alpha \sim 0.1$. The asymptotic expansion relies on Δv_x being

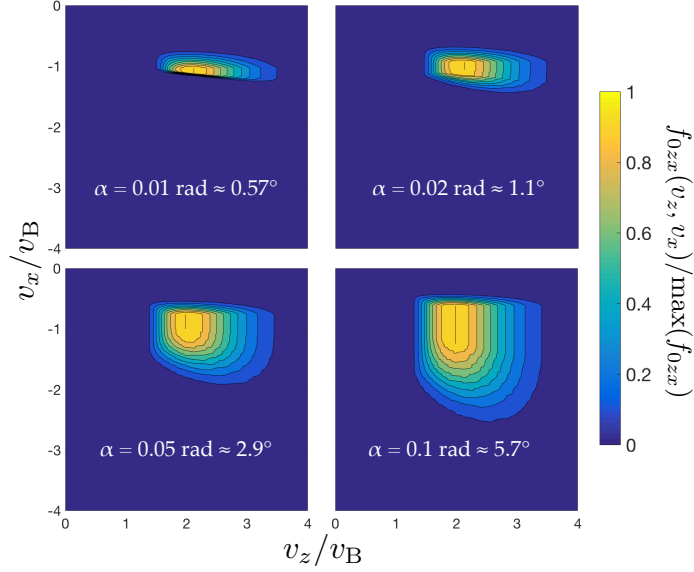


Figure 412: The distribution function $f_{0zx}(v_z, v_x) = \int_0^\infty f_0(v_x, v_y, v_z) dv_y$ for a range of angles α , marked on each panel. The distribution of the corresponding velocity components of ions entering the magnetic presheath is the same as the one shown in Figure 46, with the axis labelled v_y representing v_x .

small, so one might question the validity of my results when $\Delta v_x \sim v_{ti}$. While it is true that the accuracy of our expansion may to some extent be compromised at such large values of Δv_x , the broadening of the distribution function is expected to be physical.

In Figure 411 I show a contour plot of $f_{0yz}(v_y, v_z)$, which is given by

$$f_{0yz}(v_y, v_z) = \int f_0(v_x, v_y, v_z) dv_x \simeq F_{cl}(\mu(\bar{x}, \chi_M(\bar{x})), U) \Delta v_x, \quad (4.91)$$

where (2.28) and (3.26) can be used to re-express \bar{x} and U in terms of v_y and v_z in equation (4.91). Comparing with the distribution function at the magnetic presheath entrance (shown in Figure 46), the distribution function at $x = 0$ is narrower (it occupies a smaller area in the $v_y - v_z$ plane of phase space) and it has shifted to larger v_z and to very large and positive v_y . The net motion of the ions in the y direction can be explained by the fact that they acquire very large $\mathbf{E} \times \mathbf{B}$ velocities in the magnetic presheath (see Figure

24). A contour plot of the distribution function in the $x - z$ plane (containing the normal to the wall and the magnetic field) is also shown in Figure 412. From Figures 410, 411 and 412, I infer that ions entering the Debye sheath travel with a typical speed of $\sim 3v_B$, making an angle of $15 - 30^\circ$ with the plane parallel to the wall. The ion speed and the angle that the ion trajectory makes to the wall are expected to increase in the Debye sheath as the electric field accelerates ions in the x -direction.

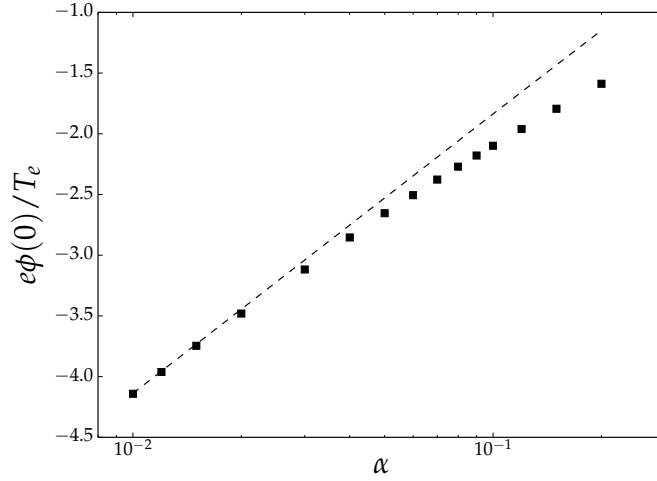


Figure 413: The total electrostatic potential drop across the magnetic presheath for a range of angles α is shown with squares. The dashed line represents the potential drop expected if the ions entering the Debye sheath are cold and the Bohm condition is marginally satisfied, $h(\alpha) = \ln(\alpha u_{z\infty}/v_B)$. For $\alpha \lesssim 0.05$, my results converge to the dashed line.

The electrostatic potential drop across the magnetic presheath is shown in Figure 413. At small angles, $e\phi(0)/T$ converges to the function

$$h(\alpha) = \ln\left(\frac{\alpha u_{z\infty}}{v_B}\right), \quad (4.92)$$

which is depicted in Figure 413 using a dashed line. The reason is the following. At $x = 0$, the flow into the wall is $n_{e\infty} \exp(e\phi(0)/T) |u_{x0}|$. Equating this to the flux

through $x \rightarrow \infty$, equal to $\alpha n_{e\infty} u_{z\infty}$, and rearranging, I obtain an expression for the potential drop in terms of the ion flows into and out of the magnetic presheath,

$$\frac{e\phi(0)}{T} = \ln \left(\frac{\alpha u_{z\infty}}{|u_{x0}|} \right). \quad (4.93)$$

Moreover, I previously found that for $\alpha \lesssim 0.05$ the cold ion Bohm condition is almost marginally satisfied, $|u_{x0}| \simeq v_B$, due to the thinness of the distribution function (see Figure 410). Then, the potential drop across the magnetic presheath can be predicted using equation (4.93) with $u_{x0} = v_B$, which is equation (4.92). Therefore, the potential drop converges to the dashed line in Figure 413.

CHAPTER 5

Ion temperature dependence

At the end of the previous chapter, a magnetic presheath in which the ion and electron temperatures are similar was studied. Setting $Z = 1$, the magnetic presheath solution depends on: (i) the angle α ; and (ii) the ion distribution function at the magnetic presheath entrance.

There is an infinite number of possible distribution functions at the magnetic presheath entrance, but only a small subset of them can be used in a realistic study. The width of the ion distribution function is characterized by the quantity $T_i = m_i v_{ti}^2/2$. In this chapter, I study the dependence of the magnetic presheath on the width of the ion distribution function using the parameter

$$\tau = \frac{T_i}{T_e} \tag{5.1}$$

by using a prescribed, arbitrary set of distribution functions.

Dependence on the ion temperature at the entrance of the magnetic presheath is important because τ is measured to be greater than unity near the divertor targets of tokamak plasmas [65]. No ions bounce back from the magnetic presheath, and thus

we expect the ion distribution function at the entrance of the magnetic presheath to be zero for $v_z < 0$. That is, the distribution function is not a Maxwellian. Fluid equations require that the distribution function be sufficiently close to a Maxwellian. If the ion temperature is small compared to the electron temperature, $\tau \ll 1$, the ions can be assumed mono-energetic and fluid equations can accurately describe the ion dynamics. Conversely, if $\tau \gtrsim 1$, the ion distribution function is very far from Maxwellian and the validity of a fluid description becomes questionable. Therefore, it is important to include the effect of a strongly non-Maxwellian ion distribution function, and the only way to do this is via a kinetic treatment of the ions such as the one carried out in this thesis.

Some of the basic orderings presented in section 2.1 change with τ . The electrostatic potential ϕ must be ordered as in (2.8) if the wall is electron-repelling. Ions falling in such a potential gain energies of order $Ze\phi \sim ZT_e$, where Ze is the ion charge. At such energies, ions have at least a velocity of the order of the Bohm speed (1.2). Hence, considering that the ion's speed must at least be equal to its thermal velocity, I order

$$|\mathbf{v}| \sim c_s = \sqrt{v_B^2 + \frac{1}{2}v_{ti}^2} = \sqrt{\frac{ZT_e + T_i}{m_i}}. \quad (5.2)$$

Note that $c_s = v_B$ when $\tau = 0$ and $c_s = v_{ti}/\sqrt{2}$ when $\tau = \infty$.

The typical size of the magnetic presheath, denoted d_{mps} , also changes with τ . In order to obtain an estimate for d_{mps} , consider the two limits $\tau \ll 1$ and $\tau \gg 1$ separately. When the ion temperature is much smaller than the electron temperature, $\tau \ll 1$, the only way by which ions can acquire the Bohm velocity v_B in the direction normal to the wall – necessary to satisfy the Bohm condition at the Debye sheath entrance [31] – is if the electric field becomes large enough that it breaks the Larmor orbits [14]. From the ordering $|\mathbf{v}| \sim v_B$ for the ion speed and by balancing the magnetic and electric forces, one obtains $\phi'(x) \sim T_e/ed_{mps} \sim v_B B$, leading to $d_{mps} \sim v_B/\Omega$. When the ion

temperature is large, $\tau \gg 1$, the length scale of the magnetic presheath is set by the ion density variation, which cannot have a characteristic length scale smaller than the ion gyroradius, giving $d_{\text{mps}} \sim \rho_i = v_{ti}/\Omega$. When $\tau \sim 1$, both arguments are valid since $\rho_i \sim v_B/\Omega$. Thus, the size of the magnetic presheath is given by the ion sound gyroradius,

$$d_{\text{mps}} \sim \rho_s = \frac{c_s}{\Omega}. \quad (5.3)$$

The rest of this chapter is structured as follows. In section 5.1, I describe the set of distribution functions used as boundary conditions. Subsequently, in section 5.2 I present numerical results obtained for a range of parameters τ using the numerical method outlined in chapter 4. The numerical results are consistent with the limits $\tau \rightarrow 0$ and $\tau \rightarrow \infty$, which are studied in sections 5.3 and 5.4 respectively. In section 5.5 I discuss the results of this chapter.

5.1 Boundary conditions

For different values of the parameter τ , the boundary condition for the ion distribution function at the magnetic presheath entrance is given by

$$f_\infty(\mathbf{v}) = \begin{cases} \mathcal{N} n_\infty \frac{4v_z^2}{\pi^{3/2} v_{ti}^5} \exp\left(-\frac{|\mathbf{v} - u\mathbf{v}_{ti}\hat{\mathbf{z}}|^2}{v_{ti}^2}\right) \Theta(v_z) & \text{for } \tau \leq 1, \\ \mathcal{N} n_\infty \frac{4v_z^2}{\pi^{3/2} v_{ti}^3 (v_{ti}^2 + \tau v_z^2)} \exp\left(-\frac{|\mathbf{v}|^2}{v_{ti}^2}\right) \Theta(v_z) & \text{for } \tau > 1. \end{cases} \quad (5.4)$$

The value of the normalization constant \mathcal{N} is (see Appendix H)

$$\mathcal{N} = \begin{cases} \left[(1 + 2u^2) (1 + \text{erf}(u)) + \frac{2u}{\sqrt{\pi}} \exp(-u^2) \right]^{-1} & \text{for } \tau \leq 1, \\ r^{3/2} \left[2\sqrt{r} - 2\sqrt{\pi} \exp\left(\frac{1}{r}\right) \left(1 - \text{erf}\left(\frac{1}{\sqrt{r}}\right)\right) \right]^{-1} & \text{for } \tau > 1, \end{cases} \quad (5.5)$$

ensuring that

$$n_\infty = \int f_\infty(\mathbf{v}) d^3v. \quad (5.6)$$

At every value of τ , the positive constant r or u is obtained by imposing the marginal form of the kinetic Chodura condition (4.28),

$$\int \frac{f_\infty(\mathbf{v})}{v_z^2} d^3v = \frac{n_\infty}{v_B^2}. \quad (5.7)$$

Hence, u satisfies the equation

$$(1 + \operatorname{erf}(u)) = \tau \left[(1 + 2u^2) (1 + \operatorname{erf}(u)) + \frac{2u}{\sqrt{\pi}} \exp(-u^2) \right], \quad (5.8)$$

and r satisfies

$$r\sqrt{\pi} \exp\left(\frac{1}{r}\right) \left(1 - \operatorname{erf}\left(\frac{1}{\sqrt{r}}\right)\right) = \tau \left[2\sqrt{r} - 2\sqrt{\pi} \exp\left(\frac{1}{r}\right) \left(1 - \operatorname{erf}\left(\frac{1}{\sqrt{r}}\right)\right) \right]. \quad (5.9)$$

Equations (5.8) and (5.9) are derived in Appendix H. The positive constant u can be determined iteratively for a given $\tau \leq 1$, and the positive constant r can be determined iteratively for a given $\tau > 1$. The fluid velocity in the z direction at the magnetic presheath entrance, $u_{z\infty}$, is evaluated in Appendix H, giving

$$\frac{u_{z\infty}}{v_{ti}} = \frac{u(3 + 2u^2)(1 + \operatorname{erf}(u)) + \frac{2\exp(-u^2)}{\sqrt{\pi}}(1 + u^2)}{(1 + 2u^2)(1 + \operatorname{erf}(u)) + \frac{2u}{\sqrt{\pi}}\exp(-u^2)} \text{ for } \tau \leq 1. \quad (5.10)$$

and

$$\frac{u_{z\infty}}{v_{ti}} = \frac{2}{\sqrt{r}\sqrt{\pi}} \frac{r - \exp\left(\frac{1}{r}\right) E_1\left(\frac{1}{r}\right)}{2\sqrt{r} - 2\sqrt{\pi} \exp\left(\frac{1}{r}\right) \left(1 - \operatorname{erf}\left(\frac{1}{\sqrt{r}}\right)\right)} \text{ for } \tau > 1. \quad (5.11)$$

In equation (5.11), I have introduced the exponential integral,

$$E_1(\xi) = \int_\xi^\infty \frac{\exp(-\eta)}{\eta} d\eta. \quad (5.12)$$

I proceed to write the distribution functions (5.4) in the variables μ and U . Using the results of Appendix E, the equations

$$\mu = \frac{v_x^2 + v_y^2}{2\Omega} \quad (5.13)$$

and

$$U = \Omega\mu + \frac{1}{2}v_z^2 \quad (5.14)$$

are valid at $x \rightarrow \infty$. From equation (5.4), (5.13) and (5.14), we can write

$$F(\mu, U) = \begin{cases} \mathcal{N}n_\infty \frac{8(U-\Omega\mu)}{\pi^{3/2}v_{ti}^5} \exp \left[-\frac{2}{v_{ti}^2} \left(\Omega\mu + \left(\sqrt{2(U-\Omega\mu)} - uv_{ti} \right)^2 \right) \right] & \text{for } \tau \leq 1, \\ \mathcal{N}n_\infty \frac{8(U-\Omega\mu)}{\pi^{3/2}v_{ti}^3(v_{ti}^2 + 2r(U-\Omega\mu))} \exp \left(-\frac{2U}{v_{ti}^2} \right) & \text{for } \tau > 1. \end{cases} \quad (5.15)$$

The boundary conditions in equation (5.4) are only one possible set. The ion distribution function entering the magnetic presheath is unknown in the absence of a kinetic solution in the bulk plasma or in the collisional presheath.

5.2 Finite ion temperature

The electrostatic potential drop across the magnetic presheath is shown in Figure 51 as a function of α and τ , for the range $0.01 \leq \alpha \leq 0.1$ and $0.2 \leq \tau \leq 10$. The numerical results approaching $\tau = 0.2$ and $\tau = 10$ are consistent with the analytical results obtained in the cold ion and cold electron limits, treated in sections 5.3 and 5.4, respectively. The shaded region is where we expect the assumption of an electron-repelling wall not to be suitable for Deuterium ions, $\alpha \lesssim \sqrt{\tau} \sqrt{m_e/m_e} \sim 0.02\sqrt{\tau}$. Considering the unshaded region in Figure 51, the potential drop with finite ion temperature is up

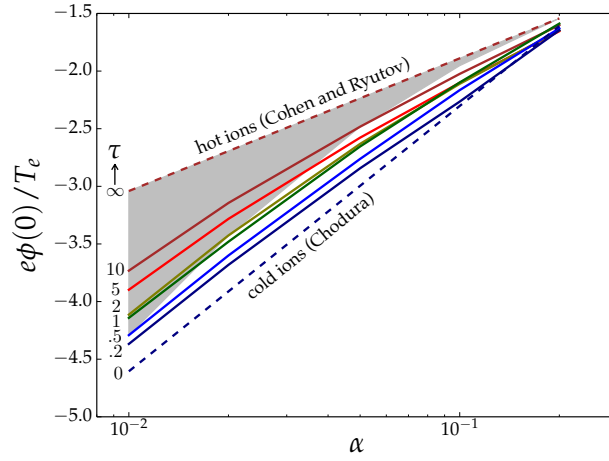


Figure 51: The electrostatic potential drop across the magnetic presheath $\phi(0)$ is shown as a function of the angle α and the parameter τ . The region where $\alpha \lesssim \sqrt{\tau} \sqrt{m_e/m_i}$, and therefore the ordering (4.2) breaks down, is shaded.

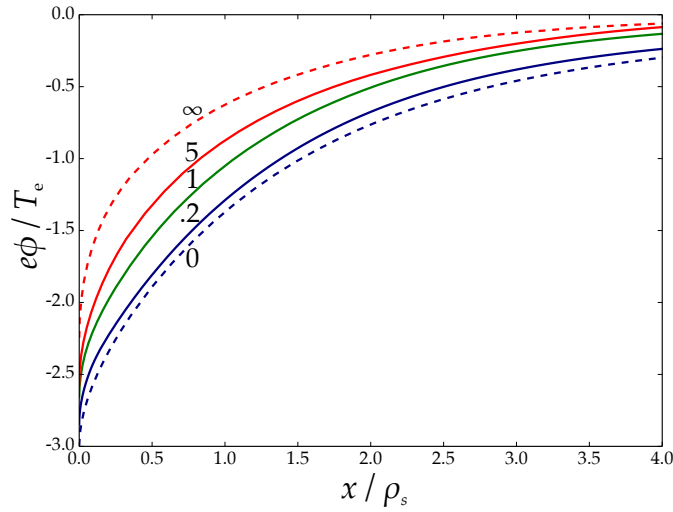


Figure 52: Electrostatic potential for $\alpha = 0.05$ at different values of τ , marked on the curves.

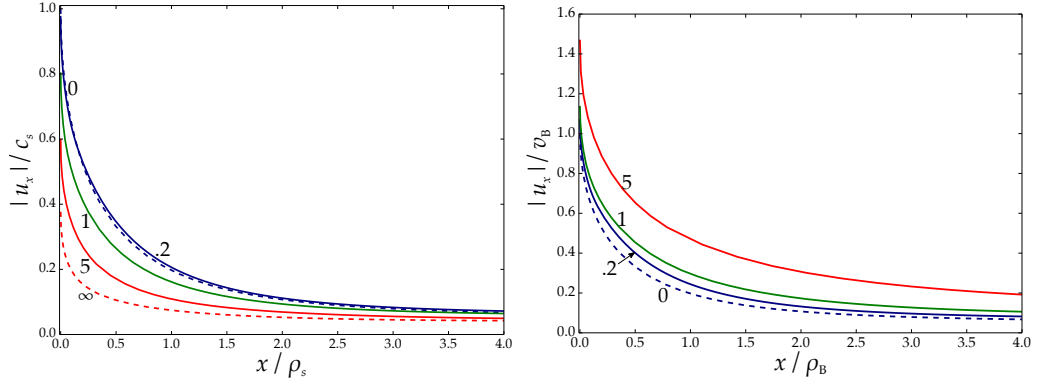


Figure 53: Flow profiles for $\alpha = 0.05$ at different values of τ , marked on the curves. The flow speed $|u_x|$ is normalized to c_s on the left and to v_B on the right. The distance from the wall is normalized to ρ_s on the left and to ρ_B on the right.

to 10 – 15% smaller than the cold ion ($\tau = 0$) potential drop. A kinetic model for electrons, as well as ions, would be necessary to study the transition from the unshaded to the shaded region. Moreover, in the shaded region, the wall may be an ion-repelling wall and hence it may be that $\phi(0) > 0$. Therefore, one would also need to relax some of the assumptions that were used to obtain the ion distribution function in chapter 3. Specifically, the backward-travelling ions reflected in the magnetic presheath or Debye sheath must be considered. Finally, note that for a sufficiently large ion current towards the wall, the wall remains electron-repelling and the potential drop shown in Figure 51 will be correct for values of $\alpha/\sqrt{\tau}$ smaller than 0.02.

The electrostatic potential profiles are shown in Figure 52. The numerical profiles lie in between the known limits $\tau = 0$ and $\tau = \infty$. The flow profiles are shown in Figure 53 for different values of τ . The ion fluid velocity is normalized to the sound speed c_s on the left diagram, and to the Bohm speed v_B on the right diagram. The numerical profiles are consistent with the low and high temperature limits $\tau = 0$ and $\tau = \infty$. The fluid velocity normal to the wall is always simultaneously sub-sonic and super-Bohm,

$v_B \leq |u_x(0)| \leq c_s$. At $\tau = 0$, the sound speed and the Bohm speed coincide and the cold ion Bohm condition, $|u_x(0)| = v_B = c_s$, is satisfied.

For different values of temperature, we plot the functions $f_{0x}(v_x)$ (defined in equation (4.90)) and $f_{\infty z}(v_z) = \int_{-\infty}^{\infty} \int_{-\infty}^{\infty} f_{\infty}(\mathbf{v}) dv_y dv_x$ in Figure 54. The kinetic Bohm condition (4.61) is numerically satisfied for all distribution functions. This is a property of the self-consistent solution of equation (4.9), as shown in section 4.4 of chapter 4. The distribution $f_{0x}(v_x)$ is found to be narrower than $f_{\infty z}(v_z)$ for all values of τ .

In Figure 55, we plot the functions $f_{\infty yz}(v_y, v_z)$ and $f_{0yz}(v_y, v_z)$. The ions have very large tangential velocities at $x = 0$ (compared with $x = \infty$) due to the large increase in the y -component of the velocity, related to the $\mathbf{E} \times \mathbf{B}$ drift acquired by the ion orbit in the magnetic presheath.

5.3 Zero ion temperature limit

When $T_i = 0$, the ion equations of motion become the equations for the ion fluid velocity. Letting $\mathbf{u} = (u_x, u_y, u_z)$ be the ion fluid velocity, the momentum equation for the ion species is, in components,

$$u_x u'_x = -\frac{\Omega \phi'}{B} + \Omega u_y \cos \alpha, \quad (5.16)$$

$$u_x u'_y = -\Omega u_x \cos \alpha - \Omega u_z \sin \alpha, \quad (5.17)$$

$$u_x u'_z = \Omega u_y \sin \alpha. \quad (5.18)$$

Here, ' indicates differentiation with respect to x . The momentum equations (5.16)-(5.18) follow from the particle equations of motion (2.22)-(2.24) in section (2.2.1), by replacing

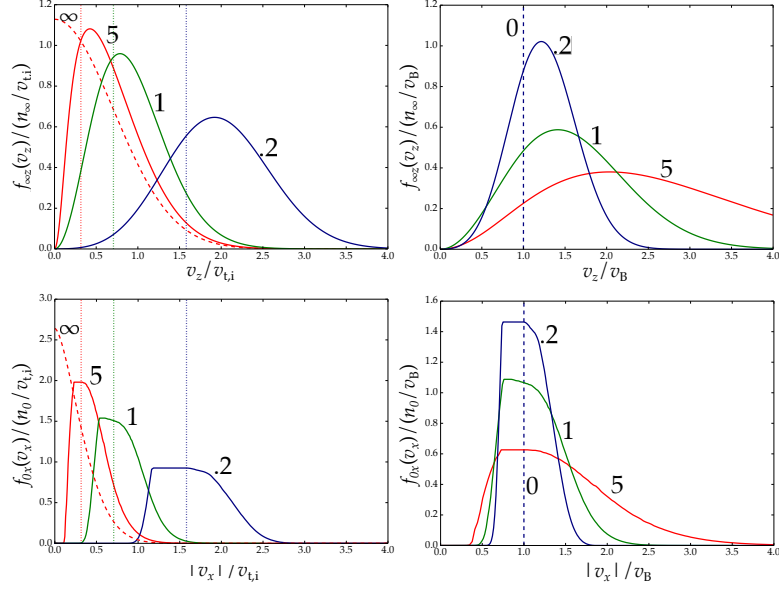


Figure 54: The distributions of the component v_z of the ion velocity at the magnetic presheath entrance $x \rightarrow \infty$ (top) and the component v_x of the velocity at the Debye sheath entrance $x = 0$ (bottom) are shown for $\alpha = 0.05$ for three different values of the parameter τ , labelled next to the corresponding curve. The velocities are normalized to v_{ti} on the left diagrams and to v_B on the right diagrams. Magnetized ions at the magnetic presheath entrance move parallel to the magnetic field. Hence, v_z is responsible for the flow of ions to the wall. At the Debye sheath entrance, the ion flow towards the wall is determined by $|v_x|$. The red dashed lines on the left diagrams are the distribution functions in the limit $\tau \rightarrow \infty$. The blue vertical dashed lines on the right diagrams are the cold ion distribution functions, $\tau = 0$.

the ion velocity \mathbf{v} with the ion fluid velocity \mathbf{u} and using $u_x = \dot{x}$ to write $\dot{\mathbf{u}} = u_x \mathbf{u}'$ (thus changing the time derivative of every velocity component to a spatial derivative). The fluid velocity at $x \rightarrow \infty$ is denoted \mathbf{u}_{∞} . Equations (5.16)-(5.18) are solved using the

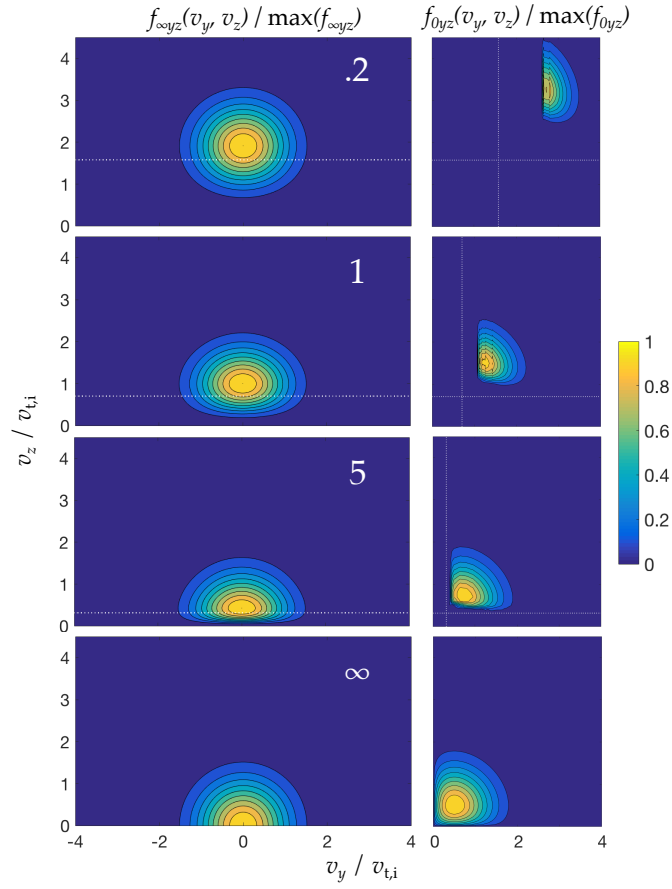


Figure 55: The ion distribution functions $f_{\infty yz}(v_y, v_z)$ (left) and $f_{0yz}(v_y, v_z)$ (right) for $\alpha = 0.05$ and, from top to bottom, for $\tau = 0.2$, $\tau = 1$, $\tau = 5$ and $\tau = \infty$ (see section 5.4). The Bohm speed $v_B/v_{t,i} = 1/\sqrt{2\tau}$ is marked as a horizontal line in all panels, and also as a vertical line on the right panels.

boundary conditions of a flow that is aligned with the magnetic field,

$$\mathbf{u}_\infty = \begin{pmatrix} u_{x\infty} \\ u_{y\infty} \\ u_{z\infty} \end{pmatrix} = \begin{pmatrix} -u_\infty \sin \alpha \\ 0 \\ u_\infty \cos \alpha \end{pmatrix}. \quad (5.19)$$

The quasineutrality equation, together with the electron Boltzmann distribution and the ion continuity equation, gives the equation

$$u_x = u_{x\infty} \exp\left(-\frac{e\phi}{T_e}\right). \quad (5.20)$$

The derivation of (5.20) is identical to that of (4.88), but uses $u_x = u_{x\infty}$ at $x \rightarrow \infty$. Then, differentiating (5.20) and rearranging, one obtains

$$\phi' = -\frac{T_e}{e} \frac{u'_x}{u_x}. \quad (5.21)$$

I follow Riemann's derivation of a first order differential equation for u_x from equations (5.16)-(5.18) and (5.21) [16]. The original derivation is due to Chodura [15]. Equation (5.16) can be rearranged to obtain

$$u_y = \frac{\phi'}{B \cos \alpha} + \frac{u_x u'_x}{\Omega \cos \alpha}. \quad (5.22)$$

By substituting equation (5.21) into equation (5.22), one obtains

$$u_y = -\frac{v_B^2 u'_x}{u_x \Omega \cos \alpha} + \frac{u_x u'_x}{\Omega \cos \alpha}, \quad (5.23)$$

which can be substituted in equation (5.18) to obtain

$$u'_z = \tan \alpha \left(1 - \frac{v_B^2}{u_x^2}\right) u'_x. \quad (5.24)$$

Using the boundary conditions in (5.19), equation (5.24) integrates to

$$u_z = u_x \tan \alpha + \frac{v_B^2 \tan \alpha}{u_x} + \frac{u_\infty}{\cos \alpha} + \frac{v_B^2}{u_\infty \cos \alpha}. \quad (5.25)$$

Analogously to the procedure for deriving conservation of energy for a single particle, one can add equations (5.16)-(5.18) multiplied by u_x , u_y and u_z respectively, and divide by u_x again to obtain

$$\frac{1}{2} u_\infty^2 = \frac{1}{2} u_x^2 + \frac{1}{2} u_y^2 + \frac{1}{2} u_z^2 + \frac{\Omega \phi}{B}, \quad (5.26)$$

where we used $\phi(x) = 0$ at $x \rightarrow \infty$ and the boundary conditions (5.19). Substituting equations (5.23) and (5.25) into the energy equation (5.26), one obtains the differential equation

$$\frac{(u_x^2 - v_B^2)^2}{u_x^2 \Omega^2 \cos^2 \alpha} u_x'^2 = f(u_x), \quad (5.27)$$

where

$$f(u_x) = u_\infty^2 - u_x^2 - 2v_B^2 \ln \left(\frac{u_\infty \sin \alpha}{-u_x} \right) - \left(\tan \alpha \left(u_x + \frac{v_B^2}{u_x} \right) + \frac{u_\infty + \frac{v_B^2}{u_\infty}}{\cos \alpha} \right)^2. \quad (5.28)$$

Equation (5.27) is solved by realizing that the singularity occurring when $u_x = -v_B$ corresponds to the Debye sheath entrance, $x = 0$ [15, 16]. Then the position x is the definite integral

$$x = \int_{-v_B}^{u_x} \frac{\eta^2 - v_B^2}{\eta \Omega \cos \alpha} [f(\eta)]^{-1/2} d\eta. \quad (5.29)$$

This equation can be inverted to obtain $u_x(x)$, and then equation (5.20) can be used to obtain $\phi(x)$.

Taking $\alpha \ll 1$, the direction of the fluid velocity at $x \rightarrow \infty$ is, to lowest order, along the z -axis. Hence, $u_\infty \simeq u_{z\infty}$. At the Debye sheath entrance, the Bohm condition is satisfied and thus $u_x \sim v_B$ close to $x = 0$. Therefore, the size of u_x changes from $\sim \alpha v_B$ to $\sim v_B$ from $x \rightarrow \infty$ to $x = 0$. For $u_x \sim \alpha v_B$, the lowest order terms in equations (5.27) and (5.28) give

$$\frac{v_B^2}{\Omega^2} \left(\frac{u_x'}{u_x} \right)^2 = -\frac{v_B^2}{u_{z\infty}^2} - 2 + 2 \ln \left(\frac{-u_x}{\alpha u_{z\infty}} \right) - \frac{\alpha^2 v_B^2}{u_x^2} + \frac{2\alpha v_B^2}{-u_x u_{z\infty}} + \frac{2\alpha u_{z\infty}}{-u_x}. \quad (5.30)$$

For $u_x \sim v_B$, the lowest order terms in (5.27) and (5.28) give

$$\frac{(v_B^2 - u_x^2)^2}{v_B^2 u_x^2} \frac{u_x'^2}{\Omega^2} = -\frac{u_x^2}{v_B^2} - \frac{v_B^2}{u_{z\infty}^2} - 2 + 2 \ln \left(\frac{-u_x}{\alpha u_{z\infty}} \right). \quad (5.31)$$

Equations (5.30) and (5.31) both result in the same equation to lowest order in α in the limit $\alpha \ll u_x/v_B \ll 1$,

$$\frac{v_B^2}{u_x^2} \frac{u_x'^2}{\Omega^2} = -\frac{v_B^2}{u_{z\infty}^2} - 2 + 2 \ln \left(\frac{-u_x}{\alpha u_{z\infty}} \right). \quad (5.32)$$

A lowest order equation in α valid for all values of u_x is

$$\frac{(v_B^2 - u_x^2)^2}{v_B^2 u_x^2} \frac{u_x'^2}{\Omega^2} = f_\alpha(u_x), \quad (5.33)$$

with

$$f_\alpha(u_x) = -\frac{(u_x + \alpha u_{z\infty})^2}{v_B^2} - \frac{v_B^2}{u_{z\infty}^2} - 2 + 2 \ln \left(\frac{-u_x}{\alpha u_{z\infty}} \right) - \frac{\alpha^2 v_B^2}{u_x^2} + \frac{2\alpha v_B^2}{-u_{z\infty} u_x} + \frac{2\alpha u_{z\infty}}{-u_x}. \quad (5.34)$$

Equations (5.33) and (5.34) are obtained by expanding (5.27) and (5.28) in α and keeping enough lowest order terms such that the conditions $f_\alpha(-\alpha u_{z\infty}) = f'_\alpha(-\alpha u_{z\infty}) = 0$ are satisfied. These conditions correspond to the electrostatic potential and ion flow tending to a constant value at $x \rightarrow \infty$ [16].

By imposing the equality form of the fluid Chodura condition, $u_{z\infty} = v_B$, in (5.33) and (5.34), one obtains

$$\frac{(v_B^2 - u_x^2)^2}{v_B^2 u_x^2} \frac{u_x'^2}{\Omega^2} = -\frac{(u_x + \alpha v_B)^2}{v_B^2} - 3 + 2 \ln \left(\frac{-u_x}{\alpha v_B} \right) - \frac{\alpha^2 v_B^2}{u_x^2} - \frac{4\alpha v_B}{u_x}. \quad (5.35)$$

The solution of (5.35) is

$$x = \int_{-v_B}^{u_x} \frac{\eta^2 - v_B^2}{\eta \Omega} \left[-\frac{(\eta + \alpha v_B)^2}{v_B^2} - 3 + 2 \ln \left(\frac{-\eta}{\alpha v_B} \right) - \frac{\alpha^2 v_B^2}{\eta^2} - \frac{4\alpha v_B}{\eta} \right]^{-1/2} d\eta. \quad (5.36)$$

The ion flow u_x is obtained by inverting (5.36). The electrostatic potential profile is then obtained by using the equation relating flow and potential, (4.88),

$$\phi(x) = -\frac{T_e}{e} \ln \left(\frac{-u_x(x)}{\alpha v_B} \right). \quad (5.37)$$

With the flow solution to (5.35) marginally satisfying Bohm's condition at the Debye sheath entrance ([31, 50]), $u_x(0) = -v_B$, the potential drop is

$$\phi(0) = -\frac{T_e}{e} \ln \left(\frac{1}{\alpha} \right). \quad (5.38)$$

In section 4.4, it was shown that there cannot be any type I orbits, and hence $\phi(x) - \phi(0) \propto \sqrt{x}$ for $x \rightarrow 0$. As a result, the critical point x_c (defined in equation (2.39)) must be non-zero, and there exists a value of orbit position \bar{x}_c for which the effective potential $\chi(x, \bar{x}_c)$ has a point of inflection with zero derivative at x_c . For each \bar{x} , closed orbits with $\mu \sim \tau v_B^2 / \Omega$ must lie in a region surrounding the effective potential minimum, and the size of this region is small for $\tau \ll 1$ and $x \gg x_c$. Since minima of the effective potential only exist for $x > x_c$, most closed orbits must lie in the region $x \gg x_c$, while only open orbits reach the region $x \ll x_c$, as shown schematically in Figure 56. In Figure 56, a set of effective potential curves corresponding to the solution of the fluid equation (5.36) for $\alpha = 0.05$ are shown. It can be seen that the effective potential curves corresponding to minima near x_c are very flat. Hence, for $\tau \ll 1$, the size of closed orbits approaching x_c from large x grows and can become of the order of the system scale length, ρ_B .

From this discussion, the quasineutrality equation (4.9) evaluated for $\tau \ll 1$ leads to three regions of interest: $x \gg x_c$, $x \sim x_c$ and $x \ll x_c$. In subsection 5.3.1, I show that the quasineutrality equation (4.9) for $x \gg x_c$ reduces to equation (5.30), which is the fluid differential equation obtained for $u_x \sim \alpha v_B$. In subsection 5.3.2, I show that the quasineutrality equation for $x \ll x_c$ reduces to the form in equation (5.31), which is the fluid differential equation obtained for $u_x \sim v_B$. In subsection 5.3.3, I discuss the intermediate region $x \sim x_c$.

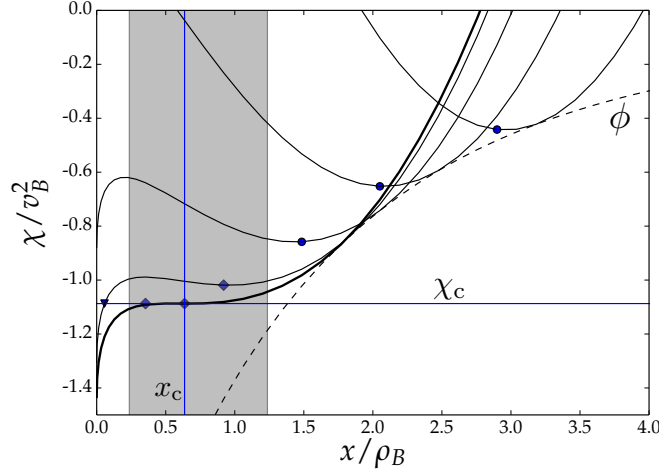


Figure 56: Some effective potential curves $\chi(x, \bar{x})$, corresponding to the electrostatic potential profile $\phi(x)$ (dashed line) that solves the magnetic presheath for $\tau = 0$ and $\alpha = 0.05$, are shown for a range of values of \bar{x} (where the dashed line intersects the solid lines, $\chi(x, \bar{x}) = \phi(x)$ hence $x = \bar{x}$). The position of an ion with $\mu = 0$ corresponding to each value of \bar{x} is shown by a marker: (i) a circle if the ion is in a closed orbit to the right of the shaded region, $x \gg x_c$; (ii) a triangle if the ion is in an open orbit to the left of the shaded region, $x \ll x_c$; (iii) a diamond if the ion is in the shaded region, $x \sim x_c$, transitioning from a closed to an open orbit. In the shaded transition one finds $\chi''(x, \bar{x}) \simeq 0$ and $\chi'''(x, \bar{x}) = \phi'''(x, \bar{x}) \simeq 0$.

5.3.1 Closed orbit region ($x \gg x_c$)

At large values of x the ion density is dominated by closed orbits. For $\tau \ll 1$, the distribution function (5.4) is clustered in a thin region a few $v_{t,i}$ from $v_z = uv_{t,i} \simeq u_{z\infty} \gg v_{t,i}$. In terms of μ and U , equation (5.15) reduces to a very thin Maxwellian for $\tau \rightarrow 0$,

$$F(\mu, U) = \frac{1}{2\pi^{3/2}\tau^{3/2}} \left(\frac{m_i}{2\tau T_e} \right)^{3/2} \exp\left(-\frac{m_i \Omega \mu}{2\tau T_e}\right) \times \exp\left(-\frac{m_i \left(\sqrt{2(U - \Omega \mu)} - u_{z\infty}\right)^2}{2\tau T_e}\right). \quad (5.39)$$

For most of this section, we consider the general case $u_{z\infty} \geq v_B$, but the numerical results are all based on equation (5.15) and hence $u_{z\infty} = v_B$. Expanding the square root

in the exponential around $\sqrt{2(U - \Omega\mu)} = u_{z\infty}$ gives

$$\sqrt{2(U - \Omega\mu)} = \sqrt{u_{z\infty}^2 + 2\left(U - \Omega\mu - \frac{1}{2}u_{z\infty}^2\right)} \simeq u_{z\infty} \left(1 + \frac{(U - \Omega\mu - \frac{1}{2}u_{z\infty}^2)}{u_{z\infty}^2}\right). \quad (5.40)$$

Hence, the distribution function is

$$F(\mu, U) = \left(\frac{m_i}{2\tau T_e \pi}\right)^{3/2} \exp\left(-\frac{m_i \Omega \mu}{\tau T_e}\right) \exp\left(-\frac{m_i (U - \Omega\mu - \frac{1}{2}u_{z\infty}^2)^2}{2\tau T_e u_{z\infty}^2}\right). \quad (5.41)$$

Considering that $e\phi \sim T_e$, I order $\Omega\mu \sim U \sim T_e/m_i$, thus when taking $\tau \rightarrow 0$ equation (5.39) is equivalent to the product of two Dirac delta functions

$$F(\mu, U) = \frac{u_{z\infty}}{2\pi\Omega} \delta(\mu) \delta\left(U - \frac{1}{2}u_{z\infty}^2\right). \quad (5.42)$$

For $\tau \ll 1$ and $x \gg x_c$, the particle is confined close to the minimum, $x \simeq x_m$, and the effective potential looks like a parabola locally near the minimum. Hence,

$$\chi(x, \bar{x}) - \chi_m(\bar{x}) \simeq \frac{1}{2}\chi''(x)(x - x_m)^2. \quad (5.43)$$

Using equation (2.38), we have that

$$\Omega^2(\bar{x} - x_m) = \frac{\Omega\phi'(x_m)}{B}. \quad (5.44)$$

From $x \simeq x_m$, one finds $U_\perp \simeq \chi(x, \bar{x}) \simeq \chi_m(\bar{x})$, and using equation (5.44), it follows that

$$U_\perp \simeq \frac{1}{2}\left(\frac{\phi'(x)}{B}\right)^2 + \frac{\Omega\phi(x)}{B}. \quad (5.45)$$

The adiabatic invariant is

$$\mu \simeq \frac{\sqrt{2(U_\perp - \chi_m(\bar{x}))}}{\pi} \int_{x_b}^{x_t} \sqrt{1 - \frac{\chi''(x_m)(x - x_m)^2}{2(U_\perp - \chi(x_m))}} dx, \quad (5.46)$$

with $x_b = x_m - \sqrt{2(U_\perp - \chi_m(\bar{x})) / \chi''(x_m)}$ and $x_t = x_m + \sqrt{2(U_\perp - \chi_m(\bar{x})) / \chi''(x_m)}$.

Upon using $\chi''(x_m) \simeq \chi''(x)$, equation (5.46) reduces to

$$\mu \simeq \frac{U_\perp - \chi_m(\bar{x})}{\sqrt{\chi''(x)}}. \quad (5.47)$$

Inserting the distribution function of equation (5.39) into the closed orbit integral (4.7)

and changing from U_\perp to μ using equation (5.47) gives

$$n_{i,cl}(x) = \int_{\bar{x}_m(x)}^{\infty} \Omega d\bar{x} \int_0^{\infty} \frac{2\sqrt{\chi''(x)}d\mu}{\sqrt{2\left(\sqrt{\chi''(x)}\mu + \chi_m(\bar{x}) - \chi(x, \bar{x})\right)}} \times \int_{\Omega\mu}^{\infty} \frac{F(\mu, U)dU}{\sqrt{2\left(U - \frac{1}{2}\left(\frac{\phi'}{B}\right)^2 - \frac{\Omega\phi}{B}\right)}}. \quad (5.48)$$

The upper limit of integration in μ is allowed to be ∞ for $x \gg x_c$ because $F(\mu, U)$ is exponentially small for orbits with $\mu \gg \tau v_B^2 / \Omega$.

To take the integral in equation (5.48), I change variable from \bar{x} to x_m . From (5.44) one obtains the relation

$$\frac{\partial \bar{x}}{\partial x_m} = \frac{\chi''(x_m)}{\Omega^2} \simeq 1 + \frac{\phi''(x)}{\Omega B}. \quad (5.49)$$

Using (5.43) and (5.49), equation (5.48) becomes

$$n_{i,cl}(x) = \frac{\chi''(x)}{\Omega^2} \int_0^{\infty} d\mu \int_{\Omega\mu}^{\infty} \frac{F(\mu, U)dU}{\sqrt{2\left(U - \frac{1}{2}\left(\frac{\phi'(x)}{B}\right)^2 - \frac{\Omega\phi(x)}{B}\right)}} \times \int_{x - \frac{\sqrt{2\mu}}{(\chi''(x))^{1/4}}}^{x + \frac{\sqrt{2\mu}}{(\chi''(x))^{1/4}}} \frac{2\sqrt{\chi''(x)}dx_m}{\sqrt{2\left(\sqrt{\chi''(x)}\mu - \frac{1}{2}\chi''(x)(x - x_m)^2\right)}}. \quad (5.50)$$

Note that the order of integration was changed in order to obtain (5.50). The rightmost

integral evaluates to 2π , and thus equation (5.50) becomes

$$n_{i,cl}(x) = \frac{2\pi\chi''(x)}{\Omega^2} \int_0^\infty d\mu \int_{\Omega\mu}^\infty \frac{F(\mu, U) dU}{\sqrt{2 \left(U - \frac{1}{2} \left(\frac{\phi'(x)}{B} \right)^2 - \frac{\Omega\phi(x)}{B} \right)}}. \quad (5.51)$$

Equation (5.50) is valid for $x \gg x_c$. To lowest order in $\tau \ll 1$, one can substitute equation (5.42) for the distribution function to obtain

$$n_{i,cl}(x) = \frac{n_\infty u_{z\infty} \chi''(x)}{\Omega} \int_0^\infty \delta(\mu) d\mu \int_{\Omega\mu}^\infty \frac{\delta \left(U - \frac{1}{2} u_{z\infty}^2 \right)}{\sqrt{2 \left(U - \frac{1}{2} \left(\frac{\phi'(x)}{B} \right)^2 - \frac{\Omega\phi(x)}{B} \right)}} dU. \quad (5.52)$$

Taking the straightforward integrals over Dirac delta functions, the density of closed orbits is

$$n_{i,cl}(x) = \frac{n_\infty u_{z\infty} \left(1 + \frac{\phi''(x)}{\Omega B} \right)}{\sqrt{u_{z\infty}^2 - \left(\frac{\phi'(x)}{B} \right)^2 - \frac{2\Omega\phi(x)}{B}}}. \quad (5.53)$$

Note that equation (5.53) satisfies $n_{i,cl}(x) \rightarrow 0$ for $x \rightarrow x_c$, since $1 + \phi''(x_c)/\Omega B = 0$.

The quasineutrality equation (4.9) for cold ions in the region $x \gg x_c$ is, using $n_{i,op}(x) = 0$ and equation (5.53),

$$\exp \left(\frac{e\phi}{T_e} \right) = \frac{u_{z\infty} \left(1 + \frac{\phi''}{\Omega B} \right)}{\sqrt{u_{z\infty}^2 - \left(\frac{\phi'}{B} \right)^2 - \frac{2\Omega\phi}{B}}}. \quad (5.54)$$

Multiplying equation (5.54) by $\Omega\phi'/B$, integrating once and using the boundary condition $\phi = \phi' = 0$ at $x \rightarrow \infty$ I obtain

$$v_B^2 \exp \left(\frac{e\phi}{T_e} \right) = v_B^2 + u_{z\infty}^2 - u \sqrt{u_{z\infty}^2 - \left(\frac{\phi'}{B} \right)^2 - \frac{2\Omega\phi}{B}}, \quad (5.55)$$

which can be rearranged to

$$\left(\frac{\phi'}{B} \right)^2 = u_{z\infty}^2 - \frac{2\Omega\phi}{B} - \frac{v_B^4}{u_{z\infty}^2} \left(1 + \frac{u_{z\infty}^2}{v_B^2} - \exp \left(\frac{e\phi}{T_e} \right) \right)^2. \quad (5.56)$$

Using the relation (4.88) between fluid velocity and potential leads to equation (5.30).

Hence, Chodura's differential equation is recovered for $x \gg x_c$.

5.3.2 Open orbit region ($x \ll x_c$)

I proceed to evaluate the quasineutrality equation (4.9) in the region $x \ll x_c$. In order to do so, I calculate the open orbit density for $\tau \ll 1$. While an ion is in an open orbit, it falls down the effective potential well in the region $x \ll x_c$. The perpendicular energy of the open orbit remains constant to lowest order in α , taking the value it had at the effective potential maximum. From Figure 56, the perpendicular energy is given, to lowest order in α and τ , by

$$U_{\perp} \simeq \chi_M \simeq \chi_c = \chi(x_c, \bar{x}_c). \quad (5.57)$$

For $x \ll x_c$, one can use $\Delta_M \sim \alpha v_{ti}^2$ and $\chi_c - \chi(x, \bar{x}_c) \sim v_B^2$ to show that $\Delta_M \ll \chi_c - \chi$. Then, equation (3.31) is expanded to give

$$\Delta v_x \simeq \frac{\Delta_M}{\sqrt{2 \left(\chi_c - \frac{1}{2} \Omega^2 (x - \bar{x}_c)^2 - \frac{\Omega \phi(x)}{B} \right)}}. \quad (5.58)$$

In what follows, I denote $d\mu/d\bar{x}|_{\text{open}} = d\mu(\bar{x}, \chi_M(\bar{x}))/d\bar{x}$. By changing variable from \bar{x} to μ and substituting (5.58), the integral (4.8) simplifies to

$$n_{i,\text{op}} = \frac{1}{\sqrt{2 \left(\chi_c - \frac{1}{2} \Omega^2 (x - \bar{x}_c)^2 - \frac{\Omega \phi(x)}{B} \right)}} \int_0^{\infty} \left. \frac{d\mu}{d\bar{x}} \right|_{\text{open}}^{-1} \Omega d\mu \times \int_{\Omega\mu}^{\infty} \frac{F(\mu, U) \Delta_M dU}{\sqrt{2(U - \chi_c)}}. \quad (5.59)$$

To evaluate (5.59), one uses the relation

$$\Delta_M \simeq 2\pi\alpha \sqrt{2(U - \chi_c)} \left. \frac{d\mu}{d\bar{x}} \right|_{\text{open}}, \quad (5.60)$$

obtained using (4.10) and (4.11). Inserting equation (5.60) into (5.59) gives

$$n_{i,\text{op}} = \frac{2\pi\alpha}{\sqrt{2 \left(\chi_c - \frac{1}{2} \Omega^2 (x - \bar{x}_c)^2 - \frac{\Omega \phi(x)}{B} \right)}} \int_0^{\infty} \Omega d\mu \int_{\Omega\mu}^{\infty} F(\mu, U) dU. \quad (5.61)$$

Using (5.42) for the distribution function, the density of open orbits is

$$n_{i,op}(x) = \frac{\alpha n_\infty u_{z\infty}}{\sqrt{2 \left(\chi_c - \frac{1}{2} \Omega^2 (x - \bar{x}_c)^2 - \frac{\Omega \phi}{B} \right)}}, \quad (5.62)$$

valid for $x \ll x_c$. For $x \rightarrow x_c$, the open orbit density diverges, $n_{i,op}(x) \rightarrow \infty$, while we previously found that the closed orbit density goes to zero at the same point, $n_{i,cl}(x) \rightarrow 0$. Both estimates were derived by considering positions far from the critical point and are thus not valid in the region $x \sim x_c$.

Imposing quasineutrality (4.9) in the region $x \ll x_c$ using $n_{i,cl}(x) = 0$ and equation (5.62), one obtains

$$\exp\left(\frac{e\phi}{T_e}\right) = \frac{\alpha u_{z\infty}}{\sqrt{2\chi_c - \Omega^2(x - \bar{x}_c)^2 - \frac{2\Omega\phi}{B}}}. \quad (5.63)$$

The constants χ_c and \bar{x}_c are to be determined, because they depend on the form of the solution ϕ . Rearranging equation (5.63) gives

$$\Omega^2(x - \bar{x}_c)^2 = 2\chi_c - \frac{2\Omega\phi}{B} - \alpha^2 u_{z\infty}^2 \exp\left(-\frac{2e\phi}{T_e}\right), \quad (5.64)$$

which is differentiated to obtain

$$\Omega^2(x - \bar{x}_c) = \frac{e\phi'}{T_e} \left(\alpha^2 u_{z\infty}^2 \exp\left(-\frac{2e\phi}{T_e}\right) - v_B^2 \right). \quad (5.65)$$

Hence, inserting equation (5.65) into (5.64), the constant \bar{x}_c is eliminated and the first order differential equation

$$\left(\frac{e\phi'}{\Omega T_e}\right)^2 \left(\alpha^2 u_{z\infty}^2 \exp\left(-\frac{2e\phi}{T_e}\right) - v_B^2 \right)^2 = 2\chi_c - \frac{2\Omega\phi}{B} - \alpha^2 u_{z\infty}^2 \exp\left(-\frac{2e\phi}{T_e}\right) \quad (5.66)$$

is obtained. Using the equation relating fluid velocity to electrostatic potential, (4.88), gives a differential equation for u_x ,

$$\frac{(v_B^2 - u_x^2)^2}{u_x^2 v_B^2} \frac{u_x'^2}{\Omega^2} = \frac{2\chi_c}{v_B^2} - \frac{u_x^2}{v_B^2} + 2 \ln \left(\frac{-u_x}{\alpha u_{z\infty}} \right). \quad (5.67)$$

Note that (5.67) has the same form as (5.31), but with an additional constant of integration to be determined. The singularity in (5.67) at $u_x = -v_B$ implies that the system will reach the Bohm velocity with an infinite gradient at the Debye sheath entrance, $x = 0$ [31]. Hence, we expect that, to lowest order in α and τ , the distribution of the ion velocity normal to the wall at $x = 0$ is

$$f_{0x}(v_x) = \alpha n_\infty \delta(v_x + v_B), \quad (5.68)$$

shown as a vertical dashed line in the bottom-right panel of Figure 54.

5.3.3 Intermediate region ($x \sim x_c$)

The equations derived in the two previous subsections assumed that x was a point sufficiently far away from the critical point x_c . In what follows, I speculate that the self-consistent electrostatic potential must be a parabola in the region $x \sim x_c$, and also argue that my kinetic model requires non-zero τ (and therefore requires kinetic effects) in order to have a solution in this intermediate region. Figure 56 shows effective potentials corresponding to the solution of the fluid model (equation (5.36), valid for $\tau = 0$; for $\bar{x} = \bar{x}_c$ there is a large intermediate region near x_c where the effective potential is flat over a length scale of ρ_B , and this behaviour is connected with the electrostatic potential being close to parabolic for $x \sim x_c$.

The closed orbit and the open orbit equations both have the form

$$\frac{v_B^2}{\Omega^2} \frac{u_x'^2}{u_x^2} = C + 2 \ln \left(\frac{-u_x}{\alpha u_{z\infty}} \right), \quad (5.69)$$

when $\alpha \ll u_x/v_B \ll 1$ is taken. Suppose that equation (5.69) describes the dynamics in the region $x \sim x_c$. Using (4.88) to re-express (5.69) as a differential equation for the

electrostatic potential, one obtains

$$\rho_B \frac{e\phi'}{T_e} = \sqrt{C - \frac{2e\phi}{T_e}}. \quad (5.70)$$

The solution to equation (5.70) is the parabola

$$\frac{e\phi}{T_e} = \frac{1}{2}C - \frac{(x - x_0)^2}{2\rho_B^2}, \quad (5.71)$$

which can be re-expressed as

$$\frac{Ze\phi}{m_i} = \frac{1}{2}Cv_B^2 - \frac{1}{2}\Omega^2(x - x_0)^2. \quad (5.72)$$

The effective potential for ions reaching $x \sim x_c$ is thus

$$\chi(x; \bar{x}) = \frac{1}{2}\Omega^2(x - \bar{x})^2 - \frac{1}{2}\Omega^2(x - x_0)^2 + \frac{1}{2}Cv_B^2. \quad (5.73)$$

The effective potential of cold ions reaching x_c must be such that $\chi'(x; \bar{x}) = 0$ to lowest order in α and τ , because these ions are in closed orbits that eventually become open, and closed orbits satisfy $U_\perp = \chi_m(\bar{x})$ to lowest order in τ . Hence, $x_0 = \bar{x}$ and the effective potential is constant. The value of \bar{x} for which $\chi'(x_c; \bar{x}) = \chi''(x_c) = 0$ is \bar{x}_c , as proved in section 2.2.2. Hence, $x_0 = \bar{x}_c$ and the effective potential is equal to $\chi(x_c; \bar{x}_c) = \chi_c$ to lowest order in α and τ ,

$$\chi(x; \bar{x}) \simeq \frac{1}{2}Cv_B^2 = \chi_c. \quad (5.74)$$

From the closed orbit quasineutrality equation for $x \gg x_c$, $C = -v_B^2/u_{z\infty}^2 - 2$. Hence, $\chi_c = -v_B^2/u_{z\infty}^2 - 2$, and the open orbit solution for $x \ll x_c$ coincides with equation (5.31), which is the expansion of Chodura's differential equation for $u_x \sim v_B$.

Note that this discussion relies on the supposition that the solution be a parabola in the intermediate region. Moreover, the exact values of x_c and \bar{x}_c remain undetermined,

and depend on the higher order corrections to equation (5.69). Hence, the electrostatic potential solution in the intermediate region depends on higher order corrections in α and τ . My model is formulated to lowest order in α , and thus I expect that non-zero value of τ is required in order to obtain a solution in the intermediate region. Hence, my numerical scheme relies on the presence of kinetic effects, although it can be seen that my numerical solutions qualitatively approach the cold ion limit when τ is small.

In this subsection, I have speculated (without proof) that the form of the solution to the quasineutrality equation (4.9) in the intermediate region is a parabola when τ is small. I have thus argued that the electrostatic potential solution of (4.9) relies on $\tau \neq 0$, and is not necessarily equivalent to the electrostatic potential solution of the fluid model (valid for $\tau = 0$). Nonetheless, the numerical profiles for $\tau = 0.2$ approach the solutions for $\tau = 0$, lending support to the accuracy of the kinetic model in the intermediate region for small τ . Moreover, note that I have proved in 5.3.1 and 5.3.2 that the kinetic model recovers the correct ion flow profile — and electrostatic potential profile — for the regions $x \gg x_c$ and $x \ll x_c$. It is therefore unlikely that the flow and electrostatic potential in the intermediate region should tend to a profile that is too different from the fluid profile in the region $x \sim x_c$.

5.4 Infinite ion temperature limit

In the hot ion limit $\tau \rightarrow \infty$, the distribution function of equation (5.4) must have the value $r \rightarrow \infty$ in order to satisfy the marginal form of the kinetic Chodura condition (5.7), and therefore tends to a half-Maxwellian

$$F = 2n_\infty \left(\frac{m_i}{2\pi T_i} \right)^{3/2} \exp \left(-\frac{m_i U}{T_i} \right). \quad (5.75)$$

This distribution function was used in [33] to study a magnetic presheath where the electrons are cold. The limit $\tau \rightarrow \infty$ is inconsistent with the ordering (4.2) for finite values of m_i/m_e . The inconsistency arises because, at large values of τ , we would expect the sheath-presheath system to be ion-repelling. However, the system may stay electron-repelling if the value of m_i/m_e is sufficiently large that $\tau \ll \alpha^2 m_i/m_e$ can be satisfied. Therefore, the limit $1 \ll \tau \ll \alpha^2 m_i/m_e$ is not inconsistent (although it is unrealistic at large values of τ for typical values of m_i/m_e).

For $\tau \rightarrow \infty$, ion orbits are undistorted by the presheath potential drop necessary to repel most of the cold electrons. We expect $e\phi(x)/T_e \sim 1$, and therefore the ion flow and density can be computed using $e\phi(x)/T_i = (1/\tau)e\phi(x)/T_e = 0$ across the magnetic presheath. The effective potential is a parabola with its minimum at $x_m = \bar{x}$,

$$\chi(x, \bar{x}) = \frac{1}{2}\Omega^2 (x - \bar{x})^2. \quad (5.76)$$

This is a type I effective potential. Hence,

$$\chi_M(\bar{x}) = \chi(0, \bar{x}) = \frac{1}{2}\Omega^2 \bar{x}^2. \quad (5.77)$$

In chapter 4, I found that the self-consistent solution for the electrostatic potential leads to the presence of type II orbits only. Hence, for $\tau \rightarrow \infty$ there must be an infinitely small region near $x = 0$ in which the type II behaviour emerges. I neglect this region and proceed with the analysis. The minimum value of \bar{x} necessary for an ion at position x to be in a closed orbit or an open orbit is, using equations (3.19) and (3.25) with $\phi(x) = 0$,

$$\bar{x}_{m,o}(x) = \bar{x}_m(x) = \frac{1}{2}x. \quad (5.78)$$

Moreover, the adiabatic invariant is $\mu = U_\perp/\Omega$.

Inserting the distribution function (5.75) into equation (4.7), the closed orbit density is

$$n_{i,\text{cl}}(x) = 2n_\infty \left(\frac{m_i}{2\pi T_i} \right)^{3/2} \int_{x/2}^{\infty} \Omega d\bar{x} \int_{\frac{1}{2}\Omega^2 \bar{x}^2}^{\frac{1}{2}\Omega^2 (x-\bar{x})^2} \frac{2dU_\perp}{\sqrt{2(U_\perp - \chi(x))}} \int_{\Omega\mu}^{\infty} \frac{\exp\left(-\frac{m_i U}{T_i}\right) dU}{\sqrt{2(U - \Omega\mu)}}. \quad (5.79)$$

Changing variables to $\tilde{v}_y = (\bar{x} - x)/\rho_i$, $\tilde{U}_\perp = m_i(U_\perp - \frac{1}{2}\Omega^2(x - \bar{x})^2)/T_i$ and $\tilde{U} = m_i(U - \Omega\mu)/T_i$ gives

$$n_{i,\text{cl}}(x) = \frac{n_\infty}{\pi^{3/2}} \int_{-\frac{1}{2}\frac{x}{\rho_i}}^{\infty} d\tilde{v}_y \exp(-\tilde{v}_y^2) \int_0^{\frac{x}{\rho_i}(2\tilde{v}_y + \frac{x}{\rho_i})} \tilde{U}_\perp^{-1/2} \exp(-\tilde{U}_\perp) d\tilde{U}_\perp \times \int_0^{\infty} \tilde{U}^{-1/2} \exp(-\tilde{U}) d\tilde{U}. \quad (5.80)$$

Evaluating the integral over \tilde{U} and the integral over \tilde{U}_\perp leads to

$$n_{i,\text{cl}}(x) = \frac{n_\infty}{\sqrt{\pi}} \int_{-\frac{1}{2}\frac{x}{\rho_i}}^{\infty} \exp(-\tilde{v}_y^2) \operatorname{erf}\left(\sqrt{\frac{x}{\rho_i}\left(2\tilde{v}_y + \frac{x}{\rho_i}\right)}\right) d\tilde{v}_y. \quad (5.81)$$

The density of open orbits is given by

$$n_{i,\text{op}}(x) = \int_{\frac{1}{2}x}^{\infty} \Omega d\bar{x} \int_{\frac{1}{2}\Omega^2 \bar{x}^2}^{\infty} \frac{F(\mu, U)}{\sqrt{2(U - \chi_M)}} \times \left(\sqrt{2(\chi_M - \chi(x, \bar{x}) + \Delta_M)} - \sqrt{2(\chi_M - \chi(x, \bar{x}))} \right) dU. \quad (5.82)$$

The adiabatic invariant of ions with $U_\perp = \chi_M = \chi(0, \bar{x}) = \Omega^2 \bar{x}^2/2$ is given by

$$\mu = \frac{1}{2}\Omega \bar{x}^2. \quad (5.83)$$

Using equation (4.10), we obtain

$$\Delta_M = 2\alpha\pi\Omega\bar{x}\sqrt{2\left(U - \frac{1}{2}\Omega^2\bar{x}^2\right)}. \quad (5.84)$$

Then, using the dimensionless integration variables $\tilde{v}_z = \sqrt{m_i (U - \Omega^2 \bar{x}^2 / 2) / T_i}$ and $\tilde{\bar{x}} = \bar{x} / \rho_i$, equation (5.82) reduces to

$$n_{i,\text{op}}(x) = \frac{2}{\pi^{3/2}} \int_{\frac{x}{2\rho_i}}^{\infty} \exp(-\tilde{\bar{x}}^2) d\tilde{\bar{x}} \int_0^{\infty} \exp(-\tilde{v}_z^2) \times \left(\sqrt{\frac{x}{\rho_i} \left(2\tilde{\bar{x}} - \frac{x}{\rho_i} \right)} + 4\alpha\pi\tilde{\bar{x}}\tilde{v}_z - \sqrt{\frac{x}{\rho_i} \left(2\tilde{\bar{x}} - \frac{x}{\rho_i} \right)} \right) d\tilde{v}_z, \quad (5.85)$$

which does not simplify further for $x \neq 0$. At $x = 0$, equation (5.85) evaluates to

$$n_{i,\text{op}}(0) = n_{\infty} \frac{\Gamma^2(3/4)}{\pi} \sqrt{\alpha}. \quad (5.86)$$

The ion density profile in the hot ion limit is, according to (4.6) the sum of equations (5.81) and (5.85). The potential profile is obtained by imposing quasineutrality and inverting the Boltzmann relation for the electron density, to find

$$\frac{e\phi(x)}{T_e} = \ln \left(\frac{n_i(x)}{n_{\infty}} \right). \quad (5.87)$$

The potential drop across the magnetic presheath can be calculated by using $n_{i,\text{cl}}(0) = 0$ (from equation (5.81)) and equation (5.86),

$$\frac{e\phi(x)}{T_e} = \ln \left(\frac{\Gamma^2(3/4)}{\pi} \sqrt{\alpha} \right) \simeq \ln(0.48\sqrt{\alpha}). \quad (5.88)$$

Equation (5.88) is the dashed line marked $\tau = \infty$ in Figure 51. The electrostatic potential profile obtained using equation (5.87) is the red dashed curve (marked $\tau = \infty$) in Figure 52. The dashed curve in Figure 53 is obtained by inserting $\phi(x)$ into equation (4.88) for the ion fluid velocity u_x .

Inserting the distribution function (5.75) and the value of $\bar{x}_{\text{m},0}$ in (5.78) into equation (4.90), the distribution of the ion velocity component perpendicular to the wall at $x = 0$ is

$$f_{0x}(v_x) = \frac{n_{\infty}}{v_{ti}\pi} \Theta(v_x) \int_0^{\infty} \exp(-\tilde{\bar{x}}^2) \left[1 - \text{erf} \left(\frac{v_x^2}{4\pi\alpha\tilde{\bar{x}}v_{ti}^2} \right) \right] d\tilde{\bar{x}} \quad (5.89)$$

Inserting the distribution function (5.75) into equation (4.91), the distribution of the ion velocity components parallel to the wall at $x = 0$ is

$$f_{0yz}(v_y, v_z) = \frac{4\sqrt{\alpha}n_\infty}{\pi} \frac{\sqrt{v_y v_z}}{v_{t,i}^3} \exp\left(-\frac{v_y^2 + v_z^2}{v_{t,i}^2}\right) \Theta(v_y)\Theta(v_z). \quad (5.90)$$

Equation (5.89) is the dashed curve on the bottom-left panel in Figure 54, while equation (5.90) is the bottom right panel in Figure 55.

5.5 Discussion

In this chapter I have studied the dependence of an electron-repelling magnetic presheath on ion temperature using the kinetic model described in this thesis. The electrostatic potential drop across the magnetic presheath deviates from the fluid one $\tau = 0$ by up to approximately 15% for $\alpha/\sqrt{\tau} \gtrsim \sqrt{m_e/m_i} \sim 0.02$ (assuming Deuterium ions), a regime in which the wall is electron-repelling. For very large values of τ , the potential drop is up to a factor of 30% smaller than for $\tau = 0$, but the wall is likely to not be electron-repelling, which would change the potential. In order to study the transition between an electron- and an ion-repelling wall ($\alpha/\sqrt{\tau} \sim \sqrt{m_e/m_i}$), a kinetic treatment of both ions and electrons is essential.

I have argued that the numerical profiles of potential and fluid velocity obtained with the kinetic model are consistent with the small and large τ limit. The limit $\tau \ll 1$ is Chodura's fluid model. For $\tau \ll 1$, my kinetic treatment analytically recovers the potential drop predicted from fluid theory (equation (5.38)), and recovers the fluid potential and flow profiles for $x \gg x_c$ and for $x \ll x_c$. In the intermediate region $x \sim x_c$, I have speculated that the solution to my equations must become close to a parabola when τ is small, but have argued that τ must be non-zero in order to obtain a solution

to the kinetic model, and that such a solution may not be equal to the solution to the fluid model to lowest order in τ and α . The numerical results for $\tau = 0.2$, however, lend support to the view that the solution to the kinetic model approaches the solution to the fluid model when τ is small.

For large ion temperatures, $\tau \gtrsim 5$, the velocity component normal to the wall at the Debye sheath entrance is reduced by the small angle α for two reasons. Firstly, there are a large number of slow ions with $|v_x| \simeq v_B \ll v_{t,i}$, and secondly, the velocity spread of the distribution function is $\sqrt{\alpha}v_{t,i}$ (see Figure 54 and equation (5.89)). The tangential velocity of a typical ion remains roughly of the same size $v_y \sim v_z \sim v_{t,i}$, and therefore the angle between the ion trajectory and the wall is shallow at the Debye sheath entrance. There are several ions (in the peak of the distribution function f_{0x}) whose trajectory makes an angle with the wall of size $1/\sqrt{\tau}$. Most ions, in the tail of the distribution function, make an angle with the wall of size $\sqrt{\alpha}$. For $\tau \lesssim 1$, the typical size of all the velocity components is v_B and thus the angle between the ion trajectory and the wall is of order unity (for $\alpha = 0.05$ and $\tau = 0$ this angle is approximately 30°). Hence, an ion is expected to impinge on the wall at an angle whose size is small when $\tau \gg 1$ and order unity when $\tau \lesssim 1$.

It has been experimentally shown that $\tau \gtrsim 1$ near the divertor targets of tokamaks [65]. The kinetic treatment of this thesis has introduced the necessary ingredient to tackle the presence of ions at a temperature comparable to or larger than the electron temperature in the magnetic presheath. A kinetic treatment of the electrons will also be necessary to study systems in which $\alpha/\sqrt{\tau} \lesssim \sqrt{m_e/m_i}$.

CHAPTER 6

Conclusions

In this thesis I presented and solved a model of the magnetic presheath. The ordering (1.1) was used to assume that the magnetic presheath is collisionless and quasineutral. The ion trajectories were discussed in detail in chapter 2, where a treatment that relies on an asymptotic expansion in the small angle α between magnetic field and wall was presented. Weak turbulent gradients were assumed in the y direction perpendicular to the magnetic field and parallel to the wall. These gradients give rise to a turbulent electric field component which is smaller than the component normal to the wall by a factor $\delta \sim \alpha \ll 1$. Given an electrostatic potential profile $\phi(x, y)$, the ion density (3.13) is obtained in chapter 3. The density includes the contribution (3.24) of approximately closed orbits and the crucial contribution (3.39) of open orbits. The continuity equation is used to obtain the fluid velocity from the ion density via equation (4.87).

By making the simplifying assumption that the wall is strongly electron-repelling, in chapter 4 I have taken a Maxwell-Boltzmann response (4.3) for the electron density in the magnetic presheath. The self-consistent electrostatic potential is the solution of the quasineutrality equation (4.4). Taking $\delta = 0$ and thus assuming no gradients in

the directions parallel to the wall, the electrostatic potential that solves the simplified quasineutrality equation (4.9) can be determined by the iteration scheme presented in section 4.5. The ion distribution function at the magnetic presheath entrance was shown to have to satisfy a kinetic generalization of the Chodura condition, equation (4.28). The ion distribution function at the Debye sheath entrance is obtained from the analysis of chapter 3, and is given in equation (4.62). It is shown both analytically and numerically that this distribution function satisfies the kinetic Bohm condition.

The kinetic treatment of ions in the magnetic presheath is generalizable to an arbitrary number of ion species, and also applicable to impurities, and can thus be used to predict impurity trajectories and the effect of impurities. The ion distribution function (4.62) is important in order to predict the amount of sputtering off the wall, since each ion has a sputtering yield which depends on the ion's species, kinetic energy and angle of incidence with the surface [66]. Sputtering by impurities usually has a lower kinetic energy threshold than sputtering by the main ion species [67], and therefore it is especially important to predict the velocity distribution of impurities reaching the wall. In the limit of small impurity density, the impurity ions can be considered as a trace in the plasma and their distribution function at the Debye sheath entrance can be obtained from their distribution function at the magnetic presheath entrance.

The effect of finite ion temperature on an electron-repelling magnetic presheath was studied in chapter 5, where the distribution function at the magnetic presheath entrance was varied with the parameter $\tau = T_i/T_e$. The marginally satisfied kinetic Chodura condition (4.26) was assumed. All the numerical results were shown to be consistent with the zero and infinite ion temperature limits.

The inclusion of kinetic electrons is an important next step that must be taken to understand the physics of plasma-wall interaction near the divertor targets of a fusion de-

vice. Kinetic electrons are expected to change the behaviour of the magnetic presheath. Firstly, if the parameter $\alpha/\sqrt{\tau}$ is small enough, a strongly electron-repelling wall may not be a good approximation (see equation (4.2)). In this case, the number of electrons reaching the wall would be too large to ignore in the electron distribution, and an appropriate treatment of the whole electron distribution function would have to be retained. Plasma in contact with a wall that is not strongly electron-repelling can only be studied with a kinetic ion model such as the one described in this thesis. This is because fluid ion models can only be justified for zero ion temperature, and therefore are — from equation (4.2) — only consistent with an electron-repelling wall.

The ion kinetic treatment presented in this thesis is expected to be applicable to electrons in the Debye sheath if $\rho_e \sim \lambda_D$, a regime relevant for the boundary of fusion devices. Hence, an accurate and realistic solution of the Debye sheath and magnetic presheath with kinetic electrons may be obtained using the tools presented in this thesis. For $\alpha/\sqrt{\tau} \lesssim \sqrt{m_e/m_i}$ the inclusion of kinetic electrons is expected to dramatically change the potential drop across the sheath and presheath under ambipolar conditions, as well as the relationship between current and potential drop. With a full kinetic treatment, the ion and electron distribution functions at the wall could be obtained. The ion distribution function is important to predict sputtering off the wall, while the electron distribution function can be used to predict the amount of secondary electron emission.

In summary, this thesis has presented a powerful asymptotic theory of charged particle trajectories a gyroradius away from a wall, on which a uniform magnetic field impinges at a small angle α . Applying this theory to ions, a strongly electron-repelling magnetic presheath was solved for several values of α and for several values of the ratio of the ion and electron temperatures. The numerical solutions typically require less than one minute to compute on a laptop, making the numerical scheme described in

this thesis computationally cheap. The kinetic framework can be generalized to include multiple ion species and impurities, and can be applied to electrons in the Debye sheath. The numerical and analytical studies presented in this thesis generalize known magnetic presheath results, and demonstrate the potential applicability of the asymptotic theory to more complex problems such as a Debye sheath with $\rho_e \sim \lambda_D$, a magnetic presheath affected by turbulence ($\delta \sim \alpha$) and small angles ($\alpha \sim \sqrt{\tau m_e/m_i}$).

APPENDIX A

Typical widths of the plasma-wall boundary layers in a tokamak

In this Appendix, I estimate the typical typical width of the different plasma-wall boundary layers (see Figure 11). In order to do so, I take data from reference [54], which contains a comparison of some important parameters between different tokamaks. I use JET data because it is the most relevant for fusion. From Tables 1 to 5 of [54], the magnetic field is

$$B \sim 2 \text{ T}, \tag{A.1}$$

the electron and ion temperatures are (by taking $T_e \sim T_i \sim T$),

$$T \sim 50 \text{ eV} = 8 \times 10^{-18} \text{ J}, \tag{A.2}$$

and the electron density is,

$$n_e \sim 10^{19} \text{ m}^{-3}. \tag{A.3}$$

For a deuterium plasma, the ion mass is $m_i \sim 3 \times 10^{-27}$ kg, which leads to the estimate

$$v_{t,i} = \sqrt{\frac{2T_i}{m_i}} \sim 7 \times 10^4 \text{ ms}^{-1} \quad (\text{A.4})$$

for the ion thermal velocity. The ion gyrofrequency is estimated to be

$$\Omega = \frac{eB}{m_i} \sim 10^8 \text{ s}^{-1}, \quad (\text{A.5})$$

which leads to the estimate for the ion gyroradius

$$\rho_i \sim \frac{v_{t,i}}{\Omega} \sim 7 \times 10^{-4} \text{ m} = 0.7 \text{ mm}. \quad (\text{A.6})$$

The Debye length is (with $\epsilon_0 = 8.85 \times 10^{-12} \text{ Fm}^{-1}$)

$$\lambda_D = \sqrt{\frac{\epsilon_0 T_e}{n_e e^2}} \sim 2 \times 10^{-5} \text{ m} = 0.02 \text{ mm}. \quad (\text{A.7})$$

The ion mean free path is estimated for the two dominant collision processes occurring close to the divertor target: Coulomb collisions and charge exchange. For Coulomb collisions, I determine the frequency of ion-ion collisions as (from the NRL Plasma Formulary [68])

$$\nu_{ii} \sim \frac{4\sqrt{\pi}}{3} \frac{e^4 n_i \ln \Lambda}{(4\pi\epsilon_0)^2 m_i^{1/2} T_i^{3/2}} \sim 2 \times 10^4 \text{ s}^{-1}, \quad (\text{A.8})$$

where $\ln \Lambda \sim 15$ is the Coulomb logarithm for ion-ion collisions. Therefore, the collisional mean free path is

$$\lambda_{\text{mfp},ii} \sim \frac{v_{t,i}}{\nu_{ii}} \sim 4 \text{ m}. \quad (\text{A.9})$$

I evaluate $\alpha \lambda_{\text{mfp},ii}$ for $\alpha \sim 0.1$ to obtain

$$\alpha \lambda_{\text{mfp},ii} \sim 0.4 \text{ m}. \quad (\text{A.10})$$

For charge exchange I use the value of $5 \times 10^{-14} \text{ m}^3 \text{s}^{-1}$ (extracted from reference [69]) as an approximate rate coefficient for the reaction at $T_i \sim 50 \text{ eV}$. I then multiply this by an estimate of the neutral density, $n_n \sim 10^{18} \text{ m}^{-3}$, in order to obtain the charge exchange collision frequency

$$\nu_{\text{cx}} \sim 5 \times 10^4 \text{ s}^{-1}. \quad (\text{A.11})$$

From this collision frequency, we obtain a mean free path that is slightly smaller than the Coulomb collision one,

$$\lambda_{\text{mfp,cx}} \sim 1 \text{ m}. \quad (\text{A.12})$$

The estimate for the width of the collisional layer becomes

$$\alpha \lambda_{\text{mfp,cx}} \sim 0.1 \text{ m}. \quad (\text{A.13})$$

It is worth making a few comments on these numbers and the scalings associated with them. The scaling $\rho_i / \lambda_D \sim 40 \gg 1$ which implies a quasineutral magnetic presheath is robust. The dependence on density and temperature of the ion gyroradius and Debye length is weak, with $\rho_i \propto \sqrt{T_i}$ and $\lambda_D \propto \sqrt{T_e / n_e}$, so the error associated with both these estimates is small. If one of T_i , T_e or n_e is wrong by a factor of 10, the corresponding estimate for ρ_i or λ_D will be wrong by a factor of ~ 3 only.

The discussion about the length of the collisional layer is more complex. I assumed Coulomb or charge exchange collisions in order to make the estimates (A.9) and (A.12), which resulted in $\alpha \lambda_{\text{mfp}} / \rho_i \sim 100 \gg 1$ using the slightly more conservative charge exchange estimate. This seems to favour a collisionless model for the magnetic presheath and a scale separation between the magnetic and collisional layers. However, note that $\lambda_{\text{mfp,ii}} \propto T_i^2$, so that if the ion temperature were smaller than the estimated temperature

by a factor of 10, this separation of scales would no longer be valid due to collisions becoming important in the magnetic presheath. Moreover, the charge exchange frequency depends linearly on the neutral density close to divertor targets, which we estimated crudely. These estimates warrant caution towards the idea of a completely collisionless magnetic presheath and the separation into the three layers of Figure 11, even though it is still a physically motivated and theoretically attractive way to model the plasma-wall boundary.

APPENDIX B

Orderings in the context of a tokamak

The orderings I used for the length scales parallel to the wall in the magnetic presheath and the characteristic timescale are applicable to tokamaks, as I show in this Appendix. Figure B1 shows the plasma-wall boundary in the context of the tokamak geometry. In Appendix B.1, I recover the orderings (2.6) and (2.11) of Section 2 by developing an ordering for the turbulent structures in the SOL. In Appendix B.2, I calculate the characteristic steady-state gradients parallel to the wall in the magnetic presheath by projecting the SOL width onto the y and z directions parallel to the wall. The steady-state lengths are longer than, or of the same order as, the characteristic lengths parallel to the wall due to turbulent structures, as expected.

B.1 Turbulence

The size of the turbulent structures is assumed of order $l \sim \rho_i/\delta$ in any direction perpendicular to field lines, with $\delta \ll 1$. I proceed to estimate the parallel length l_{\parallel} and turnover time t_{turn} associated with such structures. In the perpendicular direction,

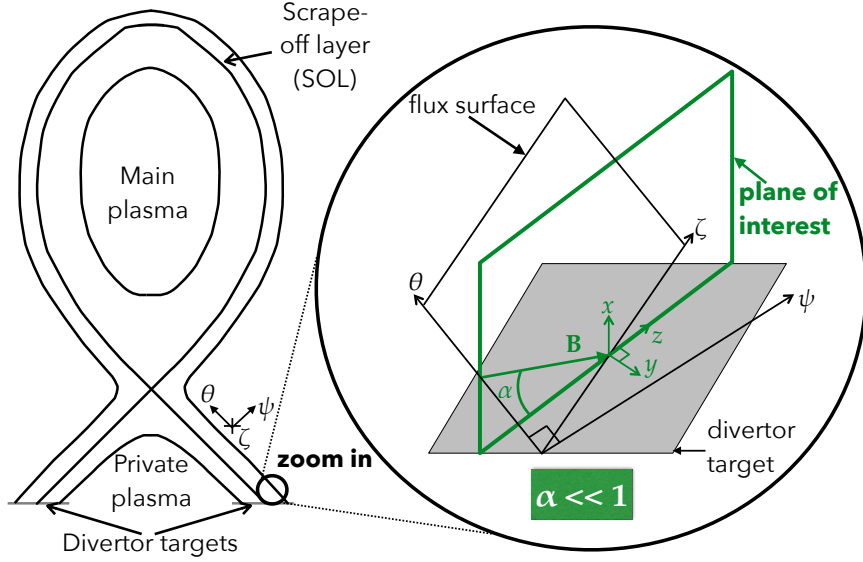


Figure B1: On the left, a cartoon of the flux surface contours in the poloidal plane of a typical tokamak, with different plasma regions labelled. The region close to one of the two divertor targets (grey horizontal lines) is enlarged and shown in 3 dimensions on the right. Here, the cartesian coordinate axes (x, y, z) used as a basis in this thesis are shown in green. The divertor target (also referred to as the wall) is the grey surface S , and two planes are shown cutting through it: the flux surface containing the field line \mathbf{B} (green arrow) and the toroidal direction ζ , and the plane perpendicular to y (framed in green) containing the field line and the normal to the wall. In both drawings we have identified, in the region near the divertor target, the local poloidal and toroidal axes θ and ζ respectively, and the axis locally normal to the flux surface ψ . On the right, we have labelled the minimum angle α between the field and the wall.

over a characteristic turbulent timescale, I assumed that plasma travels a distance l . The distance it travels in the parallel direction is larger than l by the factor by which the typical velocity along the field line, the thermal velocity $v_{t,i}$, is larger than the cross-field one. I order the cross-field velocity of plasma in the SOL the same as the $\mathbf{E} \times \mathbf{B}$ drift I expect turbulence to produce, $\sim \delta v_{t,i}$. I can thus assume that turbulent structures have a size $l_{\parallel} = l/\delta$ parallel to the magnetic field.

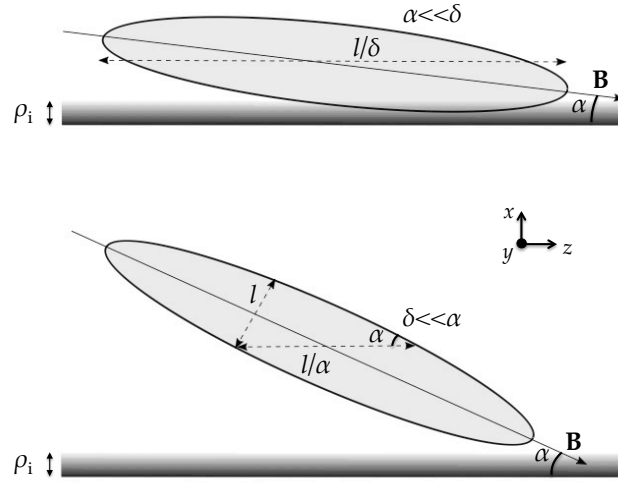


Figure B2: Turbulent structures in the SOL, as they approach the magnetic presheath (thin shaded region of thickness $\sim \rho_i$), are shown here. The elongation of these structures is by a factor $1/\delta$, which comes from the characteristic size of perpendicular velocities compared to parallel ones. Two cases (i) $\alpha \ll \delta$ and (ii) $\delta \ll \alpha$ are shown. In (i), the size of the turbulent structure in the z direction is determined by the length of the turbulent structure parallel to the field line, l/δ . In (ii), it is determined by the length of a cut across the eddy, l/α .

I refer to turbulent scale lengths in the z direction as l_z . For $\alpha \ll \delta$, it should be clear from Figure B2 that gradients in the z -direction in the magnetic presheath, arising due to the turbulent structures impinging on the wall, are set by l/δ , so that $l/l_z \sim \delta$. On the other hand, when $\delta \ll \alpha$ the length scale in the z -direction is set by the horizontal cut across the eddy shown in the lower picture, of length l/α , so that $l/l_z \sim \alpha$. Therefore, $l_z \sim \min(l/\alpha, l/\delta)$. By ordering $z \sim l_z$, I obtain the ordering of (2.6).

The turnover time of turbulence is obtained from the characteristic length and velocity scales associated with the turbulence, $t_{\text{turn}} \sim l/\delta v_{t,i} \sim 1/\delta^2 \Omega$. This leads to an estimate for the characteristic frequency of changes within turbulent structures, using $\partial/\partial t \sim 1/t_{\text{turn}}$, from which the ordering of (2.11) follows.

The gradients in the x direction outside of the magnetic presheath are determined by the cross-field size l of turbulent structures, but they get larger as the magnetic presheath is approached (its characteristic thickness is ρ_i). Pictorially, this can be viewed as a squeezing that the turbulent structures undergo in the direction normal to the wall as they approach it. However, the discussion on the characteristic lengths *parallel to the wall* in the magnetic presheath is unaffected, because these scales are inherited from the boundary conditions at the magnetic presheath entrance ($x \rightarrow \infty$).

B.2 Steady-state scrape-off layer width

One expects gradients in the y and z directions due to the steady-state SOL width because the flux coordinate direction ψ has components in the y and z directions (see Figure B3).¹ Note that, in a typical tokamak, the SOL width λ_{SOL} is of the order of the width of turbulent structures, $\lambda_{\text{SOL}} \sim l \sim 10$ mm [52]. One can calculate the projection in the y and z directions of the SOL width, and thus obtain an estimate for the characteristic steady-state scale lengths in those directions, L_y and L_z . These must be greater than or equal to the turbulent scales in those directions, $L_y \gtrsim l$ and $L_z \gtrsim l_z \sim \min(l/\alpha, l/\delta)$.

In Figure B3, the angle ε is related to the ratio of the poloidal component of the magnetic field to the toroidal component of the magnetic field, $\tan \varepsilon = |B_\theta/B_\zeta|$. The ratio B_θ/B_ζ is usually small in tokamaks, so $\varepsilon \ll 1$. The angle γ is the angle between the flux surface and the divertor target. From Figure B3, I obtain an expression relating

¹The x direction also has a component in the ψ direction, but the scale of the SOL width λ_{SOL} is large compared to the magnetic presheath scale ρ_i , so this does not matter.

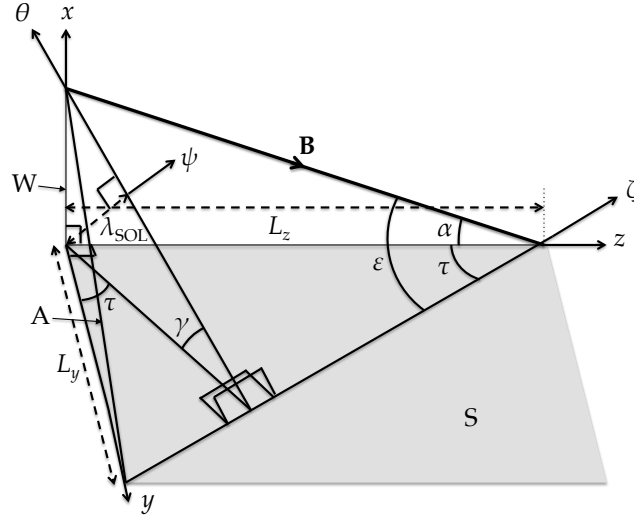


Figure B3: A schematic that shows how the SOL thickness λ_{SOL} , measured in the flux coordinate direction ψ , is projected to lengths L_y and L_z in the directions parallel to the wall. The plane A is the flux surface, W is the plane perpendicular to y (framed green in Figure B1) and S is the divertor target. The following angles are shown: γ , the angle between the flux surface A and the divertor target S; ε , the angle between the toroidal direction ζ and the magnetic field line \mathbf{B} ; τ , the angle between the z and ζ directions.

α to ε and γ ,

$$\sin \alpha = \sin \varepsilon \sin \gamma. \quad (\text{B.1})$$

In order to achieve $\alpha \ll 1$ it is sufficient to have $\varepsilon \ll 1$, which is valid for most tokamaks. However, the divertor target inclination in the poloidal plane is a free design parameter, and the flux surface geometry can be controlled with the external magnets. Therefore, the angle γ between the divertor target and the flux surface is often also made small, $\gamma \lesssim 1$, in order to make α even smaller. I order α with respect to ε as $\alpha \lesssim \varepsilon$.

In what follows, it will be convenient to use the angle τ , shown in Figure B3. I express τ in terms of ε and γ ,

$$\tan \tau = \tan \varepsilon \cos \gamma. \quad (\text{B.2})$$

I proceed to express the length scales L_y and L_z in terms of the SOL width λ_{SOL} and the angles ε and γ . Projecting the SOL width λ_{SOL} onto the z -axis and using (B.2), I obtain

$$L_z = \frac{\lambda_{\text{SOL}}}{\sin \gamma \sin \tau} = \frac{\sqrt{1 + \tan^2 \varepsilon \cos^2 \gamma}}{\sin \gamma \cos \gamma \tan \varepsilon} \lambda_{\text{SOL}} \sim \frac{1}{\varepsilon \sin \gamma} \lambda_{\text{SOL}} \gg \lambda_{\text{SOL}}. \quad (\text{B.3})$$

The presence of $\sin \gamma$ in the denominator of (B.3) implies that $L_z \sim \lambda_{\text{SOL}}/\alpha \gtrsim l_z \sim \min(l/\alpha, l/\delta)$. The SOL width projected in the y direction is, using (B.2),

$$L_y = \frac{\lambda_{\text{SOL}}}{\cos \tau \sin \gamma} = \frac{\sqrt{1 + \tan^2 \varepsilon \cos^2 \gamma}}{\sin \gamma} \lambda_{\text{SOL}} \sim \frac{\lambda_{\text{SOL}}}{\sin \gamma} \gtrsim \lambda_{\text{SOL}}. \quad (\text{B.4})$$

This also implies $L_y \gtrsim l$. The ratio of the two steady-state length scales is

$$\frac{L_y}{L_z} = \tan \varepsilon \cos \gamma \sim \varepsilon. \quad (\text{B.5})$$

This means that L_z is much larger than L_y , by a factor $\sim 1/\varepsilon$.

APPENDIX C

How large can the parallel current be?

In this appendix, I consider the validity of our equations when a large current \mathbf{j}^L is driven parallel to the magnetic field through the plasma in the magnetic presheath. In Section 2, I ordered the plasma currents using the particle drifts, and the relationship between current components obtained using Maxwell's equations. This means that the ordering I obtained there, $j_z^D \sim \alpha n_i e v_{ti} \sim \delta n_i e v_{ti}$ is consistent with the piece of the parallel current that flows through the plasma in response to the currents due to the perpendicular drifts. This parallel current is present to satisfy $\nabla \cdot \mathbf{j}^D = 0$ and maintain charge neutrality, that may otherwise be broken by the divergence of the perpendicular current. In this Appendix, I show that that the orderings are consistent with a larger parallel current, $j^L \gg \delta n_i v_{ti}$, provided that the size of this current does not become too large, at which point neglecting the plasma produced magnetic fields and the induced electric fields would no longer be a valid assumption.

The large parallel current \mathbf{j}^L has components $j_z^L = j^L \cos \alpha \sim j^L$, $j_x^L = -j^L \sin \alpha \sim \alpha j^L$ and $j_y^L = 0$. This parallel current must satisfy $\nabla \cdot \mathbf{j}^L = 0$. Using (2.6) I find $\partial j_x^L / \partial x \sim \alpha j^L / \rho_i$ and $\partial j_z^L / \partial z \sim \delta \alpha j^L / \rho_i \sim \delta^2 j^L / \rho_i$. Thus, $\nabla \cdot \mathbf{j}^L = 0$ requires $\partial j^L / \partial x = 0$, and to

lowest order \mathbf{j}^L is not affected by the magnetic presheath. Therefore, the length scale in the x direction of the large parallel current and the magnetic and electric fields associated with it is larger than the magnetic presheath scale ρ_i . Balancing $\partial j_x^L / \partial x \sim \partial j_z^L / \partial z$ leads to ordering

$$\frac{\partial}{\partial x} \sim \frac{\delta}{\alpha l} \sim \frac{1}{l}, \quad (\text{C.1})$$

so the appropriate length scale in the x direction (for this Appendix only) is the perpendicular turbulent scale l .

The magnetic field produced in the plasma by \mathbf{j}^L is denoted $\mathbf{B}^{p'}$ and is determined by Ampère's law (2.14), with \mathbf{j}^L instead of \mathbf{j}^D and $\mathbf{B}^{p'}$ instead of \mathbf{B}^p . Taking the y component of (2.14) with $j_y^L = 0$, I have $\partial B_z^{p'} / \partial x \sim \partial B_x^{p'} / \partial z$, from which I obtain $B_z^{p'} \sim \alpha B_x^{p'}$. Considering the long length scales in the z direction, this implies that $\partial B_z^{p'} / \partial z$ must be subdominant in $\nabla \cdot \mathbf{B}^{p'} = 0$, so $\partial B_x^{p'} / \partial x \sim \partial B_y^{p'} / \partial y$. This implies that $B_x^{p'} \sim B_y^{p'}$. The x and z components of Ampère's law determine $B_y^{p'} \sim B_x^{p'} \sim \mu_0 l j^L$. Collecting the orderings for the components of the magnetic field produced by a large parallel current \mathbf{j}_L , I have

$$B_z^{p'} \sim \alpha B^{p'} \ll B_x^{p'} \sim B_y^{p'} \sim B^{p'} \sim \mu_0 l j^L \sim \frac{j^L}{\delta e n_i v_{ti}} \beta B^c, \quad (\text{C.2})$$

where in the rightmost equation I used $\beta B^c \sim B^p \sim \mu_0 l \delta n_i e v_{ti}$ inferred from (2.15) and (2.16).

As explained in section 2.1, in order to neglect $\mathbf{B}^{p'}$, I require each component of it to be negligible compared to either the respective component or the smallest retained component of the constant external magnetic field \mathbf{B}^c . The strongest constraint is obtained by the neglect of $B_x^{p'}$ and $B_y^{p'}$ compared to $B_x^c \sim \alpha B^c$. This is $B^{p'} \ll \alpha B^c$, which

leads to

$$j^L \ll \frac{\alpha}{\beta} \delta e n_i v_{t,i}. \quad (\text{C.3})$$

The large parallel current \mathbf{j}^L is consistent with an electrostatic electric field provided that each component of the electric field $\mathbf{E}^{p'}$ induced by $\mathbf{B}^{p'}$ is negligible compared to either the same component or the smallest retained component of $-\nabla\phi$. From (2.11), (C.2) and the length scale orderings of this section (which are $x \sim y \sim l \ll z \sim l/\delta \sim l/\alpha$), one can order the components of the induction equation (2.17), with $\mathbf{E}^{p'}$ instead of \mathbf{E}^p and $\mathbf{B}^{p'}$ instead of \mathbf{B}^p . I obtain (recalling that $\rho_i \Omega = v_{t,i}$)

$$E_x^{p'} \sim E_y^{p'} \sim \alpha E^{p'} \ll E_z^{p'} \sim E^{p'} \sim \delta v_{t,i} B^{p'}. \quad (\text{C.4})$$

Therefore, I find that the strongest constraint on the electrostatic approximation is $E_z^{p'} \sim \delta v_{t,i} B^{p'} \ll \delta v_{t,i} B^c$ and leads to $B^{p'} \ll B^c$. This is a weaker condition than the one needed to neglect the magnetic field $\mathbf{B}^{p'}$; hence, the electrostatic approximation is justified when (C.3) holds. Note that (C.3) allows for a large parallel current in the magnetic presheath because $\alpha \gg \beta$, as pointed out in Section 2. If currents larger than (C.3) were present in the magnetic presheath, one would have to consider the magnetic fields produced by them in our equations (and in extreme cases also the induced electric fields). For example, currents larger than (C.3) would be large enough to change the angle α between the magnetic field lines and the wall.

APPENDIX D

Adiabatic invariant

I proceed to prove that the lowest order adiabatic invariant has the form in (2.55), starting from the definition

$$\mu = \frac{1}{2\pi m_i} \oint \tilde{\mathbf{p}} \cdot d\tilde{\mathbf{r}}, \quad (\text{D.1})$$

where $\tilde{\mathbf{p}}$ and $\tilde{\mathbf{r}} = (\tilde{x}, \tilde{y}, \tilde{z})$ are the canonical momentum and the position vector of the charged particle in the system where $\alpha = \delta = 0$ and in the frame where the parallel motion and $\mathbf{E} \times \mathbf{B}$ drift of an ion are zero. The electric field in this frame is given by $\tilde{\mathbf{E}} = \mathbf{E} - \langle \mathbf{E} \rangle_\varphi$, whereas the magnetic field is unchanged provided we are in the non-relativistic limit.

From (2.63), the magnetic vector potential can be expressed as (using $\alpha = 0$).

$$\mathbf{A} = \begin{pmatrix} 0 \\ \tilde{x}B \\ 0 \end{pmatrix}. \quad (\text{D.2})$$

The canonical momentum is $\tilde{\mathbf{p}} = m_i \tilde{\mathbf{v}} + Ze\mathbf{A}$, where $\tilde{\mathbf{v}} = \mathbf{v} - \langle \mathbf{v} \rangle_\varphi$. Using (2.31) and (2.43), the component v_x of the velocity gyroaverages to zero. The gyroaverage of v_y is

(2.44) and the gyroaverage of v_z is (2.34), leading to

$$\langle \mathbf{v} \rangle_\varphi = \begin{pmatrix} 0 \\ V_{\mathbf{E} \times \mathbf{B}}(\bar{x}, U_\perp) \\ \sigma_\parallel V_\parallel(U_\perp, U) \end{pmatrix}. \quad (\text{D.3})$$

Note that there is no periodicity in the z direction, and thus $\tilde{v}_z = 0$. The position $\tilde{\mathbf{r}}$ is obtained by integrating $\tilde{\mathbf{v}}$ in time (which, due to periodicity, is equivalent to integrating in gyrophase and dividing by $\overline{\Omega}$). For simplicity, I choose $\tilde{\mathbf{r}}$ such that $\langle \tilde{\mathbf{r}} \rangle_\varphi = 0$. Using $d\tilde{\mathbf{r}} = \tilde{\mathbf{v}} d\varphi / \overline{\Omega}$, the expression for the adiabatic invariant in (D.1) becomes

$$\mu = \frac{1}{2\pi\overline{\Omega}} \oint (\tilde{v}^2 + \Omega \tilde{x} \tilde{v}_y) d\varphi. \quad (\text{D.4})$$

From (2.33) I obtain $\tilde{x} = -\tilde{v}_y / \Omega$ which leads to (using $\tilde{v}_x = v_x$ and $\tilde{v}_z = 0$)

$$\mu = \frac{1}{2\pi\overline{\Omega}} \oint v_x^2 d\varphi. \quad (\text{D.5})$$

Using (2.31) and the definition of the gyroaverage in (2.43), equation (D.5) reduces to the form in (2.55).

APPENDIX E

Ion density at the magnetic presheath entrance

Here I derive equation (4.17) in the following steps. First, in section E.1, I expand the adiabatic invariant (2.55) as a function of \bar{x} and U_\perp for small electrostatic potential, $e\phi(x)/T_e \ll 1$, and small gradients of the electrostatic potential, $\epsilon = \rho_i \phi'(x)/\phi(x) \ll 1$. Then, in section E.2 I expand equation (2.41) to obtain an expression for \bar{x} as a function of φ , x and μ . I also obtain an expression for U_\perp as a function of φ , x and μ . Then, by making the change of variables $(x, \bar{x}, U_\perp, U) \rightarrow (x, \varphi, \mu, U)$, I obtain an expression for the ion density in section E.3. Finally, this expression for the ion density is carefully expanded in section E.4. The results of this appendix are valid to lowest order in α .

E.1 Adiabatic invariant expansion

I proceed to derive an expression for μ as a function of \bar{x} and U_\perp by expanding equation (2.55) near $x \rightarrow \infty$, where $e\phi(x)/T_e \ll 1$. In addition, I assume that the length

scale of changes in the electrostatic potential is much larger than the ion gyroradius ρ_i , defining the small parameter ϵ of equation (4.15). I first expand the expression inside the square root of equation (2.31) around $x = \bar{x}$ to second order in ϵ , obtaining

$$v_x = \sigma_x V_x(x, \bar{x}, U_\perp) = \sigma_x \sqrt{2} \left[U_\perp - \frac{1}{2} \Omega^2 (x - \bar{x})^2 - \frac{\Omega \phi(\bar{x})}{B} - \frac{\Omega \phi'(\bar{x})}{B} (x - \bar{x}) - \frac{\Omega \phi''(\bar{x})}{2B} (x - \bar{x})^2 + O(\epsilon^3 \hat{\phi} v_{ti}^2) \right]^{1/2}. \quad (\text{E.1})$$

Completing the square in the square root and dropping small terms gives

$$V_x(x, \bar{x}, U_\perp) = A \Omega \sqrt{1 + \frac{\phi''(\bar{x})}{\Omega B}} \times \sqrt{1 - \frac{1}{A^2} \left[x - \bar{x} + \frac{\phi'(\bar{x})}{\Omega B} \right]^2} + O(\hat{\phi} \epsilon^3, \hat{\phi}^2 \epsilon^2), \quad (\text{E.2})$$

where I have defined the orbit amplitude

$$A = \frac{1}{\Omega} \left(1 + \frac{\phi''(\bar{x})}{\Omega B} \right)^{-1/2} \sqrt{2U_\perp - \frac{2\Omega \phi(\bar{x})}{B}}. \quad (\text{E.3})$$

The bounce points of the closed orbit are obtained by solving $V_x(x, \bar{x}, U_\perp) = 0$, leading to

$$x_b = \bar{x} - \frac{\phi'(\bar{x})}{\Omega B} - A, \quad (\text{E.4})$$

$$x_t = \bar{x} - \frac{\phi'(\bar{x})}{\Omega B} + A. \quad (\text{E.5})$$

By substituting (E.2) into equation (2.40) and using (E.4) and (E.5) for the integration limits, I find

$$\begin{aligned} \frac{\pi}{\Omega} &= \int_{x_b}^{x_t} \left(A \Omega \sqrt{1 + \frac{\phi''(\bar{x})}{\Omega B}} \sqrt{1 - \frac{1}{A^2} \left[x - \bar{x} + \frac{\phi'(\bar{x})}{\Omega B} \right]^2} \right)^{-1} dx \\ &+ O\left(\frac{\hat{\phi} \epsilon^3}{\Omega}, \frac{\hat{\phi}^2 \epsilon^2}{\Omega}\right), \end{aligned} \quad (\text{E.6})$$

which leads to the modified gyrofrequency

$$\bar{\Omega} = \Omega \sqrt{1 + \frac{\phi''(\bar{x})}{\Omega B}} + O\left(\hat{\phi}\epsilon^3\Omega, \hat{\phi}^2\epsilon^2\Omega\right) = \Omega \left(1 + \frac{\phi''(\bar{x})}{2\Omega B} + O\left(\hat{\phi}\epsilon^3, \hat{\phi}^2\epsilon^2\right)\right). \quad (\text{E.7})$$

We exploit (E.7) to simplify equation (E.2),

$$V_x(x, \bar{x}, U_\perp) = \bar{\Omega} A \sqrt{1 - \frac{1}{A^2} \left[x - \bar{x} + \frac{\phi'(\bar{x})}{\Omega B}\right]^2} + O\left(\hat{\phi}\epsilon^3, \hat{\phi}^2\epsilon^2\right). \quad (\text{E.8})$$

By inserting (E.8) into expression (2.55) for the adiabatic invariant, I find

$$\mu = \frac{1}{\pi} \int_{x_b}^{x_t} \bar{\Omega} A \sqrt{1 - \frac{1}{A^2} \left[x - \bar{x} + \frac{\phi'(\bar{x})}{\Omega B}\right]^2} dx + O\left(\hat{\phi}\epsilon^3 \frac{v_{ti}^2}{\Omega}, \hat{\phi}^2\epsilon^2 \frac{v_{ti}^2}{\Omega}\right), \quad (\text{E.9})$$

which evaluates to

$$\begin{aligned} \mu &= \frac{1}{2} \bar{\Omega} A^2 + O\left(\hat{\phi}\epsilon^3 \rho_i v_{ti}, \hat{\phi}^2\epsilon^2 \rho_i v_{ti}\right) \\ &= \frac{1}{\bar{\Omega}} \left(U_\perp - \frac{\Omega \phi(\bar{x})}{B}\right) + O\left(\hat{\phi}\epsilon^3 \rho_i v_{ti}, \hat{\phi}^2\epsilon^2 \rho_i v_{ti}\right). \end{aligned} \quad (\text{E.10})$$

Rearranging equation (E.10) and using (E.7), I obtain

$$\begin{aligned} U_\perp &= \bar{\Omega} \mu + \frac{\Omega \phi(\bar{x})}{B} + O\left(\hat{\phi}\epsilon^3 \frac{v_{ti}^2}{\Omega}, \hat{\phi}^2\epsilon^2 \frac{v_{ti}^2}{\Omega}\right) \\ &= \Omega \mu + \frac{\Omega \phi(\bar{x})}{B} + \frac{\mu \phi''(\bar{x})}{2B} + O\left(\hat{\phi}\epsilon^3 \frac{v_{ti}^2}{\Omega}, \hat{\phi}^2\epsilon^2 \frac{v_{ti}^2}{\Omega}\right). \end{aligned} \quad (\text{E.11})$$

At $x \rightarrow \infty$, the zeroth order in $\hat{\phi}$ of all the equations in this Appendix is valid exactly. Then, I have $\bar{\Omega} = \Omega$ from equation (E.7) and $\mu = U_\perp/\Omega$ from equation (E.10). Hence, the equations $2\Omega\mu = v_x^2 + v_y^2$ and $2(U - \Omega\mu) = v_z^2$ are valid at $x \rightarrow \infty$. These equations are used to obtain equation (4.27) and to obtain $F_{cl}(\mu, U)$ from $f_\infty(\mathbf{v})$.

E.2 Gyrophase expansion

I require an expression for U_\perp as a function of μ , φ and x . To obtain it from equation (E.11), I need an equation for \bar{x} as a function of μ , φ and x , which I proceed to derive. I

insert equation (E.8) into the definition of the gyrophase φ , equation (2.41), and use the top bounce point in (E.5) as the lower integration limit to obtain

$$\varphi = \sigma_x \int_{x_t}^x \left(A \sqrt{1 - \frac{1}{A^2} \left[s - \bar{x} + \frac{\phi'(\bar{x})}{\Omega B} \right]^2} \right)^{-1} ds + O\left(\hat{\phi}\epsilon^3, \hat{\phi}^2\epsilon^2\right). \quad (\text{E.12})$$

Note that $\varphi > 0$ when $\sigma_x = -1$. Using equation (E.12) and $A = \sqrt{2\mu/\Omega}$ (from equation (E.10)), I obtain the relation

$$x - \bar{x} + \frac{\phi'(\bar{x})}{\Omega B} = \sqrt{\frac{2\mu}{\Omega}} \cos \varphi + O\left(\hat{\phi}\epsilon^3\rho_i, \hat{\phi}^2\epsilon^2\rho_i\right). \quad (\text{E.13})$$

Then, we expand equation (E.13) around the lowest order $\bar{x} = x - \sqrt{2\mu/\Omega} \cos \varphi$ to obtain

$$\bar{x} = x - \left(1 + \frac{3\Omega\phi''(x)}{4B}\right) \sqrt{\frac{2\mu}{\Omega}} \cos \varphi + \frac{\phi'(x)}{\Omega B} + O\left(\hat{\phi}\epsilon^3\rho_i, \hat{\phi}^2\epsilon^2\rho_i\right). \quad (\text{E.14})$$

Similarly, I expand equation (E.11) around $\bar{x} = x - \sqrt{2\mu/\Omega} \cos \varphi$ to obtain

$$\begin{aligned} U_{\perp} = \Omega\mu + \frac{\Omega\phi(x)}{B} - \frac{\Omega\phi'(x)}{B} \sqrt{\frac{2\mu}{\Omega}} \cos \varphi + \frac{\mu\phi''(x)}{2B} (1 + 2\cos^2 \varphi) \\ + O\left(\hat{\phi}\epsilon^3v_{ti}^2, \hat{\phi}^2\epsilon^2v_{ti}^2\right). \end{aligned} \quad (\text{E.15})$$

Defining $\delta U_{\perp} = \Omega\mu - U_{\perp}$, equation (E.15) leads to equation (4.18).

E.3 Change of variables in the ion density integral

For sufficiently large x , the open orbit density is zero and the closed orbit density in (4.7) is

$$n_{i,cl}(x) \simeq \int_{\bar{x}_m(x)}^{\infty} \Omega d\bar{x} \int_{\chi(x,\bar{x})}^{\chi_M(\bar{x})} \frac{2dU_{\perp}}{\sqrt{2(U_{\perp} - \chi(x,\bar{x}))}} \int_{U_{\perp}}^{\infty} \frac{F_{cl}(\mu(\bar{x}, U_{\perp}), U)}{\sqrt{2(U - U_{\perp})}} dU. \quad (\text{E.16})$$

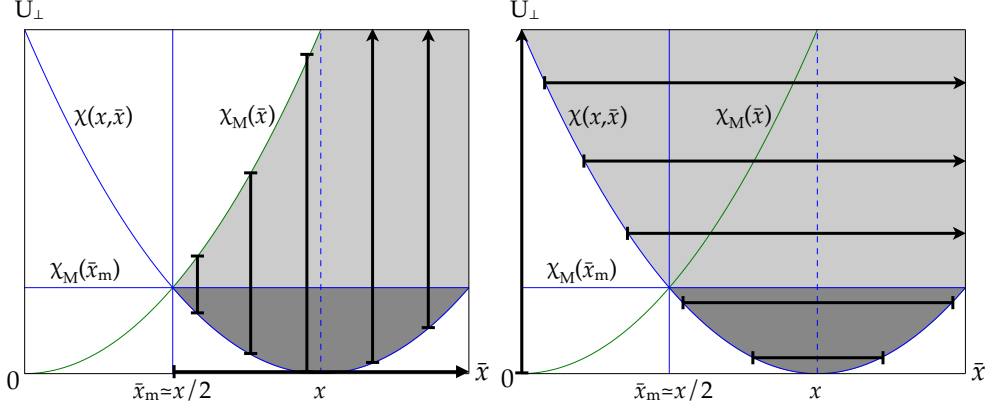


Figure E1: The integration domain in (\bar{x}, U_{\perp}) of equation (E.16) consists of both shaded regions on the left hand side drawing. When I exchange the integration order, the integration limits (bold lines) are picked such that the integration domain coincides in the dark grey region but not in the light grey one. The light grey region satisfies $U_{\perp} > \chi_M(x/2) = \Omega^2 x^2/8 \gg v_{ti}^2$ near $x \rightarrow \infty$, and at such large energies I expect the distribution function to be exponentially small. Thus, the contribution to the integral from this region of phase space is negligible and the limits of integration of equation (E.18) are appropriate.

The value of $\bar{x}_m(x)$ is given by equation (3.19) evaluated near $x \rightarrow \infty$,

$$\bar{x}_m(x) \simeq \frac{1}{2}x, \quad (\text{E.17})$$

The effective potential maximum at large \bar{x} is, from equation (4.51), $\chi_M(\bar{x}) \simeq \Omega^2 \bar{x}^2/2$. I can exchange the integrals over \bar{x} and U_{\perp} to get

$$n_{i,cl}(x) \simeq \int_0^{\infty} dU_{\perp} \int_{\bar{x}_b}^{\bar{x}_t} \frac{2\Omega d\bar{x}}{\sqrt{2(U_{\perp} - \chi(x, \bar{x}))}} \int_{U_{\perp}}^{\infty} \frac{F_{cl}(\mu(\bar{x}, U_{\perp}), U)}{\sqrt{2(U - U_{\perp})}} dU, \quad (\text{E.18})$$

where

$$\bar{x}_b = x - \frac{1}{\Omega} \sqrt{2 \left(U_{\perp} - \frac{\Omega \phi(x)}{B} \right)}, \quad (\text{E.19})$$

$$\bar{x}_t = x + \frac{1}{\Omega} \sqrt{2 \left(U_{\perp} - \frac{\Omega \phi(x)}{B} \right)}. \quad (\text{E.20})$$

The change in the integration limits is explained in Figure E1. Equations (E.14) and (E.15) can be used to make the change of variables $(x, \bar{x}, U_\perp, U) \rightarrow (x, \varphi, \mu, U)$ in equation (E.18). Using equations (E.14) and (E.15), the Jacobian

$$\left| \frac{\partial(\bar{x}, U_\perp)}{\partial(\varphi, \mu)} \right| = \left(1 + \frac{5\phi''(x)}{4B\Omega} \right) \sqrt{2\Omega\mu} |\sin \varphi| + O\left(\hat{\phi}\epsilon^3 v_{t,i}, \hat{\phi}^2 \epsilon^2 v_{t,i}\right) \quad (\text{E.21})$$

and the result

$$\frac{1}{\sqrt{2(U_\perp - \chi(x, \bar{x}))}} = \left(1 - \frac{\phi''(x)}{4B\Omega} \right) \frac{1}{\sqrt{2\Omega\mu} |\sin \varphi|} + O\left(\frac{\hat{\phi}\epsilon^3}{v_{t,i}}, \frac{\hat{\phi}^2 \epsilon^2}{v_{t,i}}\right), \quad (\text{E.22})$$

I obtain

$$\begin{aligned} n_{i,\text{cl}}(x) = & \left(1 + \frac{\phi''(x)}{\Omega B} \right) \int_{-\pi}^{\pi} d\varphi \int_0^\infty \Omega d\mu \int_{\Omega\mu}^\infty \frac{F_{\text{cl}}(\mu, U)}{\sqrt{2(U - \Omega\mu + \delta U_\perp)}} dU \\ & + O\left(\hat{\phi}\epsilon^3 n_\infty, \hat{\phi}^2 \epsilon^2 n_\infty\right), \end{aligned} \quad (\text{E.23})$$

where δU_\perp is defined in equation (4.18). Note that I changed the lower limit of the integral over U from U_\perp to $\Omega\mu$ in going from equation (E.18) to (E.23). The distribution function is zero for $U < \Omega\mu$. Therefore, the integrand is zero in the region $U_\perp < U < \Omega\mu$ and U_\perp can be replaced by $\Omega\mu$ in the integration limit of the integral in U .

E.4 Expansion of the integral over U in equation (E.23)

I begin by changing variables from U to $U_\star = U - \Omega\mu + \delta U_\perp$,

$$\int_{\Omega\mu}^\infty \frac{F_{\text{cl}}(\mu, U) dU}{\sqrt{2(U - \Omega\mu + \delta U_\perp)}} = \int_{\delta U_\perp}^\infty \frac{F_{\text{cl}}(\mu, U_\star + \Omega\mu - \delta U_\perp)}{\sqrt{2U_\star}} dU_\star. \quad (\text{E.24})$$

Note that $\delta U_\perp > 0$ for typical values of μ . I Taylor expand the distribution function

$$\begin{aligned} \int_{\delta U_\perp}^{\infty} \frac{F_{\text{cl}}(\mu, U_\star + \Omega\mu - \delta U_\perp)}{\sqrt{2U_\star}} dU_\star &= \int_{\delta U_\perp}^{\infty} \frac{F_{\text{cl}}(\mu, U_\star + \Omega\mu)}{\sqrt{2U_\star}} dU_\star \\ &- \int_{\delta U_\perp}^{\infty} \frac{\delta U_\perp}{\sqrt{2U_\star}} \frac{\partial F_{\text{cl}}}{\partial U}(\mu, U_\star + \Omega\mu) dU_\star + \frac{1}{2} \int_{\delta U_\perp}^{\infty} \frac{\delta U_\perp^2}{\sqrt{2U_\star}} \frac{\partial^2 F_{\text{cl}}}{\partial U^2}(\mu, U_\star + \Omega\mu) dU_\star + \dots \end{aligned} \quad (\text{E.25})$$

Each of the terms of equation (E.25) can then be split into two separate integrals over U_\star

$$\begin{aligned} n_i(x) &= \int_0^{\infty} \frac{dU_\star}{\sqrt{2U_\star}} \left(F_{\text{cl}}(\mu, U_\star + \Omega\mu) - \delta U_\perp \frac{\partial F_{\text{cl}}}{\partial U}(\mu, U_\star + \Omega\mu) \right. \\ &\quad \left. + \frac{1}{2} \delta U_\perp^2 \frac{\partial^2 F_{\text{cl}}}{\partial U^2}(\mu, U_\star + \Omega\mu) \right) - \int_0^{\delta U_\perp} \frac{dU_\star}{\sqrt{2U_\star}} \left(F_{\text{cl}}(\mu, U_\star + \Omega\mu) \right. \\ &\quad \left. - \delta U_\perp \frac{\partial F_{\text{cl}}}{\partial U}(\mu, U_\star + \Omega\mu) \right) + \dots \end{aligned} \quad (\text{E.26})$$

Then, for small δU_\perp , I Taylor expand the distribution function near $U_\star = 0$ in the integrals between 0 and δU_\perp (and I neglect terms of order $\delta U_\perp^{5/2}$)

$$\begin{aligned} n_i(x) &= \int_0^{\infty} \frac{dU_\star}{\sqrt{2U_\star}} \left(F_{\text{cl}}(\mu, U_\star + \Omega\mu) - \frac{\partial F_{\text{cl}}}{\partial U}(\mu, U_\star + \Omega\mu) \delta U_\perp \right. \\ &\quad \left. + \frac{1}{2} \frac{\partial^2 F_{\text{cl}}}{\partial U^2}(\mu, U_\star + \Omega\mu) \delta U_\perp^2 \right) - \int_0^{\delta U_\perp} \frac{dU_\star}{\sqrt{2U_\star}} \left(F_{\text{cl}}(\mu, \Omega\mu) \right. \\ &\quad \left. + (U_\star - \delta U_\perp) \frac{\partial F_{\text{cl}}}{\partial U}(\mu, \Omega\mu) \right) + \dots \end{aligned} \quad (\text{E.27})$$

Carrying out the integrals between 0 and δU_\perp , I obtain

$$\begin{aligned} n_i(x) &= \int_0^{\infty} \frac{dU_\star}{\sqrt{2U_\star}} \left(F_{\text{cl}}(\mu, U_\star + \Omega\mu) - \frac{\partial F_{\text{cl}}}{\partial U}(\mu, U_\star + \Omega\mu) \delta U_\perp \right. \\ &\quad \left. + \frac{1}{2} \frac{\partial^2 F_{\text{cl}}}{\partial U^2}(\mu, U_\star + \Omega\mu) \delta U_\perp^2 \right) - \sqrt{2\delta U_\perp} F_{\text{cl}}(\mu, \Omega\mu) \\ &\quad + \frac{1}{3} (2\delta U_\perp)^{3/2} \frac{\partial F_{\text{cl}}}{\partial U}(\mu, \Omega\mu) + \dots \end{aligned} \quad (\text{E.28})$$

Then, inserting (E.28) into equation (E.23) and changing the dummy integration variable to $U = U_\star + \Omega\mu$, one is left with the result of equation (4.17).

APPENDIX F

Proof that $k_2 > 0$ and $q_2 > 0$

In order to show that $k_2 > 0$, I argued in the main text (see discussion below equation (4.35)) that it is sufficient to show that

$$6\pi \int_0^\infty \Omega d\mu \int_{\Omega\mu}^\infty \frac{F_{\text{cold}}(\mu, U) v_{\text{B}}^4}{(2(U - \Omega\mu))^{5/2}} dU - \frac{n_{e\infty}}{Z} > 0. \quad (\text{F.1})$$

Remembering $v_z = \sqrt{2(U - \Omega\mu)}$ and equation (4.27), the integral in the first term can be recast as

$$2\pi \int_0^\infty \Omega d\mu \int_0^\infty \frac{F_{\text{cold}}(\mu, U) dU}{(2(U - \Omega\mu))^{5/2}} = \int_0^\infty \frac{f_{\infty z}(v_z)}{v_z^4} dv_z, \quad (\text{F.2})$$

where

$$f_{\infty z}(v_z) = \int_{-\infty}^\infty dv_x \int_{-\infty}^\infty f_\infty(\mathbf{v}) dv_y. \quad (\text{F.3})$$

By application of Schwarz's inequality I have the relation

$$\int_0^\infty \frac{f_{\infty z}(v_z)}{v_z^4} dv_z \int_0^\infty f_{\infty z}(v_z) dv_z \geq \left(\int_0^\infty \frac{f_{\infty z}(v_z)}{v_z^2} dv_z \right)^2. \quad (\text{F.4})$$

From quasineutrality and from the marginal form of the kinetic Chodura condition (5.7)

I obtain

$$Z \int_0^\infty f_{\infty z}(v_z) dv_z = n_{e\infty}, \quad (\text{F.5})$$

$$\int_0^\infty \frac{f_{\infty z}(v_z)}{v_z^2} dv_z = \frac{n_\infty}{v_B^2}. \quad (\text{F.6})$$

Substituting (F.6) and (F.5) in (F.4), I obtain

$$Z v_B^4 \int_0^\infty \frac{f_{\infty z}(v_z)}{v_z^4} dv_z \geq n_{e\infty}. \quad (\text{F.7})$$

Re-expressing the left hand side of the inequality in terms of $F(\mu, U)$ and U by using (F.2), I obtain

$$2\pi \int_0^\infty \Omega d\mu \int_{\Omega\mu}^\infty \frac{F_{cl}(\mu, U) v_B^4}{(2(U - \Omega\mu))^{5/2}} dU \geq \frac{n_{e\infty}}{Z}. \quad (\text{F.8})$$

From (F.8) I see that

$$6\pi \int_0^\infty \Omega d\mu \int_{\Omega\mu}^\infty \frac{F_{cl}(\mu, U) v_B^4}{(2(U - \Omega\mu))^{5/2}} dU - \frac{n_{e\infty}}{Z} \geq \frac{2n_{e\infty}}{Z} > 0, \quad (\text{F.9})$$

from which (F.1) immediately follows.

This proof can be straightforwardly adapted to show that $q_2 > 0$, where q_2 is defined in equation (4.67). Again, it suffices to show that the numerator of equation (4.67) is positive,

$$v_B^4 \int_{\bar{x}_c}^\infty \Omega d\bar{x} \int_{\chi_M(\bar{x})}^\infty \frac{F_{cl}(\mu(\bar{x}, \chi_M(\bar{x})), U)}{\sqrt{2(U - \chi_M(\bar{x}))}} \Delta \left[\frac{1}{v_{x0}^3} \right] dU - \frac{n_{e0}}{Z} > 0. \quad (\text{F.10})$$

The integral can be re-expressed as

$$\begin{aligned} & \int_{\bar{x}_c}^\infty \Omega d\bar{x} \int_{\chi_M(\bar{x})}^\infty \frac{F_{cl}(\mu(\bar{x}, \chi_M(\bar{x})), U)}{\sqrt{2(U - \chi_M(\bar{x}))}} \Delta \left[\frac{1}{v_{x0}^3} \right] dU \\ &= \int_{\bar{x}_c}^\infty \Omega d\bar{x} \int_{\chi_M(\bar{x})}^\infty \frac{F_{cl}(\mu(\bar{x}, \chi_M(\bar{x})), U)}{\sqrt{2(U - \chi_M(\bar{x}))}} dU \\ &\quad \times \int_{-\infty}^0 \frac{3}{v_x^4} \hat{\Pi}(v_x, -V_x(0, \bar{x}, \chi_M) - \Delta v_{x0}, -V_x(0, \bar{x}, \chi_M)) dv_x \\ &= 3 \int \frac{f_0(\mathbf{v})}{v_x^4} d^3v \\ &= 3 \int_{-\infty}^0 \frac{f_{0x}(v_x)}{v_x^4} dv_x, \end{aligned} \quad (\text{F.11})$$

where $f_{0x}(v_x)$ is defined in equation (??). The marginal form of Bohm's condition is

$$Z v_B^2 \int_{-\infty}^0 \frac{f_{0x}(v_x)}{v_x^2} dv_x = n_{e0} \quad (\text{F.12})$$

and quasineutrality is

$$Z \int_{-\infty}^0 f_{0x}(v_x) dv_x = n_{e0}. \quad (\text{F.13})$$

Proceeding in an analogous way to the previous derivation, I conclude that

$$v_B^4 \int_{\bar{x}_c}^{\infty} \Omega d\bar{x} \int_{\chi_M(\bar{x})}^{\infty} \frac{F_{cl}(\mu(\bar{x}, \chi_M(\bar{x}), U))}{\sqrt{2(U - \chi_M(\bar{x}))}} \Delta \left[\frac{1}{v_{x0}^3} \right] dU - \frac{n_{e0}}{Z} \geq \frac{2n_{e0}}{Z} > 0, \quad (\text{F.14})$$

from which (F.10) immediately follows.

APPENDIX G

Neglecting the contribution of type II closed orbits near $x = 0$

The expansion of the closed orbit density near $x = 0$ relies on distinguishing type I and type II effective potential curves. In section 4.4 I omitted the contribution of closed orbits associated with type II curves, denoted $n_{i,cl,II}(x)$. I proceed to show that this contribution is negligible.

From equation (4.44), and using the expansion (2.75) of V_x near the stationary maximum x_M , I obtain an expression for the contribution to the density near $x = 0$ due to ions in approximately closed type II orbits,

$$n_{i,cl,II}(x) \simeq 2 \int_{\bar{x}_m(x)}^{\bar{x}_{m,I}} \Omega \sqrt{|\chi_M''|} |x - x_M| d\bar{x} \int_{\chi_M(\bar{x})}^{\infty} \frac{F(\mu(\bar{x}, \chi_M), U)}{\sqrt{2(U - \chi_M(\bar{x}))}} dU. \quad (G.1)$$

The upper limit of integration in \bar{x} is $\bar{x}_{m,I}$, which is the value of \bar{x} above which the effective potential is a type I curve. It is easier to express the integral in (G.1) by changing variables from \bar{x} to x_M (for type II curves, x_M depends on the value of \bar{x}). The Jacobian of this change of variables can be obtained using the equation for a stationary maximum, which is $\chi'(x_M, \bar{x}) = 0$. Rearranging equation (2.38) evaluated at the stationary point

x_M , I deduce

$$\bar{x} = x_M + \frac{\phi'(x_M)}{\Omega B}. \quad (\text{G.2})$$

Differentiating this equation with respect to x_M , one obtains $|d\bar{x}/dx_M| = |\chi_M''|/\Omega^2$. Then, the integral (G.1) can be written in terms of x_M . The integration limit $\bar{x} = \bar{x}_{m,I}$ corresponds to $x_M = 0$, while the integration limit $\bar{x} = \bar{x}_m(x)$ corresponds to $x_M = x$.

For small x , one can Taylor expand the integrand near $\bar{x} = \bar{x}_{m,I}$ (which corresponds to $x_M = 0$) and retain only the leading order,

$$\begin{aligned} n_{i,\text{cl},\text{II}}(x) &\simeq 2 \int_0^x (x - x_M) \frac{|\chi''(0, \bar{x}_{m,I})|^{3/2}}{\Omega} dx_M \int_{\chi_M(\bar{x})}^{\infty} \frac{F_{\text{cl}}(\mu(\bar{x}_{m,I}, \chi_M(\bar{x}_{m,I})), U)}{\sqrt{2(U - \chi_M(\bar{x}_{m,I}))}} dU \\ &\simeq x^2 \frac{|\chi''(0, \bar{x}_{m,I})|^{3/2}}{\Omega} \int_{\chi_M}^{\infty} \frac{F_{\text{cl}}(\mu(\bar{x}_{m,I}, \chi_M(\bar{x}_{m,I})), U)}{\sqrt{2(U - \chi_M(\bar{x}_{m,I}))}} dU. \end{aligned} \quad (\text{G.3})$$

Hence, the contribution from type II closed orbits near $x = 0$ is proportional to x^2 and therefore subdominant compared to x , making it negligible. In fact, when $\bar{x}_{m,I} \rightarrow \infty$, I expect the contribution to be exponentially small because $\mu(\bar{x}_{m,I}, \chi_M(\bar{x}_{m,I})) \rightarrow \infty$ and F is usually exponentially small for $\mu \rightarrow \infty$.

APPENDIX H

Integrals of temperature-dependent distribution functions

The distribution functions in (4.80) are normalized according to equation (5.5). The integrals over v_y and v_z are trivially carried out to obtain the functions

$$f_{\infty z}(v_z) = \int f_{\infty}(\mathbf{v}) dv_x dv_y = \begin{cases} \mathcal{N} n_{\infty} \frac{4v_z^2}{\sqrt{\pi} v_{t,i}^5} \exp\left(-\frac{(v_z - uv_{t,i})^2}{v_{t,i}^2}\right) \Theta(v_z) & \text{for } \tau \leq 1, \\ \mathcal{N} n_{\infty} \frac{4v_z^2}{\sqrt{\pi} v_{t,i}^3 (v_{t,i}^2 + \tau v_z^2)} \exp\left(-\frac{v_z^2}{v_{t,i}^2}\right) \Theta(v_z) & \text{for } \tau > 1, \end{cases} \quad (\text{H.1})$$

All the integrals in this appendix are carried out using the dimensionless variables $\tilde{w}_z = v_z/v_{t,i} - u$ and $\tilde{v}_z = v_z/v_{t,i}$.

The normalization condition (5.5) is then

$$n_{\infty} = \int_0^{\infty} f_{\infty z}(v_z) dv_z \quad (\text{H.2})$$

Applying equation (H.2) for $\tau \leq 1$, and changing integration variable to \tilde{w}_z gives

$$n_{\infty} = \mathcal{N} n_{\infty} \frac{4}{\sqrt{\pi}} \int_{-u}^{\infty} (\tilde{w}_z + u)^2 \exp(-\tilde{w}_z^2) \quad (\text{H.3})$$

Thus,

$$\frac{4\mathcal{N}}{\pi^{1/2}} \int_{-u}^{\infty} (\tilde{w}_z^2 + 2\tilde{w}_z u + u^2) \exp(-\tilde{w}_z^2) = 1, \quad (\text{H.4})$$

The integral in equation (H.4) evaluates to

$$\int_{-u}^{\infty} (\tilde{w}_z^2 + 2\tilde{w}_z u + u^2) \exp(-\tilde{w}_z^2) = \frac{\sqrt{\pi}}{4} [(1 + 2u^2)(1 + \operatorname{erf}(u)) + 2u \exp(-u^2)]. \quad (\text{H.5})$$

Hence, equation (5.5) for $\tau \leq 1$ follows.

Applying equation (H.2) for $\tau > 1$ one finds, after changing variable to \tilde{v}_z ,

$$n_{\infty} = \frac{4\mathcal{N}n_{\infty}}{\pi^{1/2}} \int_0^{\infty} \frac{\tilde{v}_z^2 \exp(-\tilde{v}_z^2)}{1 + r\tilde{v}_z^2} d\tilde{v}_z. \quad (\text{H.6})$$

The last integral in equation (H.6) is obtained in the following way. First, one can obtain the integral of the function $\exp(-\tilde{v}_z^2)/(1 + r\tilde{v}_z^2)$ (which will be useful when imposing the kinetic Chodura condition (5.7) in the next paragraph). Re-expressing $1/(1 + r\tilde{v}_z^2)$ as a definite integral of the function $\exp(-\eta(1 + r\tilde{v}_z^2))$ with respect to a dummy variable η , one has

$$\begin{aligned} \int_0^{\infty} \frac{\exp(-\tilde{v}_z^2)}{1 + r\tilde{v}_z^2} d\tilde{v}_z &= \int_0^{\infty} \exp(-\eta) d\eta \int_0^{\infty} \exp(-(1 + \eta r)\tilde{v}_z^2) d\tilde{v}_z \\ &= \frac{\sqrt{\pi}}{2} \int_0^{\infty} \frac{\exp(-\eta)}{\sqrt{\eta r + 1}} d\eta. \end{aligned} \quad (\text{H.7})$$

Changing variable to $\xi = \sqrt{\eta + 1/r}$ gives

$$\begin{aligned} \int_0^{\infty} \frac{\exp(-\tilde{v}_z^2)}{1 + r\tilde{v}_z^2} d\tilde{v}_z &= \sqrt{\frac{\pi}{r}} \exp\left(\frac{1}{r}\right) \int_{1/\sqrt{r}}^{\infty} \exp(-\xi^2) d\xi \\ &= \frac{\pi}{2\sqrt{r}} \exp\left(\frac{1}{r}\right) \left[1 - \operatorname{erf}\left(\frac{1}{\sqrt{r}}\right)\right]. \end{aligned} \quad (\text{H.8})$$

Then, using the relation

$$\int_0^{\infty} \frac{\exp(-\tilde{v}_z^2)}{1 + r\tilde{v}_z^2} d\tilde{v}_z + r \int_0^{\infty} \frac{\tilde{v}_z^2 \exp(-\tilde{v}_z^2)}{1 + r\tilde{v}_z^2} d\tilde{v}_z = \int_0^{\infty} \exp(-\tilde{v}_z^2) d\tilde{v}_z = \frac{\sqrt{\pi}}{2}, \quad (\text{H.9})$$

the integral

$$\int_0^\infty \frac{\tilde{v}_z^2 \exp(-\tilde{v}_z^2)}{1 + r\tilde{v}_z^2} dx = \frac{\sqrt{\pi}}{2r} - \frac{\pi}{2r^{3/2}} \exp\left(\frac{1}{r}\right) \left[1 - \operatorname{erf}\left(\frac{1}{\sqrt{r}}\right)\right] \quad (\text{H.10})$$

is obtained. Inserting this integral into (H.6), one obtains \mathcal{N} .

Equation (F.6) is used to obtain the values of the positive constants u and r . For $\tau \leq 1$ one inserts the distribution function in (H.1) in (F.6) and changes variable to $\tilde{w}_z = v_z/v_{\text{ti}} - u$ to obtain

$$\frac{v_{\text{ti}}^2}{v_{\text{B}}^2} = \frac{4\mathcal{N}}{\pi^{1/2}} \int_{-u}^\infty \exp(-\tilde{w}_z^2) d\tilde{w} = 2\mathcal{N}(1 + \operatorname{erf}(u)). \quad (\text{H.11})$$

Rearranging equation (H.11) and inserting the value of \mathcal{N} , one obtains equation (5.9).

For $\tau > 1$, one changes variable to $\tilde{v}_z = v_z/v_{\text{ti}}$ in the integral (H.11) to obtain

$$\frac{v_{\text{ti}}^2}{v_{\text{B}}^2} = \frac{4\mathcal{N}}{\pi^{1/2}} \int_0^\infty \frac{\exp(-\tilde{v}_z^2)}{1 + r\tilde{v}_z^2} d\tilde{v}_z. \quad (\text{H.12})$$

Inserting the value of \mathcal{N} and the integral in equation (H.8), one obtains equation (5.8).

The ion fluid velocity is evaluated using the equation (H.13)

$$u_{z\infty} = \frac{1}{n_\infty} \int f_{\infty z}(v_z) v_z dv_z. \quad (\text{H.13})$$

For $\tau \leq 1$ one has

$$\begin{aligned} \frac{u_{z\infty}}{v_{\text{ti}}} &= \frac{4\mathcal{N}n_\infty}{\sqrt{\pi}} \int_0^\infty \frac{v_z^3}{v_{\text{ti}}^5} \exp\left(-\frac{(v_z - uv_{\text{ti}})^2}{v_{\text{ti}}^2}\right) dv_z \\ &= \frac{4\mathcal{N}n_\infty}{\sqrt{\pi}} \int_{-u}^\infty (\tilde{v}_z + u)^3 \exp(-\tilde{v}_z^2) d\tilde{v}_z. \end{aligned} \quad (\text{H.14})$$

The integrals in the final equality of (H.14) evaluate to

$$\begin{aligned} \int_{-u}^\infty (\tilde{v}_z + u)^3 \exp(-\tilde{v}_z^2) d\tilde{v}_z &= \int_{-u}^\infty (\tilde{v}_z^3 + 3\tilde{v}_z^2 u + 3\tilde{v}_z u^2 + u^3) \exp(-\tilde{v}_z^2) d\tilde{v}_z \\ &= \frac{1}{2} \exp(-u^2) (u^2 + 1) + \frac{\sqrt{\pi}u}{4} (3 + 2u^2) (1 + \operatorname{erf}(u)). \end{aligned} \quad (\text{H.15})$$

For $\tau > 1$ one has

$$\begin{aligned} \frac{u_{z\infty}}{v_{t,i}} &= \frac{4\mathcal{N}n_\infty}{\sqrt{\pi}v_{t,i}} \int_0^\infty \frac{v_z^3}{v_{t,i}^3(v_{t,i}^2 + rv_z^2)} \exp\left(-\frac{v_z^2}{v_{t,i}^2}\right) dv_z \\ &= \frac{4\mathcal{N}n_\infty}{\sqrt{\pi}} \int_0^\infty \frac{\tilde{v}_z^3}{(1 + r\tilde{v}_z^2)} \exp(-\tilde{v}_z^2) d\tilde{v}_z. \end{aligned} \quad (\text{H.16})$$

The integral in equation (H.16) is taken, as before, by expressing $1/(1+rx^2)$ as a definite integral,

$$\begin{aligned} \int_0^\infty \frac{\tilde{v}_z^3}{(1 + r\tilde{v}_z^2)} \exp(-\tilde{v}_z^2) d\tilde{v}_z &= \int_0^\infty \exp(-\eta) d\eta \int_0^\infty \tilde{v}_z^3 \exp(-\tilde{v}_z^2(1 + \eta r)) d\tilde{v}_z \\ &= \int_0^\infty \frac{\exp(-\eta)}{2(1 + \eta r)^2} d\eta \\ &= \frac{1}{2r} - \frac{1}{2r} \int_0^\infty \frac{\exp(-\eta)}{(1 + \eta r)} d\eta \\ &= \frac{1}{2r} - \frac{\exp(1/r)}{2r^2} \int_{1/r}^\infty \frac{\exp(-\eta')}{\eta'} d\eta' \end{aligned} \quad (\text{H.17})$$

where, in the last two steps, I have integrated by parts and then changed integration variable to $\eta' = \eta + 1/r$. Using the definition of the exponential integral in equation (5.12), one obtains

$$\int_0^\infty \frac{\tilde{v}_z^3}{(1 + r\tilde{v}_z^2)} \exp(-\tilde{v}_z^2) d\tilde{v}_z = \frac{1}{2r} - \frac{\exp(1/r)}{2r^2} E_1\left(\frac{1}{r}\right). \quad (\text{H.18})$$

Bibliography

- [1] V. Mukhovatov and V. Shafranov, “Plasma equilibrium in a tokamak”, *Nuclear Fusion* **11**, 605 (1971).
- [2] L. Spitzer Jr, “The stellarator concept”, *The Physics of Fluids* **1**, 253–264 (1958).
- [3] R. Post, “The magnetic mirror approach to fusion”, *Nuclear Fusion* **27**, 1579 (1987).
- [4] H. Bodin and A. Newton, “Reversed-field-pinch research”, *Nuclear fusion* **20**, 1255 (1980).
- [5] P. C. Stangeby, “The plasma boundary of magnetic fusion devices (IOP publishing, Bristol, UK)”, (2000).
- [6] A. Loarte, B. Lipschultz, A. S. Kukushkin, G. F. Matthews, P. C. Stangeby, N. Asakura, G. F. Counsell, G. Federici, A. Kallenbach, K. Krieger, et al., “Chapter 4: power and particle control”, *Nuclear Fusion* **47**, S203 (2007).
- [7] J. Laframboise, “Current collection by a positively charged spacecraft: effects of its magnetic presheath”, *Journal of Geophysical Research: Space Physics* **102**, 2417–2432 (1997).
- [8] M. Martinez-Sanchez and J. E. Pollard, “Spacecraft electric propulsion - an overview”, *Journal of Propulsion and Power* **14**, 688–699 (1998).

- [9] I. H. Hutchinson, “Principles of plasma diagnostics”, *Plasma Physics and Controlled Fusion* **44**, 2603 (2002).
- [10] A. Anders, S. Anders, and I. G. Brown, “Transport of vacuum arc plasmas through magnetic macroparticle filters”, *Plasma Sources Science and Technology* **4**, 1 (1995).
- [11] J. Cipolla and M. Silevitch, “On the temporal development of a plasma sheath”, *Journal of Plasma Physics* **25**, 373–389 (1981).
- [12] K. Riemann, “Kinetic analysis of the collisional plasma–sheath transition”, *Journal of Physics D: Applied Physics* **36**, 2811 (2003).
- [13] K. Riemann, J. Seebacher, D. Tskhakaya Sr, and S. Kuhn, “The plasma–sheath matching problem”, *Plasma physics and controlled fusion* **47**, 1949 (2005).
- [14] J. Loizu, P. Ricci, F. D. Halpern, and S. Jolliet, “Boundary conditions for plasma fluid models at the magnetic presheath entrance”, *Physics of Plasmas* (1994-present) **19**, 122307 (2012).
- [15] R. Chodura, “Plasma–wall transition in an oblique magnetic field”, *Physics of Fluids* (1958-1988) **25**, 1628–1633 (1982).
- [16] K.-U. Riemann, “Theory of the collisional presheath in an oblique magnetic field”, *Physics of Plasmas* (1994-present) **1**, 552–558 (1994).
- [17] I. H. Hutchinson, “Oblique ion collection in the drift approximation: how magnetized mach probes really work”, *Physics of Plasmas* (1994-present) **15**, 123503 (2008).
- [18] P. C. Stangeby, “The Bohm–Chodura plasma sheath criterion”, *Physics of Plasmas* (1994-present) **2**, 702–706 (1995).

- [19] M. Stanojević, J. Duhovnik, N. Jelić, A. Kendl, and S. Kuhn, “Fluid model of the magnetic presheath in a turbulent plasma”, *Plasma physics and controlled fusion* **47**, 685 (2005).
- [20] A. V. Chankin and P. C. Stangeby, “The effect of diamagnetic drift on the boundary conditions in tokamak scrape-off layers and the distribution of plasma fluxes near the target”, *Plasma physics and controlled fusion* **36**, 1485 (1994).
- [21] M. U. Siddiqui, D. S. Thompson, C. D. Jackson, J. F. Kim, N. Hershkowitz, and E. E. Scime, “Models, assumptions, and experimental tests of flows near boundaries in magnetized plasmas”, *Physics of Plasmas* (1994-present) **23**, 057101 (2016).
- [22] D. Tskhakaya and S. Kuhn, “The magnetised plasma-wall transition: theory and PIC simulation”, *Contributions to Plasma Physics* **44**, 564–570 (2004).
- [23] D. Tskhakaya and S. Kuhn, “Particle-in-cell simulations of the plasma-wall transition with a magnetic field almost parallel to the wall”, *Journal of nuclear materials* **313**, 1119–1122 (2003).
- [24] J. Kovačič, T. Gyergyek, and M. Čerček, “Pre-sheath formation in an oblique magnetic field: fluid model and PIC simulation”, *The European Physical Journal D* **54**, 383–389 (2009).
- [25] R. Khaziev and D. Curreli, “Ion energy-angle distribution functions at the plasma-material interface in oblique magnetic fields”, *Physics of Plasmas* (1994-present) **22**, 043503 (2015).
- [26] H. Gerhauser and H. Claassen, “Numerical study of the deformation of the ion distribution function in the magnetic presheath”, *Contributions to Plasma Physics* **38**, 331–336 (1998).

- [27] S. Devaux and G. Manfredi, “Vlasov simulations of plasma-wall interactions in a magnetized and weakly collisional plasma”, *Physics of Plasmas* (1994-present) **13**, 083504 (2006).
- [28] D. Coulette and G. Manfredi, “An Eulerian Vlasov code for plasma-wall interactions”, *Journal of Physics: Conference Series* **561**, 012005 (2014).
- [29] D. Coulette and G. Manfredi, “Kinetic simulations of the chodura and debye sheaths for magnetic fields with grazing incidence”, *Plasma Physics and Controlled Fusion* **58**, 025008 (2016).
- [30] E. R. Harrison and W. B. Thompson, “The low pressure plane symmetric discharge”, *Proceedings of the Physical Society* **74**, 145 (1959).
- [31] K.-U. Riemann, “The Bohm criterion and sheath formation”, *Journal of Physics D: Applied Physics* **24**, 493 (1991).
- [32] T. Daube and K.-U. Riemann, “Kinetic analysis of the plasma boundary layer in an oblique magnetic field”, *Physics of Plasmas* (1994-present) **6**, 2409–2417 (1999).
- [33] R. H. Cohen and D. D. Ryutov, “Particle trajectories in a sheath in a strongly tilted magnetic field”, *Physics of Plasmas* (1994-present) **5**, 808–817 (1998).
- [34] D. L. Holland, B. D. Fried, and G. J. Morales, “Sheath structure in a magnetized plasma”, *Physics of Fluids B: Plasma Physics* (1989-1993) **5**, 1723–1737 (1993).
- [35] U. Daybelge and B. Bein, “Electric sheath between a metal surface and a magnetized plasma”, *Physics of Fluids* (1958-1988) **24**, 1190–1194 (1981).
- [36] K. Sato, H. Katayama, and F. Miyawaki, “Effects of an oblique magnetic field on sheath formation in the presence of electron emission”, *Contributions to Plasma Physics* **34**, 133–138 (1994).

- [37] D. Tskhakaya Sr and L. Kos, “Comprehensive kinetic analysis of the plasma-wall transition layer in a strongly tilted magnetic field”, *Physics of Plasmas* **21**, 102115 (2014).
- [38] E. Shi, G. Hammett, T. Stoltzfus-Dueck, and A. Hakim, “Gyrokinetic continuum simulation of turbulence in a straight open-field-line plasma”, *Journal of Plasma Physics* **83** (2017).
- [39] F. I. Parra and P. J. Catto, “Limitations of gyrokinetics on transport time scales”, *Plasma Physics and Controlled Fusion* **50**, 065014 (2008).
- [40] R. Jorge, P. Ricci, and N. Loureiro, “A drift-kinetic analytical model for scrape-off layer plasma dynamics at arbitrary collisionality”, *Journal of Plasma Physics* **83** (2017).
- [41] R. Cohen and D. Ryutov, “Sheath physics and boundary conditions for edge plasmas”, *Contributions to Plasma Physics* **44**, 111–125 (2004).
- [42] D. Bohm, *The Characteristics of Electrical Discharges in Magnetic Fields*, 77 (1949).
- [43] E. Ahedo, “Structure of the plasma-wall interaction in an oblique magnetic field”, *Physics of Plasmas* **4**, 4419–4430 (1997).
- [44] E. Ahedo and D. Carralero, “Model of a source-driven plasma interacting with a wall in an oblique magnetic field”, *Physics of Plasmas (1994-present)* **16**, 043506 (2009).
- [45] H. Claaßen and H. Gerhauser, “Ion gyro-cooling in the magnetic presheath”, *Contributions to Plasma Physics* **36**, 381–385 (1996).
- [46] K.-U. Riemann, “Kinetic theory of the plasma sheath transition in a weakly ionized plasma”, *The Physics of Fluids* **24**, 2163–2172 (1981).

- [47] P. C. Stangeby, “The chodura sheath for angles of a few degrees between the magnetic field and the surface of divertor targets and limiters”, *Nuclear Fusion* **52**, 083012 (2012).
- [48] R. H. Cohen and D. D. Ryutov, “Spreading particle trajectories near a perfectly reflecting surface in a tilted magnetic field”, *Physics of Plasmas* **2**, 4118–4121 (1995).
- [49] A. Geraldini, F. I. Parra, and F. Militello, “Gyrokinetic treatment of a grazing angle magnetic presheath”, *Plasma Physics and Controlled Fusion* **59**, 025015 (2017).
- [50] A. Geraldini, F. Parra, and F. Militello, “Solution to a collisionless shallow-angle magnetic presheath with kinetic ions”, *Plasma Physics and Controlled Fusion* **60**, 125002 (2018).
- [51] D. D’Ippolito, J. Myra, S. Krasheninnikov, G. Yu, and A. Y. Pigarov, “Blob transport in the tokamak scrape-off-layer”, *Contributions to Plasma Physics* **44**, 205–216 (2004).
- [52] D. Carralero, P. Manz, L. Aho-Mantila, G. Birkenmeier, M. Brix, M. Groth, H. W. Müller, U. Stroth, N. Vianello, E. Wolfrum, et al., “Experimental validation of a filament transport model in turbulent magnetized plasmas”, *Physical review letters* **115**, 215002 (2015).
- [53] S. P. Hirshman, “Neoclassical current in a toroidally confined multispecies plasma”, *Physics of Fluids* **21**, 1295 (1978).
- [54] F. Militello and W. Fundamenski, “Multi-machine comparison of drift fluid dimensionless parameters”, *Plasma Physics and Controlled Fusion* **53**, 095002 (2011).

-
- [55] A. Kirk, N. B. Ayed, G. Counsell, B. Dudson, T. Eich, A. Herrmann, B. Koch, R. Martin, A. Meakins, S. Saarelma, et al., “Filament structures at the plasma edge on MAST”, *Plasma physics and controlled fusion* **48**, B433 (2006).
- [56] M. J. Gerver, S. E. Parker, and K. Theilhaber, “Analytic solutions and particle simulations of cross-field plasma sheaths”, *Physics of Fluids B* **2**, 1069–1082 (1990).
- [57] P. B. Parks and S. I. Lippmann, “Effect of magnetic field on the distribution of ions striking a planar target”, *Physics of Plasmas* **1**, 3883–3889 (1994).
- [58] J. R. Cary, D. Escande, and J. L. Tennyson, “Adiabatic-invariant change due to separatrix crossing”, *Physical Review A* **34**, 4256 (1986).
- [59] A. Neishtadt, “On the change in the adiabatic invariant on crossing a separatrix in systems with two degrees of freedom”, *Journal of Applied Mathematics and Mechanics* **51**, 586–592 (1987).
- [60] R. A. Pitts, A. Kukushkin, A. Loarte, A. Martin, M. Merola, C. E. Kessel, V. Komarov, and M. Shimada, “Status and physics basis of the ITER divertor”, *Physica Scripta* **2009**, 014001 (2009).
- [61] J. Loizu, J. Morales, F. Halpern, P. Ricci, and P. Paruta, “Scrape-off-layer current loops and floating potential in limited tokamak plasmas”, *Journal of Plasma Physics* **83** (2017).
- [62] J. H. Ingold, “Two-fluid theory of the positive column of a gas discharge”, *Physics of Fluids* (1958-1988) **15**, 75–85 (1972).
- [63] H. Claaßen and H. Gerhauser, “Generalized bohm’s criterion for thermal ions in oblique magnetic and electric fields”, *Contributions to Plasma Physics* **36**, 361–365 (1996).

- [64] A. Cavaliere, F. Engelmann, and G. Onori, “Comitato nazionale energia nucleare”, Roma, Report RT/FI (65) **58** (1965).
- [65] A. Masetto, F. D. Halpern, S. Jolliet, J. Loizu, and P. Ricci, “Finite ion temperature effects on scrape-off layer turbulence”, *Physics of Plasmas* **22**, 012308 (2015).
- [66] W. Eckstein, C. Garcia-Rosales, J. Roth, and J. László, “Threshold energy for sputtering and its dependence on angle of incidence”, *Nuclear Instruments and Methods in Physics Research Section B: Beam Interactions with Materials and Atoms* **83**, 95–109 (1993).
- [67] N. Mellet, B. Pégourié, C. Martin, J. Gunn, H. Bufferand, and P. Roubin, “Magnetic sheath effect on the gross and net erosion rates due to impurities”, *Physica Scripta* **2016**, 014064 (2016).
- [68] J. D. Huba, *NRL plasma formulary*, tech. rep. NRL/PU/6790–16-614 (Naval Research Laboratory, Washington DC, 2016).
- [69] E. Havlíčková, W. Fundamenski, F. Subba, D. Coster, M. Wischmeier, G. Fishpool, et al., “Benchmarking of a 1D scrape-off layer code SOLF1D with SOLPS and its use in modelling long-legged divertors”, *Plasma Physics and Controlled Fusion* **55**, 065004 (2013).